OPTICAL CONTROL OF ELECTRON SPINS IN DIAMOND

by

DAVID ANDREW GOLTER II

A DISSERTATION

Presented to the Department of Physics
and the Graduate School of the University of Oregon
in partial fulfillment of the requirements
for the degree of
Doctor of Philosophy

December 2014

DISSERTATION APPROVAL PAGE

Student: David Andrew Golter II

Title: Optical Control of Electron Spins in Diamond

This dissertation has been accepted and approved in partial fulfillment of the requirements for the Doctor of Philosophy degree in the Department of Physics by:

Dr. Michael Raymer	Chairperson
Dr. Hailin Wang	Advisor
Dr. Raymond Frey	Core Member
Dr. Steven van Enk	Core Member
Dr. George Nazin	Institutional Representative

and

J. Andrew Berglund	Dean of the Graduate School

Original approval signatures are on file with the University of Oregon Graduate School.

Degree awarded December 2014

DISSERTATION ABSTRACT

David Andrew Golter II

Doctor of Philosophy

Department of Physics

December 2014

Title: Optical Control of Electron Spins in Diamond

By choosing the right system and using the right techniques, it is possible to achieve reliable control of an individual quantum system in a solid. Certain atom-like solid-state systems are especially suited for this goal. The electron spin of the diamond nitrogen-vacancy (NV) impurity center is a leader among such systems and has featured in a great deal of recent experimental work in the context of various quantum technologies. By extending optical control for the NV center we increase the utility of this system, opening it up to fresh applications in quantum optics.

Doing quantum control with a solid-state spin comes with its own challenges. In particular it can be difficult to simultaneously isolate single systems, both for control and from environment-induced decoherence, while also coupling multiple systems together in a controlled way. A goal of the work presented in this dissertation is to develop techniques for answering this problem in the NV center.

Optical control, as opposed to the microwave control usually used for state manipulation in the NV center, would make it easier to address only one spin system at a time. We demonstrate such control using two methods, two-photon optically driven Rabi oscillations and stimulated Raman adiabatic passage. These both have the added advantage that by using Raman-resonant, dipole-detuned optical fields, they protect the spin state from the decoherence normally associated with the optical transitions. Furthermore, we see that this electron spin control is nuclear spin dependent, providing a mechanism for coupling these two spin systems.

We also investigate a decoherence reduction technique that involves coupling continuous microwave fields to the spin states. The resulting “dressed states” are shielded from spin-bath-induced magnetic field fluctuations. We confirm this using optical coherent population trapping measurements which we have also developed in the NV center. We show that these measurements are sensitive to nuclear spin states as well as to dressed states.

These results supply the missing piece, optical spin manipulation, to control schemes that are all-optical, and they demonstrate ways to significantly push back the decoherence limit.

This dissertation includes previously published and unpublished co-authored material.

CURRICULUM VITAE

NAME OF AUTHOR: David Andrew Golter II

GRADUATE AND UNDERGRADUATE SCHOOLS ATTENDED:

University of Oregon, Eugene OR
Wheaton College, Wheaton IL

DEGREES AWARDED:

Doctor of Philosophy, Physics, 2014, University of Oregon
Bachelor of Science, Physics, Philosophy, 2007, Wheaton College

PROFESSIONAL EXPERIENCE:

Graduate Teaching Fellow, Department of Physics, University of Oregon, Eugene, 2007-2014

PUBLICATIONS:

D. A. Golter, T. K. Baldwin, and H. Wang, "Protecting a solid-state spin from decoherence using dressed spin states," *Phys. Rev. Lett.*, vol. 113, pp. 237601-237605, 2014.

D. A. Golter, and H. Wang, "Optically driven Rabi oscillations and adiabatic passage of single electron spins in diamond," *Phys. Rev. Lett.*, vol. 112, pp. 116403-116407, 2014.

D. A. Golter, K. N. Dinyari, and H. Wang, "Nuclear-spin-dependent coherent population trapping of single nitrogen-vacancy centers in diamond," *Phys. Rev. A*, vol. 87, pp. 035801-035805, 2013.

K. N. Dinyari, R. J. Barbour, D. A. Golter, and H. Wang., "Mechanical tuning of whispering gallery modes over a 0.5 THz tuning range with MHz resolution in a silica microsphere at cryogenic temperatures," *Optics Express*, vol. 19, pp. 17966-17972, 2011.

ACKNOWLEDGMENTS

I would like to thank my advisor, Hailin Wang, for his support, encouragement, guidance, and patience. He worked very hard to give me all the resources that I needed in order to play around with some cool Physics. He taught me how to do research, a lesson which requires a major commitment of energy and time on the part of the teacher.

I am grateful to the faculty members on my committee, Michael Raymer, Raymond Frey, Steven van Enk, and George Nazin for their help and input.

I thank Nima Dinyari for teaching me how to work in a lab, as well as all the other graduate and postdoctoral researchers whom I have worked alongside of at some point in my time here (in roughly their order of appearance): Carey Phelps, Tim Sweeney, Tom Baldwin, Thein Oo, Mark Kuzyk, Victor Fiore, Russell Barbour, Yong Yang, Chunhua Dong, Jintao Zhang, Maira Amezcua, Ignas Lekavicius, Kentaro Hoeger, and Xuefeng Jiang. They have contributed to building a productive lab, and I have enjoyed collaborating, troubleshooting, and commiserating with them all.

Finally, I thank all the university staff who make research possible in the first place.

To My Mom, Dad, and Sister

TABLE OF CONTENTS

Chapter Page

I. INTRODUCTION 1

1.1. Optical Control of a Quantum System 1

1.2. Physical Systems for Quantum Control 2

1.3. Overcoming the Disadvantages of Solid-State Systems 3

1.4. Dissertation Outline 5

1.5. Acronyms Used in this Disseration 7

II. THE DIAMOND NV CENTER 8

2.1. NV Center Structure 8

2.2. NV Center Applications 13

III. EXPERIMENTAL METHODS 16

3.1. Experimental Setup 16

3.2. Preliminary Low-Temperature Investigations 19

3.2.1. Confocal Imaging of Single NV Centers 20

3.2.2. Photoluminescence Excitation 21

3.2.3. Optically Detected Magnetic Resonance 23

3.2.4. Rabi Oscillations 26

3.2.5. Conclusion 30

IV. COHERENT POPULATION TRAPPING IN THE NV CENTER 31

4.1. Coherent Population Trapping: Theory 32

4.2. Λ-Type Configuration in the NV Center 33

4.3. Coherent Population Trapping: Experiment 36

4.4. Nuclear Spin Dependent Coherent Population Trapping 37

4.5. Dynamic Stark Splitting Measured by Coherent Population Trapping 39

  4.5.1. Dynamic Stark Splitting Introduction 40

  4.5.2. Measurement of Dynamic Stark Splitting 41

4.6. Conclusion 43

V. ALL-OPTICAL CONTROL OF THE NV CENTER 45

5.1. MW Control versus Optical Control 46

5.2. Optically Driven Rabi Oscillations with a Two-Photon Transition 47

  5.2.1. Two-Photon ODROs: Theory 48

  5.2.2. Two-Photon ODROs: Experiments 49

  5.2.3. Nuclear Spin Dependence of the Two-Photon ODROs 51

  5.2.4. Ramsey Fringes Measured using Two-Photon ODROs 53

5.3. Stimulated Raman Adiabatic Passage 56

  5.3.1. Stimulated Raman Adiabatic Passage: Theory 56

  5.3.2. Stimulated Raman Adiabatic Passage: Experiments 57

5.4. Theoretical Model 59

  5.4.1. Model of Two-Photon ODROs 60

  5.4.2. Model of the STIRAP Experiment 62

5.5. Subwavelength Resolution using Optical Control 64

  5.5.1. Subwavelength Resolution Techniques 65

5.5.2. Subwavelength Resolution Experiment 66

5.6. Conclusion 69

VI. DECOHERENCE PROTECTED DRESSED SPIN STATES IN THE NV CENTER 71

6.1. Strategies for Improving the Coherence Time of the NV Electronic Spin State 72

6.2. Dressed Spin States 74

6.2.1. MW Dressed Spin States in the NV Center 74

6.2.2. Insensitivity of the Dressed States to Magnetic Fluctuations 75

6.2.3. CPT Measurement of the Dressed Spin States 77

6.3. Coherent Population Trapping Analysis 81

6.3.1. Coherent Population Trapping of Bare Spin States 82

6.3.2. Coherent Population Trapping of Dressed Spin States 85

6.3.3. Amplitudes of the Dressed State CPT Resonances 87

6.4. CPT Linewidths for Bare and Dressed Spin States: Experimental Results 88

6.5. Conclusion 93

VII. CONCLUSION 94

7.1. Summary 94

7.2. Future Work 96

REFERENCES CITED 98

LIST OF FIGURES

Figure Page

2.1. Diagram of NV center ground and excited electron spin configurations in the four occupied orbitals.......... 9

2.2. NV center electronic ground spin state structure including zero-field splitting (2.88 GHz), Zeeman splitting (ω_B), hyperfine splittings (2.2 MHz), and quadrapole splitting (5 MHz).......... 10

2.3. Energy level structure of the NV center, demonstrating spin-dependent fluorescence and spin-state polarization under off-resonant optical excitation. Ground and excited state levels are grouped by their spin value.......... 12

3.1. Diagram of the experimental setup.......... 17

3.2. (a) SEM image of the SIL. (b) Profile of the SIL shape.......... 18

3.3. 2D fluorescence image. Fluorescence was collected under 532 nm illumination. The bright spots are NV centers. The arrow indicates the NV center that was used.......... 20

3.4. (a) PLE spectrum of a single NV center. The frequency of a 632 nm laser is scanned while the sideband fluorescence is collected. Each peak is labeled by the transition it represents. (inset) Pulse sequence used for PLE measurements. (b) PLE scan of the $m_s = 0 \rightarrow E_y$ transition indicating a broadened linewidth, due to spectral diffusion, of around 600 MHz.......... 21

3.5. Decay of the fluorescence signal under continued (a) high power and (b) low power resonant excitation due to optical pumping and photoionization. This limits the detection time for an efficient PLE spin measurement.......... 22

3.6. ODMR measurement. (a) Pulse sequence. (b) Fluorescence as a function of MW frequency. The single dip corresponds to the $m_s=0 \rightarrow m_s=\pm1$ ground state transition at 2.877 GHz (at low temperature).......... 24

3.7. ODMR measurement with an external B-field. The left dip corresponds to the $m_s=0 \rightarrow m_s=-1$ transition, and the right dip corresponds to the $m_s=0 \rightarrow m_s=+1$ transition. This indicates a Zeeman splitting between $m_s=-1$ and $m_s=+1$ of 155 MHz.......... 25

3.8. ODMR measurement of the m_s=0 → m_s=-1 transition with (a) high MW power (π-pulse = 120 ns) and (b) low MW power (π-pulse = 790 ns). The three dips in (b) correspond to the three hyperfine states, due to coupling with the ^{14}N nuclear spin, and exhibit a splitting of 2.2 MHz 26

3.9. Rabi oscillations. The fluorescence from a PLE measurement following a MW pulse is plotted as a function of the MW pulse length. PLE is measured from the m_s=0 → E_y,(a) and m_s=+1 → A_2 (b) transitions as indicated in the energy level diagram in (c). (d) Rabi frequency as a function of the square root of the MW power. The expected linear relation is observed. 27

3.10. Rabi oscillations. The beating is due to coupling between the NV center electron spin and the ^{14}N nuclear spin. The detuning of the MW field is different for each hyperfine state leading to different Rabi frequencies. The measurement sums over the contributions from all three hyperfine states and exhibits a beating. 29

3.11. Nuclear spin dependent Rabi oscillations. A low MW power only drives one hyperfine state at a time. 30

4.1. Three-level Λ-configuration. The two transitions are driven by two fields with Rabi frequencies of Ω_a and Ω_b and with an overall dipole detuning of Δ and a Raman detuning of δ.. 33

4.2. (a) Λ-configuration in the NV center. The A_2 excited state couples to the m_s=-1 and m_s=+1 ground states via σ+ and σ- polarized optical fields respectively. (b)PLE spectra of the two A_2 transitions indicating a Zeeman splitting of about 500 MHz. Each transition was selected by using a CW MW field tuned to the appropriate ground state transition. 34

4.3. (a) Energy-level diagram. Both optical fields have the same power (combined power = 1 μW). One is tuned in frequency while the other is held fixed. (b) CPT measurement. Away from Raman resonance A_2 is excited and the fluorescence is high. On Raman resonance the system is pumped into the dark state and fluorescence is low 36

4.4. Nuclear spin dependent CPT. (a) Energy-level diagram indicating the three hyperfine Raman resonance conditions. (b) Pulse sequence. (c) CPT measurement using low optical power (combined power = 60 nW) and a strong MW π-pulse. All three hyperfine states are visible. (d) Three different CPT traces obtained using low optical power and a weak MW π-pulse populating the m_n = -1 (blue, dashed line), m_n = 0 (black, solid line), or m_n = +1 (red, dotted line) hyperfine state... 38

4.5. Dynamic Stark splitting of a two-level system coupled resonantly to a field with Rabi frequency Ω_d. 40

4.6. CPT measurement of dynamic Stark splitting for different MW powers (vertically offset). A CW MW field is applied to the ground state transition for the $m_n = 0$ hyperfine state during the CPT measurement. The center CPT dip is split by an amount dependent on the strength of this field. 42

4.7. CPT measurement of dynamic Stark splitting for different MW detunings (vertically offset). For the top trace, the MW frequency is 9.9 MHz above the ground state transition for the $m_n = 0$ hyperfine state. For each succeeding trace, the frequency is shifted down by 2 MHz. 43

5.1. (a) Energy level diagram including the hyperfine splitting, optical and MW excitations, and the relevant excited states. (b) Pulse sequence used for two-photon ODROs.. 49

5.2. (a) ODROs of an electron spin. The fluorescence measures the population in the $m_s = \pm 1$ states. (b) Period of the ODROs as a function of detuning for three different optical intensities. Inset: effective Rabi frequency as a function of the intensity for three different detunings.. 50

5.3. Nuclear spin selective ODROs with detunings indicated in the CPT trace shown in (a). (b)-(d) The populations in the $m_s = -1$ (top traces) and $m_s = +1$ (bottom traces) states as a function of optical pulse width 52

5.4. Ramsey fringe measurement using ODROs. (a) Pulse sequence for the spin manipulation step. (b)-(e) Free induction decays of an electron spin with $\Omega_R/2\pi = 2.5$ MHz and $\Delta = -1$ GHz. For (b), (c), and (d), nuclear-spin-selective MW π-pulses were used to prepare the electron spin in the $m_s = -1$ and $m_n = 0, -1$, and $+1$ hyperfine states respectively so that only these hyperfine states contribute to the signal. For (e), the electron spin was prepared in the $m_s = -1$ state with random nuclear spin orientation. 55

5.5. STIRAP and ODROs. (a) The temporal line shapes of the two Raman resonant optical pulses used during the spin manipulation step. The final population in state $m_s = +1$ is measured as a function of delay, T, between the two pulses. The regimes where STIRAP and ODROs take place are indicated. (b)-(e) Left column: experimental results obtained with different t_{rise}, as shown in the figure. Right column: theoretical calculations using the parameters of the experiments in the left column... 58

5.6. Simulation of the two-photon ODROs. (a) Δ held constant and $\delta = 0$. (b) Spectral diffusion is included. Sum over Δ's with $\delta = 0$. (c) Dephasing is included. Sum over δ's with Δ held constant. (d) Both spectral diffusion and dephasing are included. Sum over Δ's and δ's. 61

5.7. Simulation of the STIRAP/ODRO measurement. (a) Δ held constant and $\delta = 0$. (b) Spectral diffusion is included. Sum over Δ's with $\delta = 0$. (c) Dephasing is included. Sum over δ's with Δ held constant. (d) Both spectral diffusion and dephasing are included. Sum over Δ's and δ's. 63

5.8. PLE measurement of the two beam profiles used for the subwavelength spatial resolution experiment. Only one dimension is shown. (a) Desired pulse shapes. (b) Fluorescence as the Gaussian beam is scanned over the NV center. (c) Fluorescence as the doughnut beam is scanned over the NV center. The doughnut beam is given an overall higher power in the experiment. 67

5.9. Spatially dependent STIRAP. (a) Spatial profile of the two optical fields. The shaded regions indicate where the greatest spin transfer occurs. (b) Final population in $m_s = -1$ indicating a spin transfer. (c) Final population in $m_s = +1$. 68

6.1. Two resonant MW fields with equal Rabi frequency, Ω_m, leads to the formation of three dressed states... 76

6.2. (a) The energies of the dressed spin states with the effects of a bath-induced Zeeman shift, $\pm\delta_N$, included. (b) The energies of the dressed spin states as a function of δ_N. For $\Omega_m >> |\delta_N|$, the curves are relatively flat, indicating an insensitivity to changes in δ_N. 77

6.3. Energy level diagram with both the dressed state and bare spin state nature of the ground state levels made explicit. Each of these ground state levels corresponds to a term in (6.5). The two optical fields continue to couple to the transitions between the bare spin states and the $|A_2>$ excited state. 78

6.4. Coherent population trapping of dressed spin states. Fluorescence is collected while one optical field is held fixed and the other is tuned. Dips indicate frequencies where the Raman detuning between the two fields is equal to the splitting between dressed state levels associated with different bare spin states. The resonances are labeled with energy level diagrams indicating which coherences are involved in that feature... 80

Figure Page

6.5. The frequency splitting between the central resonance and the first sidebands, as a function of MW Rabi frequency, in CPT measurements similar to that shown in Fig. 6.4 81

6.6. The optical power dependent linewidth of the CPT resonance. 1nW corresponds to an estimated $\Omega_O/2\pi = 0.74$ MHz. Circles (blue) are for the bare spin states. Squares (black) are for the center resonance in the CPT measurement of the dressed spin states. 89

6.7. (a) The linewidth of the central CPT resonance for the dressed spin states as a function of the incident optical power. The data is consistent with the theoretically expected deviations from linear power broadening. (b) The central CPT resonance obtained at the lowest optical power used (0.85 nW). 90

6.8. The linewidth of the first CPT sideband (red, circles) and the central CPT resonance (black, squares) as a function of Ω_m with an incident optical power of 2.5 nW. At higher MW power the resonances exhibit similar power broadening. At lower MW power the dressed state decoherence protection breaks down for the sideband, but not for the center resonance. 92

CHAPTER I

INTRODUCTION

1.1. Optical Control of a Quantum System

Contemporary advances in technology and in our understanding of certain physical systems have raised the exciting prospect of establishing reliable control of individual quantum-mechanical systems [1]. Experimental efforts along these lines work to advance basic quantum phenomena, for example Rabi oscillations or entanglement, from idealized theoretical textbook examples to practical experimental demonstrations involving real physical systems. Moreover, while many initial demonstrations of such quantum control involved ensembles [2], manipulation of single systems is becoming increasingly viable. Achievements in quantum control, while interesting challenges in their own right, also contribute to the development of new technologies, technologies that are useful for applications such as quantum information processing [3],[4] and metrology [5],[6].

Before these applications can be realized, it is necessary to generate consistent quantum state initialization, manipulation, and readout procedures. Coherent control methods involving optical fields have been particularly successful for meeting these requirements in isolated atoms [7]. The interaction between atoms and photons is well-understood. Optical control also lends itself to extensions into cavity QED scenarios [8]. Atom-like solid-state systems, which are generating increasing interest as quantum systems for coherent control applications, would benefit from the incorporation of optical control techniques.

In this dissertation we present several demonstrations of such optical control in a solid-state electron spin system. Using the negatively-charged nitrogen-vacancy impurity center (NV center) in diamond, we accomplish coherent population trapping (CPT), optically driven Rabi oscillations (ODROs), and stimulated Raman adiabatic passage (STIRAP). Furthermore we use optical methods to monitor the coherence properties of this system and confirm the effectiveness of using dressed states to minimize decoherence.

1.2. Physical Systems for Quantum Control

When it comes to choosing a physical system in which to implement quantum control one finds a large array of potential candidates [4], [9], everything from photons to superconducting circuits. Of particular interest are quantum states associated with isolated atoms [10], [7]. The structure and dynamics of such systems are well understood, and control techniques have been widely developed. For example, internal states such as electron spin can be used as qubits, while radiation fields work to initialize, manipulate, and readout these states [11], [12]. Additionally such systems are typically well isolated from their environment, reducing the impact of that fundamental enemy of quantum control, decoherence.

Atomic systems, however, are subject to several important limitations. The need to constrain the position and motion of individual atoms requires extensive external infrastructure, e.g. ion traps [13], optical lattices [14]. In such an arrangement it can be difficult to interact multiple quantum systems with each other, a requirement, for instance, in quantum information applications. Incorporating the atomic system into other structures such as optical cavities or mechanical resonators is also a challenge.

Atom-like solid-state systems, such as quantum dots [15] or impurity centers [16], possess many of the advantages of atomic systems while overcoming some of their limitations. The position and motion of these solid-state systems are naturally constrained. Multiple systems can potentially be packed closely enough to even allow direct dipole-dipole interactions. Well-developed fabrication techniques make it possible to build more intricate quantum devices that incorporate cavities or resonators [17]. For these reasons and more, such atom-like systems have become the focus of a great deal of research [18], [19].

The NV center in diamond has emerged as a leading solid-state point defect system. With electronic spin states that exhibit long (for a solid-state system) coherence times, and an energy level structure that lends itself to microwave (MW) control and optical initialization and readout even at room temperature, the NV center has been an ideal system for pursuing quantum control applications [20]-[22]. Researchers have made significant progress in both understanding the electronic structure and spin dynamics of this physical system on one side and in demonstrating basic quantum control techniques on the other.

1.3. Overcoming the Disadvantages of Solid-State Systems

For all their advantages, atom-like solid-state systems like the NV center present their own challenges. While closely spaced quantum systems make interactions easier, they also make spatial resolution more difficult. While having a quantum system embedded in a larger material structure makes confinement of the system easier, it also increases unwanted interactions between the system and its environment leading to effects such as spectral diffusion and decoherence. The particular quantum control methods which we demonstrate in this dissertation help to mitigate these problems in the NV center making it an even more attractive quantum system for control applications. Moreover, the techniques presented here could also, in the future, be applied to other solid-state systems such as SiC [23], [24].

Specifically we demonstrate coherent, all-optical control methods which, when combined with well-established optical state initialization and readout, allow frequency resolution where spatial resolution is difficult [25], sidestep spectral diffusion effects, and avoid radiative decay. We also show that MW dressed states can be used to greatly reduce decoherence, which is perhaps the biggest challenge for a solid-state system.

A common feature of these experiments is the use of a coupling radiation field (or fields) to change the underlying spin dynamics of the atom-like system, altering its response to, say, an additional radiation field, or to its environment. For instance, in the phenomenon known as electromagnetically induced transparency, the presence of a “control” field renders the atomic system transparent to a second “probe” field [26]. Our concern is with the effect on the atomic system itself rather than with the nonlinear optical effects on the fields. This side of the picture is referred to as coherent population trapping [27]. Quantum interference cancels out the two field-driven transitions, creating within the atomic system, a “dark” state, that is, a coherent superposition of atomic energy states that is shielded from excitation. This mechanism lies at the heart of the all-optical control techniques which we demonstrate.

Similarly, we explore a method of minimizing decoherence that relies on the change in the spin dynamics of an atomic system resulting from a coherent preparation with continuous radiation fields. These “dressed” states are just composite atom-field states [27],[28], and behave in a way that is fundamentally different from the non-dressed spin states.

Choosing a physical system in which to implement quantum control is inevitably going to involve tradeoffs. By developing the right control techniques, however, we can play to the strengths of this solid-state system while minimizing its weaknesses. The results contribute to the general goal of providing reliable control over an individual quantum system.

1.4. Dissertation Outline

In Chapter II we give an introduction to the diamond NV center. We provide a brief outline of the current theoretical understanding of this system’s energy level structure. This is followed by a survey of previous experimental research, with an emphasis on quantum control applications. We put our own work in the context of this continuing effort to demonstrate coherent quantum control in a solid-state atom-like system.

Chapter III begins with a description of our experimental setup as well as some details of our general experimental methods. We then review the results of preliminary investigations into the NV center at low temperature including MW control, optically detected magnetic resonance (ODMR), and photoluminescence excitation (PLE).

Chapters IV, V, and VI present our main experimental results. In Chapter IV CPT measurements are discussed. CPT provides a highly sensitive means of probing the energy-level structure of this system. We see that the CPT can be nuclear-spin-dependent, revealing the hyperfine structure of the electron-spin ground states. Additionally, the CPT trace is sensitive to the dynamic Stark splitting induced by a coherent spin excitation. This indicates that CPT can be used to measure dressed states, a feature that we will employ in Chapter VI. This chapter contains some previously published material that was co-authored with Khodadad N. Dinyari and Hailin Wang.

All-optical control of the NV center is the subject of Chapter V. A standard control method for the NV center involves using a single MW field resonantly coupled to a single electronic spin transition, where the two spin states associated with that transition represent the qubit states. In contrast, the techniques we use involve two optical fields and three spin states, with a subset of the spin states acting as the qubit. We demonstrate two control methods, both involving the optical Raman resonances which underlay the CPT described in Chapter IV. Method one consists of optically driven Rabi oscillations of a two-photon transition. Method two involves stimulated Raman adiabatic passage via the controlled evolution of a dark state. We compare these two processes both theoretically and experimentally and analyze the effects of spin dephasing and spectral diffusion. This chapter contains some previously published material that was co-authored with Hailin Wang.

In Chapter VI we demonstrate the use of dressed states for protection from decoherence. In the case of the NV center, magnetic field fluctuations due to a surrounding spin bath are the primary source of decoherence. We present a technique for significantly improving coherence time by using MW dressed spin states that are protected from these fluctuations. CPT measurements of these dressed states show an improvement in coherence time by at least a factor of 50, limited by the transit time broadening of the measurement. This chapter contains some previously published material that was co-authored with Hailin Wang and Thomas K. Baldwin.

Chapter VII offers a summary of the main results of our work, and briefly suggests some further applications of the techniques we have presented.

1.5. Acronyms Used in this Dissertation

CPT – Coherent Population Trapping

CW – Continuous Wave

MW – Microwave

NV (center) – Nitrogen-Vacancy

ODMR – Optically Detected Magnetic Resonance

ODRO – Optically Driven Rabi Oscillation

PLE – Photoluminescence Excitation

STIRAP – Stimulated Raman Adiabatic Passage

CHAPTER II

THE DIAMOND NV CENTER

Our understanding of the diamond NV center matured greatly over the last two decades, to the point that we now have a fairly comprehensive theoretical picture of its structure and dynamics. This has been accompanied, as well as aided, by an explosion in impressive experimental advances. Over the last decade, this impurity center has proven itself to be an excellent model system for demonstrating fundamental quantum mechanical applications and the basic building blocks of quantum control and quantum information processing. In the first part of this short chapter we outline the characteristics of the NV center, what it is and how it works. In the second, we summarize the major experimental developments that have made this solid-state system so exciting.

2.1. NV Center Structure

Diamond is attractive as a host for impurity centers for a number of reasons [17], [22], [29]. It is chemically inert. It has a high Debye temperature, meaning low electron-phonon coupling which increases spin-lattice relaxation times [30]. It consists primarily of the zero nuclear spin ^{12}C isotope resulting in a less noisy magnetic environment. Importantly, diamond has a relatively large energy bandgap (5.5 eV) with enough room to fit both ground and excited impurity electronic states. This makes these impurities optically active, even in the visible or infrared regimes. There exist hundreds of such "color" centers in diamond, many of which have not yet been extensively studied [31].

One which has received considerable attention is the nitrogen-vacancy center. Consisting of a substitutional nitrogen impurity adjacent to an empty lattice site, these impurity centers are naturally occurring and are quite common. Alternatively, they can be created through a combination of implantation and annealing. We are primarily interested in the electron-spin-state structure for the NV center. This structure and its properties have been well explained using molecular models [32]-[34] and group theory considerations along with *ab initio* calculations [35], [36]. Without going into the details of these models, we summarize the main relevant features of this system [37].

There are six electrons associated with the NV center. The nitrogen atom supplies two free electrons, while the dangling bonds for the three carbon atoms neighboring the vacancy each contribute one. In the case of the negatively charged NV center an additional electron has been captured from elsewhere in the material. (Throughout this dissertation “NV center” will refer to the negatively charged variety unless stated otherwise.) The NV center’s spin states refer to the net spin of these six electrons (see Fig. 2.1).

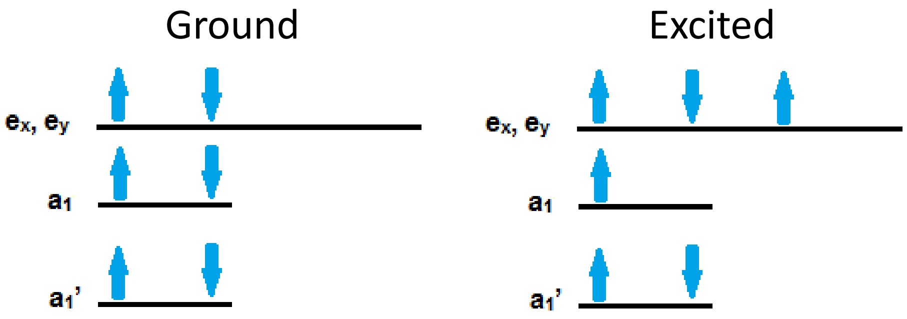

Figure 2.1. Diagram of NV center ground and excited electron spin configurations in the four occupied orbitals (e_x*,* e_y*,* a_1*,* a_1*’).*

The ground electron spin state for this system (shown in Fig. 2.2) is a spin-triplet with the $m_s = 0$ state (net electron spin projection for the six electrons is 0) split from the $m_s = \pm 1$ states (net electron spin projection for the six electrons is ±1) by 2.88 GHz due to spin-spin interactions between the electrons. An externally applied magnetic field lifts the degeneracy between the $m_s = \pm 1$ states by producing a Zeeman splitting. The continually present magnetic field generated by the nitrogen nucleus associated with the NV center also contributes to the Zeeman shift. This hyperfine interaction makes the energy of the electron $m_s = \pm 1$ states dependent on the orientation of the nuclear spin, allowing for coupling between these two systems. The most common nitrogen isotope is ^{14}N which has a spin of 1. This means that the $m_s = \pm 1$ levels each have three hyperfine states corresponding to nuclear spins $m_n = 0, +1, -1$. The $m_n = \pm 1$ states are split above and below the $m_n = 0$ state by 2.2 MHz. In addition to this, there is a quadrapole interaction that splits the $m_n = \pm 1$ hyperfine states from the $m_n = 0$ state by 5 MHz for all electron spin states.

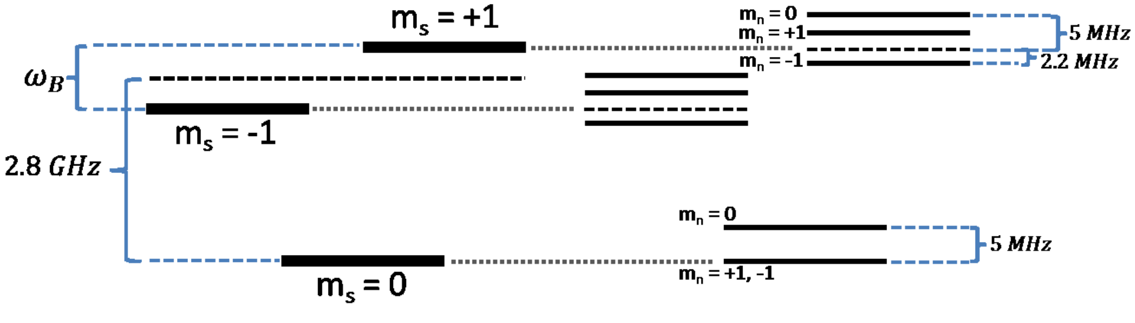

Figure 2.2. NV center electronic ground spin state structure including zero-field splitting (2.88 GHz), Zeeman splitting (ω_B), hyperfine splittings (2.2 MHz), and quadrapole splitting (5 MHz).

The excited state structure is more complicated. The orbital occupation, shown in Fig. 2.1., creates a pair of triplet states. These six states are commonly labeled $|A_1\rangle$, $|A_2\rangle$, $|E_x\rangle$, $|E_y\rangle$, $|E_1\rangle$, $|E_2\rangle$ based on their symmetry properties. The spin-orbit interaction splits states with different total angular momentum, separating the pairs ($|A_1\rangle$, $|A_2\rangle$), ($|E_x\rangle$, $|E_y\rangle$), and ($|E_1\rangle$, $|E_2\rangle$) from each other by about 5 GHz. The spin-spin interaction shifts non-zero spin states ($|A_1\rangle$, $|A_2\rangle$, $|E_1\rangle$, $|E_2\rangle$) up and zero spin states ($|E_x\rangle$, $|E_y\rangle$) down by about 1 GHz. It also splits $|A_1\rangle$ and $|A_2\rangle$ by about 3 GHz. The result is that, for low strain, states $|A_1\rangle$, $|A_2\rangle$, $|E_{x,y}\rangle$, and $|E_{1,2}\rangle$ are separated from each other by large energy gaps.

Optical transitions between the ground and excited states correspond to a zero phonon line at 637 nm. Angular momentum conservation determines which ground states couple to which excited states and sets selection rules on photon polarization. The $|E_{x,y}\rangle$ states couple to the ground $m_s = 0$ state via horizontal and vertical linearly polarized light respectively, and the $|A_1\rangle$, $|A_2\rangle$, and $|E_{1,2}\rangle$ states couple to the ground $m_s = \pm 1$ states via right and left circularly polarized light. These transitions only become narrow enough to drive directly at low temperature.

Crystal lattice strain can break the xy-symmetry and cause the excited states to spit and mix. The ground states, with their anti-symmetric combination of e_x and e_y orbitals, are much less sensitive to strain. The local strain varies throughout the crystal lattice, so the exact excited state splittings are unique to each NV center.

There also exists a continuum of vibronic states which allow phonon assisted absorption at higher energies and emission at lower energies. The former means that the NV center can be excited using, for instance, a green 532 nm laser even at room temperature. The latter causes the NV center to emit much of its fluorescence into a phonon sideband.

The optical transitions are in general spin conserving, however there exists a non-radiative pathway via a pair of additional ground, metastable singlet states whereby the system can decay from an excited state with $m_s = \pm 1$ into the ground state with $m_s = 0$ (See Fig. 2.3). This provides an important mechanism for initialization of the spin state. Under continuous optical excitation at 532 nm, all optical transitions are driven. Any population in the $m_s = \pm 1$ branch eventually leaks out via this pathway into the $m_s = 0$ branch causing optical pumping into the ground $m_s = 0$ state. Since it relies on off-resonant excitation, this initialization process is effective even at room temperature. This also works as a method of spin measurement since the initial fluorescence under green illumination (before spin polarization occurs) is spin dependent, with the $m_s = \pm 1$ states spending time in the metastable singlet states and therefore fluorescing more weakly.

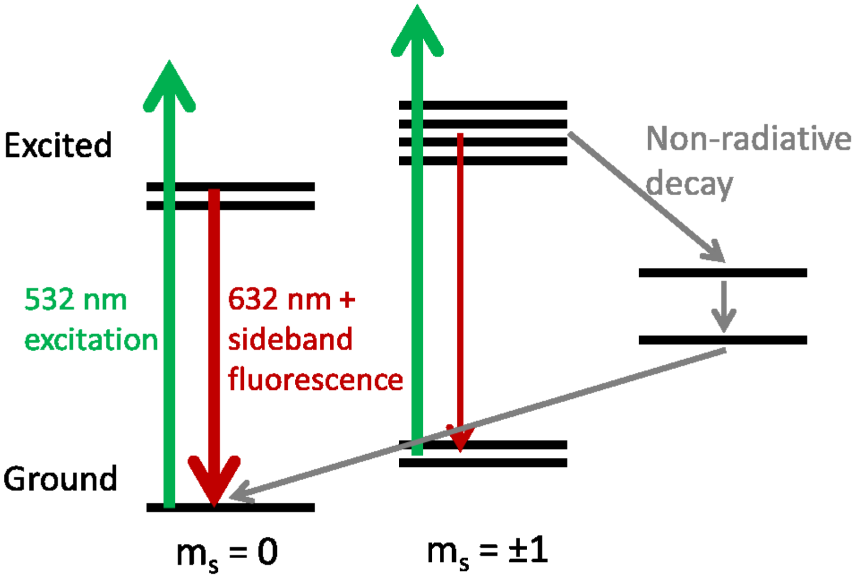

Figure 2.3. Energy level structure of the NV center, demonstrating spin-dependent fluorescence and spin-state polarization under off-resonant optical excitation. Ground and excited state levels are grouped by their spin value.

Under continued resonant excitation the NV center has a probability of being ionized and switching into the neutrally charged state which has different spin properties and resonances. An additional benefit of green illumination is that it can change the charge state, recovering a negatively charged NV center. However this comes at the cost of spectral diffusion. The resonance of the NV center is slightly Stark shifted due to its electronic environment, and the green laser can rearrange this environment changing the position of the resonance.

The primary source for decoherence of the NV center spin state is the surrounding bath of ^{13}C atoms which have a non-zero spin. The concentration of this isotope in the crystal varies from sample to sample and even within the same sample. The coherence time (T_2) for the NV center ground spin states can be as long as milliseconds in very pure samples. Even in a less pure diamond, coherence times of hundreds of microseconds are readily observed. Ground state dephasing times (T_2^*) also vary, but are typically a microsecond or better. These impressive coherence times, which do not require low temperatures, further increase the attractiveness of this solid-state system.

2.2. NV Center Applications

Ensemble NV center impurities in diamond were studied as far back as the 1960s. The center's basic properties were determined over the course of a few decades using optical spectroscopy with irradiation and annealing [38]-[40], electron-spin resonance [41], spectral hole burning [42], and optically detected magnetic resonance (ODMR) [43] methods. Beginning in the 1990s studies using single NV centers began, with demonstrations of confocal optical microscopy and ODMR [44] and photon antibunching [45].

In the last decade experimentalists turned their attention to accomplishing coherent quantum control and other basic building blocks of quantum information science in single NV centers at room temperature. This began with MW-driven Rabi oscillations and Hahn echo measurements [46].The interaction of the NV center with the surrounding spin bath, and the resulting decoherence effects were studied [47], [48]. This allowed the essential requirements for quantum gates, along with state mapping between two quantum systems, to be demonstrated by using the hyperfine interaction between the NV center electronic state and the nuclear spin of nearby ^{13}C atoms [49]-[51], and N atoms [52], [53], and later with the N atom associated with the NV center itself [54], [55]. These techniques led to single-shot readout of single nuclear spins [56] and the use of NV centers for high sensitivity magnetometry [57], [58].

Low temperature studies of single NV centers began with optical spectroscopy in bulk diamond [59], [60] and in nano-diamonds [61] revealing the details of the spin excited state structure. Once the various transitions and selection rules had been sorted out, entanglement between NV center spins and optical photons could be realized [62]. This was followed by demonstrations of quantum interference between single photons emitted from two separate NV centers [63], [64], leading finally to entanglement between these two remote spin states [65].

Progress has also been made toward low temperature coherent optical manipulation of NV center spin states. Experiments have demonstrated CPT [66], optical Rabi oscillations [67], optical cooling of nuclear spins [68], and resonant, optical initialization and readout of NV spin states [69]. The research presented in this dissertation involving CPT and all-optical control contributes to this ongoing effort [70]-[72].

CHAPTER III

EXPERIMENTAL METHODS

In this chapter we lay the groundwork for the central experimental results which are the subject of the following chapters. We begin with a description of our experimental setup. After this we present preliminary, low-temperature experimental investigations of the NV center and in the process introduce the basic methods of spin preparation and measurement which appear in our main experiments.

3.1. Experimental Setup

To optically excite and collect fluorescence from a single NV center we use a standard confocal microscope setup (see Fig. 3.1). The same objective (Olympus LUCPLFLN40, .6NA, 40x magnification) focuses the excitation lasers onto the sample while collecting emitted fluorescence. Galvanometer mirrors (Thorlabs, GVSM002) steer the laser beams and, with them, the position of the focal spot in the focal plane. A dichroic mirror (longpass cutoff at 550 nm) and a series of filters (532 nm notch, 637 nm notch, 647 nm cutoff longpass) block out any reflected laser light while passing the phonon sideband of the fluorescence. This fluorescence is coupled into a single mode optical fiber which acts as a pinhole to reject any light not coming from the focal plane of the microscope. For some of our experiments we instead used a multimode fiber with a small core diameter (10 μm). The fiber then couples into an avalanche photodiode

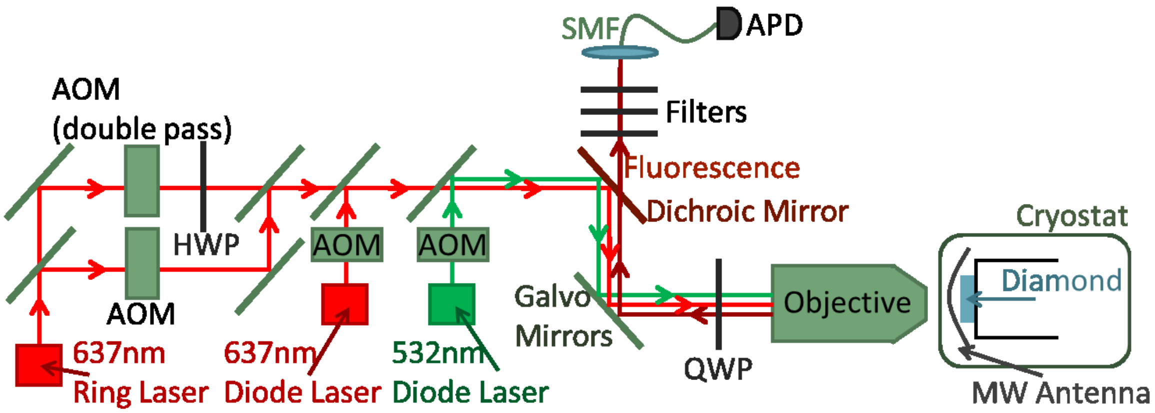

Figure 3.1. Diagram of the experimental setup.

(Perkin-Elmer, SPCM-AQR-16-FC) for single photon counting with a counting card (National Instruments, PCI 6602).

Beams from a 532 nm diode laser (Laserglow, LCS-0532), a 637 nm tunable diode laser (New Focus, Velocity 6304), and a 637 nm frequency stabilized tunable dye ring laser (Coherent, 899-21) each pass through acousto-optic modulators (AOMs) allowing them to be independently pulsed. Many of our experiments require two, oppositely circularly polarized, phase locked, 637 nm radiation fields. To achieve this we split the ring laser beam into two, cross linearly polarize them using a half-wave plate, and send them through separate AOMs. A double pass configuration on one of the AOMs allows for a greater range of frequency tuning while keeping the beam position stable. The two beams are recombined before being sent to the sample. A quarter-wave plate immediately before the objective changes the polarization of the two beams into the desired circular polarizations.

The experiments discussed in this paper all involve resonant optical excitation of the NV center and so must be performed at low temperatures. The diamond sample is mounted inside of a coldfinger, optical, helium flow cryostat (either an open cycle (Advanced Research Systems, LT-103) or a closed cycle (Montana Instruments, Cryostation)) and kept at approximately 7 K. An objective with a particularly long working distance (3.4 mm) and an adjustable cover slip correction collar allows optical access through a window in the cryostat.

We used a type IIa diamond sample with a density of NV center impurities in the parts-per-billion range. In order to improve our fluorescence collection efficiency, we used a focused ion beam to mill a solid immersion lens (SIL) directly onto the surface of the diamond [73], [74]. Diamond has a high index of refraction (2.42), lowering the effective NA of our objective. The SIL geometry ensures that any light rays originating from an emitter located at the center of the SIL will leave the diamond normal to the surface, eliminating refraction. We made multiple SILs and looked for one containing an NV center with good properties at a location near the center of the SIL. Fig. 3.2 shows a scanning electron microscope image of the SIL. An additional advantage of using a SIL is that this relatively large feature (11 μm diameter) makes the position of a particular NV center easy to relocate. This made it possible to perform nearly all the experiments described in this dissertation on the same NV center.

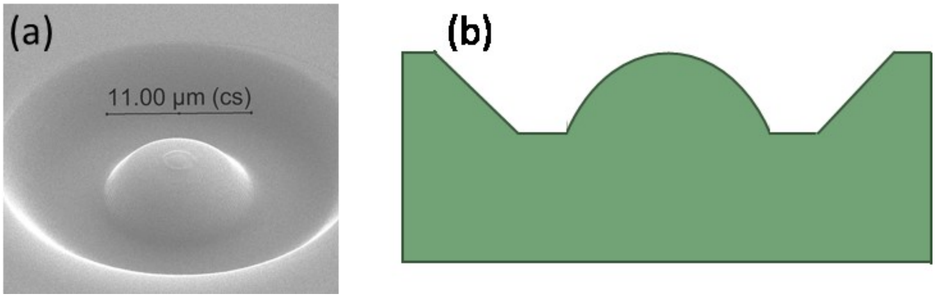

Figure 3.2. (a) SEM image of the SIL. (b) Profile of the SIL shape.

To apply MW radiation to the NV center we use a thin (approximately 20 μm diameter) bonding wire, stretched over the sample, as an antenna. The signal from a radio-frequency signal generator (Agilent, 8648C) is modulated for the desired pulse sequence and amplified (typically to a power between approximately 20 mW and 4 W) before being sent to the antenna. For experiments where two MW fields are needed, we use two phase-locked signal generators and combine the two signals using a frequency splitter.

A small permanent magnet mounted close to the sample but outside of the cryostat produces a ground state Zeeman splitting. A pulse generator (Spin Core, Pulse Blaster ESR-PRO-400) creates the pulse sequence for a given experiment, synchronizing the AOM's, MW excitation, and photon counting. A separate pulse generator (Tektronix, AFG 3052C) was used for driving the red laser AOM's in a few of the STIRAP experiments where more controllable pulse shapes were needed.

3.2. Preliminary Low-Temperature Investigations

We now describe a few basic NV center experiments and the experimental methods involved. Confocal imaging scans locate single NV centers. PLE measurements show the electronic excited state structure and provide a means of spin detection. ODMR measures the ground state Zeeman splitting and reveals hyperfine coupling. And Rabi oscillation experiments demonstrate MW spin control.

3.2.1. Confocal Imaging of Single NV Centers

The confocal microscope setup provides a spatial resolution in the x, y, and z dimensions on the order of 1µm. A scan, in the x-y plane, of the focal spot from a 532 nm laser, combined with the collection and measurement of any emitted fluorescence, produces a two-dimensional image of NV centers in the focal plane of the objective. An example of such a scan is shown in Fig. 3.3.

The faint, circular feature in this image is the SIL which is being scanned over. The bright spots are individual NV centers. The variations in brightness are due to the fact that different NV centers are closer to the focal plane. Additionally there are four possible spatial orientations for the NV center, defined by the direction of the center's dipole with respect to the crystal lattice [75]. These occur randomly and affect how efficiently the center will absorb the incoming radiation and as well as how much of its fluorescence will be emitted in the direction of the microscope. The NV center indicated by the arrow is the one that was used in most of our experiments.

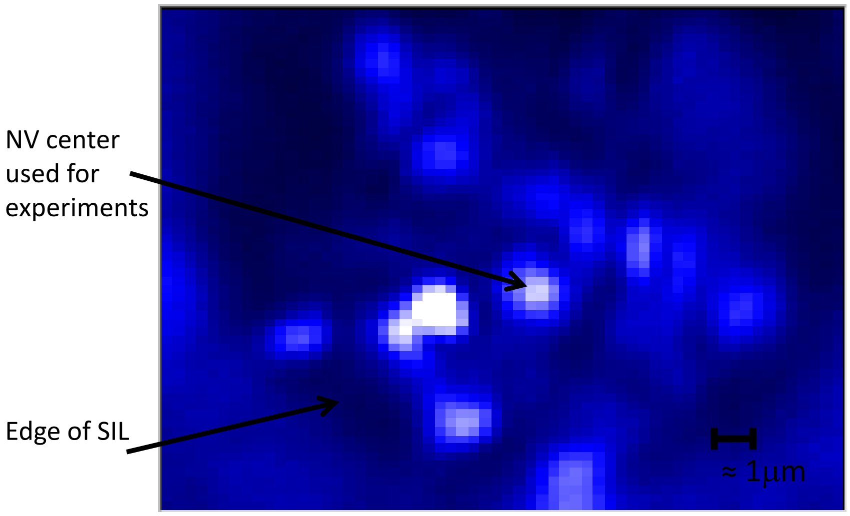

Figure 3.3. 2D fluorescence image. Fluorescence was collected under 532 nm illumination. The bright spots are NV centers. The arrow indicates the NV center that was used.

3.2.2. Photoluminescence Excitation

The zero phonon line of the NV center is at 637 nm. Scanning a laser over this wavelength while collecting phonon-sideband fluorescence reveals the various optical transitions within the NV center spin state structure [60]. The excitation spectrum for the NV center that we used is shown in Fig. 3.4a as is the pulse sequence that produced this measurement. This spectrum is strain dependent and is different for different NV centers. Each peak in the spectrum is labeled by the transition which it represents. In order to access the transitions that couple to $m_s = \pm 1$ as well those that couple to $m_s = 0$, we apply continuous MW excitation that is resonant to the transition between these ground states. The optical transitions of interest for our experiments are $m_s = 0 \rightarrow E_y$, and $m_s = \pm 1 \rightarrow A_2$.

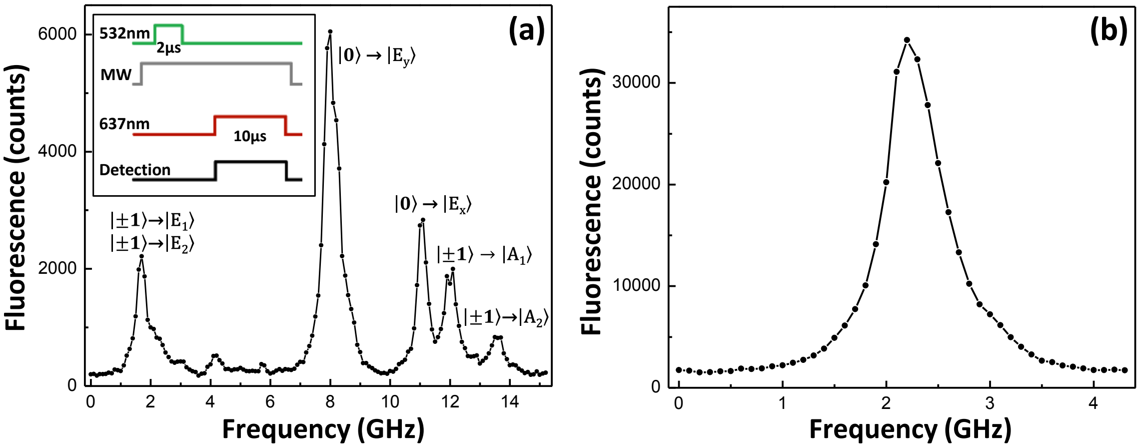

Figure 3.4. (a) PLE spectrum of a single NV center. The frequency of a 632 nm laser is scanned while the sideband fluorescence is collected. Each peak is labeled by the transition it represents. (inset) Pulse sequence used for PLE measurements. (b) PLE scan of the $m_s = 0 \rightarrow E_y$ *transition indicating a broadened linewidth, due to spectral diffusion, of around 600 MHz.*

Continued, resonant excitation can cause optical pumping and ionization. Periodic illumination with a green laser, as discussed in the previous chapter, reverses ionization and reinitializes the spin state. However, this also produces spectral diffusion. The scans shown in Fig. 3.4 effectively sum over this diffusion, resulting in linewidths that appear quite broad. The intrinsic linewidth for the NV center is approximately 13 MHz [76]. The PLE peak corresponding to the transition to E_y, shown in Fig. 3.4b, indicates a linewidth, due to spectral diffusion, of around 600 MHz.

We can investigate the ionization and pumping effects of resonant excitation by limiting our detection time to a small window and scanning it in time relative to the red excitation pulse. The results of this measurement are shown in Fig. 3.5 for two different optical powers. Here the laser is tuned to the $m_s = 0 \rightarrow E_y$ transition. The number of counts detected jumps up when the detection window begins to overlap with the resonant

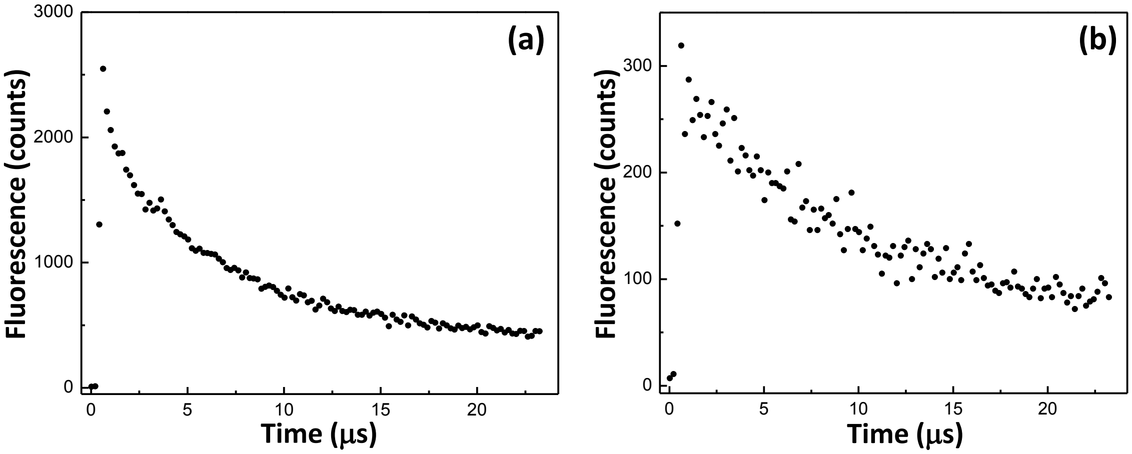

Figure 3.5. Decay of the fluorescence signal under continued (a) high power and (b) low power resonant excitation due to optical pumping and photoionization. This limits the detection time for an efficient PLE spin measurement.

excitation, and then begins to decay as ionization and pumping reduce the fluorescence. The rate of this decay is faster for higher optical power. These processes have been studied in much more detail by others [67], [68, Supplementary Information]. By tuning the laser onto a transition involving the ground state spin whose population we would like to measure, and by limiting the detection window to the beginning of the decay curves shown in Fig. 3.5, PLE becomes a good method for spin measurement. We now apply this measurement technique in demonstrations of ODMR and Rabi oscillations.

3.2.3. Optically Detected Magnetic Resonance

The pulse sequence we use to perform an ODMR measurement is shown in Fig. 3.6a. First, a green pulse initializes the spin state into $m_s = 0$. Next is a MW pulse. This is followed by a PLE measurement of the $m_s = 0$ state population using the red laser tuned to the $m_s = 0 \rightarrow E_y$ transition. The MW frequency is scanned over the 2.88 GHz ground state splitting. When the MWs are on resonance with this transition, some of the population is driven up into the $m_s = \pm 1$ state where it remains due to the long spin state lifetime. The result is a decrease in the resonant excitation leading to a decrease in the emitted fluorescence. The plot in Fig. 3.6b shows the fluorescence as a function of MW frequency. We calibrated the duration of the MW pulse to perform a π-rotation on the spin state (see the next section on Rabi oscillations) so as to maximize the depth of the ODMR dip.

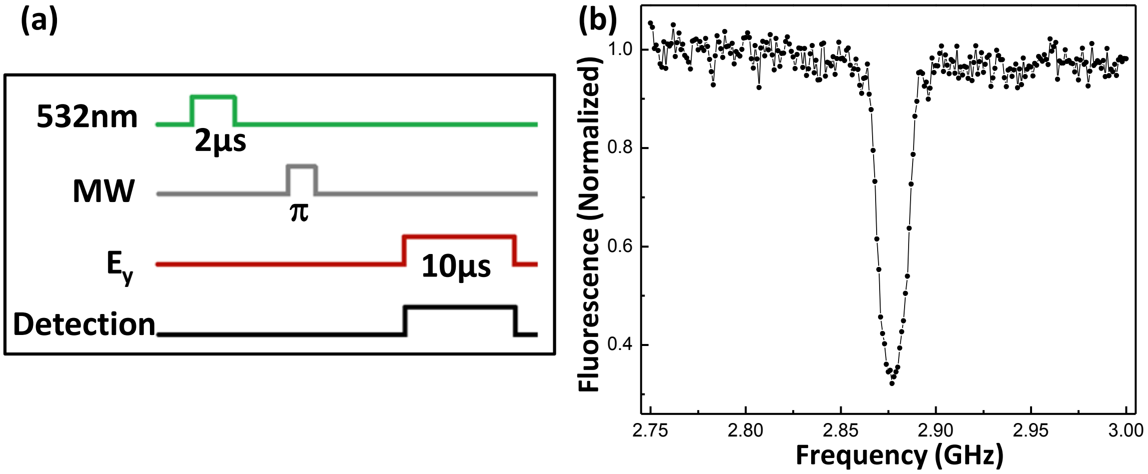

Figure 3.6. ODMR measurement. (a) Pulse sequence. (b) Fluorescence as a function of MW frequency. The single dip corresponds to the $m_s=0 \rightarrow m_s=\pm 1$ ground state transition at 2.877 GHz (at low temperature).

An external magnetic field can lift the degeneracy between the $m_s = \pm 1$ states. Fig. 3.7 shows the ODMR spectrum in the presence of a magnetic field with a strength of a couple millitesla. Two dips are now visible, one corresponding to the $m_s = 0 \rightarrow m_s = +1$ transition and the other to the $m_s = 0 \rightarrow m_s = -1$ transition. The locations of these two dips indicate a Zeeman splitting between the ±1 levels of 155 MHz.

The magnitude of the Zeeman splitting depends on both the strength of the magnetic field and on its orientation with respect to the NV center dipole axis [57]. We hold the distance between the permanent magnet and the diamond sample constant while adjusting the magnet's orientation until the Zeeman splitting is maximized, indicating that the B-field is roughly aligned with the dipole axis.

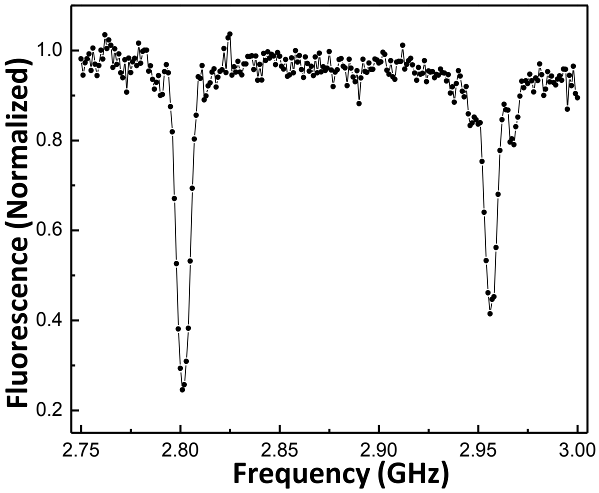

Figure 3.7. ODMR measurement with an external B-field. The left dip corresponds to the $m_s=0 \rightarrow m_s=-1$ *transition, and the right dip corresponds to the* $m_s=0 \rightarrow m_s=+1$ *transition. This indicates a Zeeman splitting between* $m_s=-1$ *and* $m_s=+1$ *of 155 MHz.*

The two ground state transitions have polarization selection rules. Since the MW polarization is fixed by the orientation of the antenna, the coupling to the MWs is not the same for both transitions [77]. The MW pulse we used was a π-pulse for one transition but not the other, leading to the asymmetry apparent in the depths of the two dips.

The width of the ODMR dip is limited by dephasing to about 1 MHz. (See the Ramsey fringe measurements presented in Chapter V and the discussion of dephasing in Chapter VI.) Additionally the transition exhibits a significant power broadening. When the MW power is decreased, and consequently the π-pulse time length is increased, the hyperfine structure described in Chapter II is revealed. Fig. 3.8 shows the ODMR spectrum for one of the ground state transitions with high and low MW power. In the low power case three dips are now visible, split by 2.2 MHz, corresponding to the three

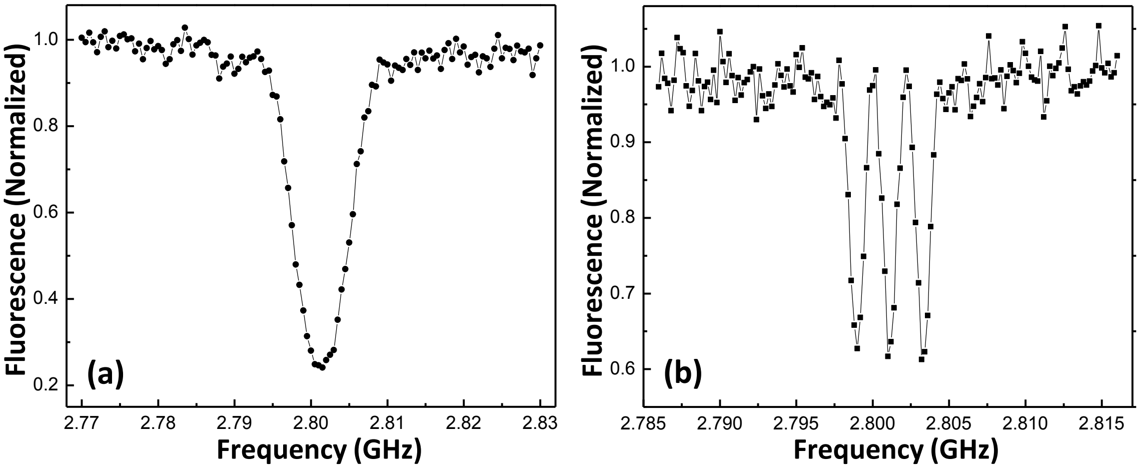

Figure 3.8. ODMR measurement of the m_s=0 → m_s=-1 transition with (a) high MW power (π-pulse = 120 ns) and (b) low MW power (π-pulse = 790 ns). The three dips in (b) correspond to the three hyperfine states, due to coupling with the ^{14}N nuclear spin, and exhibit a splitting of 2.2 MHz.

^{14}N nuclear spin states. This indicates the possibility of performing nuclear spin dependent electron spin flips [51].

3.2.4. Rabi Oscillations

MW radiation resonant with a ground state spin transition will drive oscillations in the state population. We measure these Rabi oscillations using the same pulse sequence we used for ODMR (Fig. 3.6a), but now the MW pulse duration is varied rather than the MW frequency. Fig. 3.9a displays the results when the PLE measures the population in the $m_s = 0$ state. Alternatively we can measure the population in the $m_s = \pm 1$ states by performing PLE on the transition involving the A_2 excited state. (For the Rabi oscillation measurements the MW field was tuned onto the $m_s = 0 \rightarrow m_s = +1$ transition so only the $m_s = +1$ level was actually populated.) The resulting oscillations,

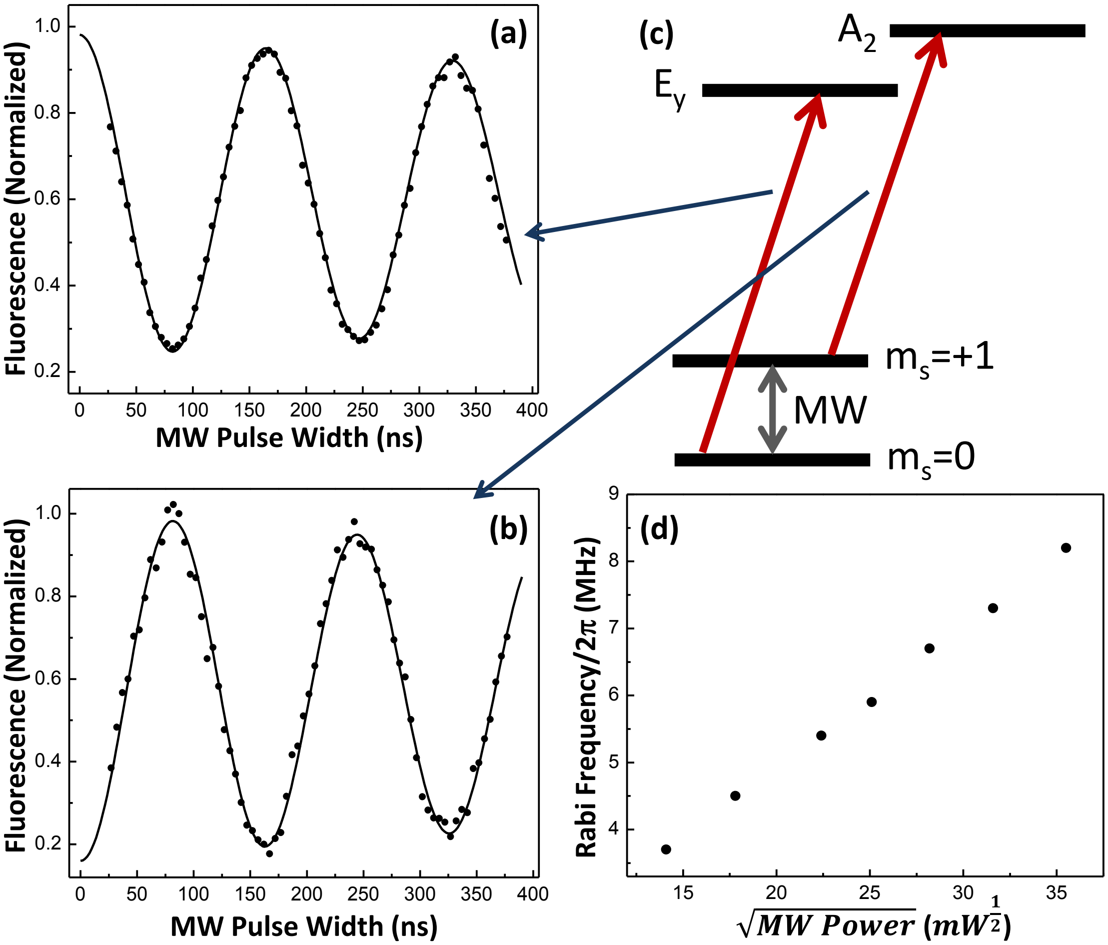

Figure 3.9. Rabi oscillations. The fluorescence from a PLE measurement following a MW pulse is plotted as a function of the MW pulse length. PLE is measured from the m_s=0 → E_y,(a) and m_s=+1 → A_2 (b) transitions as indicated in the energy level diagram in (c). Solid lines are damped Sine waves fit to the data. (d) Rabi frequency as a function of the square root of the MW power. The expected linear relation is observed. The MW power refers to the power of the RF signal that is sent to the antenna.

shown in Fig. 3.9b, start low since the spin was initialized into $m_s = 0$. Thus the phase of the Rabi oscillations indicates which ground state is involved in the transition that is being driven in the measurement step. We can use this fact to help confirm the transitions that were assigned to the various peaks in the PLE spectrum shown in Fig. 3.4a. The frequency of the Rabi oscillations will be proportional to the square root of the MW power. In Fig. 3.9d we plot the measured Rabi frequency for different MW powers confirming this dependence.

The long lifetime of these ground state spins makes efficient π-pulses possible. The Rabi oscillations in Fig. 3.9 indicate a π-pulse length of about 80 ns corresponding to complete population transfer from $m_s = 0$ to $m_s = +1$. The fluorescence fails to decrease completely to zero here, primarily due to imperfect spin initialization from the green excitation (typically no better than about 90% [43, Supplementary Information]) as well as slightly unequal contributions from different hyperfine states. This latter effect is minimized even more at higher Rabi frequencies.

The effects of the hyperfine splittings are made more evident when the Rabi oscillations are observed on a longer time scale (Fig. 3.10). A beating is now apparent in the signal. The reason for this is that while the MW field is tuned onto resonance with the hyperfine state $m_n = 0$, it is slightly off resonance from the other two hyperfine states. These two transitions have population oscillations with a slightly different Rabi frequency which are combined with the resonant Rabi frequency. On top of the data in Fig. 2.10 we plot the sum of three Sine waves with frequencies given by Ω, $\sqrt{\Omega^2 + (\pm 2.2MHz)^2}$, and with amplitudes given by A, $A * \frac{\Omega^2}{\Omega^2+(\pm 2.2MHz)^2}$, where Ω and A are the Rabi frequency and amplitude for the contribution from the $m_n = 0$ hyperfine state, and 2.2 MHz is the hyperfine splitting. The Rabi oscillations can also be affected by coupling between the NV center and other spins in its environment [48].

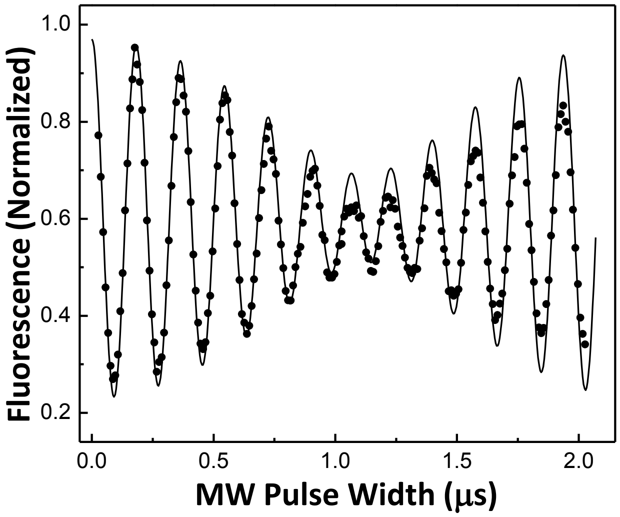

Figure 3.10. Rabi oscillations. The beating is due to coupling between the NV center electron spin and the ^{14}N *nuclear spin. The detuning of the MW field is different for each hyperfine state leading to different Rabi frequencies. The measurement sums over the contributions from all three hyperfine states and exhibits a beating. The solid line is a fit described in the main text.*

The Rabi oscillations shown so far include contributions from all three hyperfine states. As in the ODMR measurement, when the MW power is low enough it will only drive one hyperfine state at a time. This case is shown in Fig. 3.11. Here the population oscillates only when the nuclear spin state is 0. The $m_n = \pm 1$ hyperfine states are unaffected by the MW pulse and contribute a constant background. In this measurement, therefore, a fluorescence drop of at most one-third is expected. These are nuclear spin dependent Rabi oscillations. A π-pulse now represents an electron spin flip conditional on a nuclear spin state.

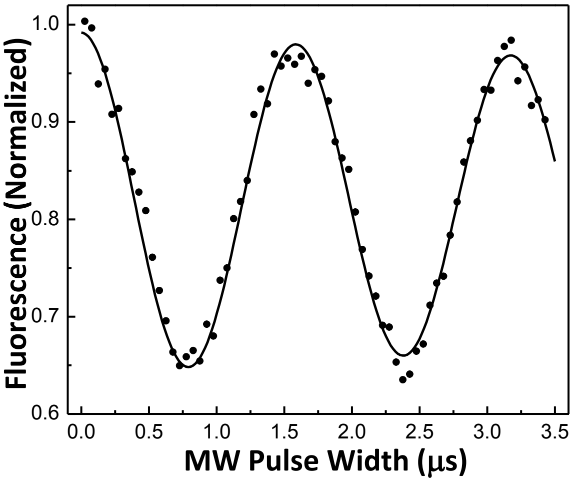

Figure 3.11. Nuclear spin dependent Rabi oscillations. A low MW power only drives one hyperfine state at a time. Solid line is a damped Sine wave fit to the data.

3.2.5. Conclusion

These PLE, ODMR, and Rabi oscillation experiments have demonstrated optical initialization, optical readout, and MW control of NV center spin states. In the rest of this dissertation we will use these abilities to investigate other phenomena such as CPT and dressed states. We will also present methods of replacing the MW control with optical control.

CHAPTER IV

COHERENT POPULATION TRAPPING IN THE NV CENTER

This chapter contains some material that was co-authored with Khodadad N. Dinyari and Hailin Wang in reference [70]. The experiments described here were performed by the author.

CPT measurements are the subject of this chapter. As we will see, these measurements can act as a very sensitive probe of the energy-level structure of the NV center. While ODMR measurements of the ground spin-state structure require MW excitation, CPT provides an optical alternative. We will find this to be useful when working in the context of all-optical control or when we wish to use the MW driven transitions for other purposes.

After a brief review of the theory behind CPT, we describe how we realize it in the NV center. The features of the two-photon Raman-resonant condition along with the concept of the dark state will be relevant to the optical control techniques presented in the following chapter. We also show that the CPT is sensitive to the hyperfine interaction and can therefore be nuclear-spin dependent. Finally we present a CPT measurement of dynamic Stark splitting. This introduces us to the idea of dressed states which will be developed further in Chapter VI.

4.1. Coherent Population Trapping: Theory

The three energy-level system shown in Fig. 4.1 is referred to as a "Λ-configuration". Two lower levels couple to the same upper level via two radiation fields. When δ is zero, the two fields are said to be on Raman resonance, i.e. the detuning between the fields is equal to the splitting between the two lower energy levels. If we also set the dipole detuning, Δ, to zero, the Hamiltonian for the atom-field system (after making the rotating wave approximation and using the rotating frame) is given by $H = \frac{\hbar}{2}(\Omega_a|a\rangle\langle c| + \Omega_b|b\rangle\langle c|) + H.C.$ An eigenstate of this Hamiltonian with an eigenvalue of 0 is $|d\rangle = \frac{1}{\sqrt{\Omega_a{}^2+\Omega_b{}^2}}(\Omega_b|a\rangle - \Omega_a|b\rangle)$. This is referred to as a dark state. It is a superposition of the two ground states and is completely uncoupled from the excited state [27], [78]. What has happened is that destructive quantum interference between the two transitions has cancelled them out. If the system is in the state $|d\rangle$, the excited state will never be populated and the system will not emit fluorescence via spontaneous emission from the excited state; hence the name "dark" state. If the system does not begin in the dark state, the combination of optical excitation and spontaneous emission can pump it into the dark state. The result of all this is that the amount of fluorescence emitted by this system will depend on whether the Raman resonance condition for the two fields is met.

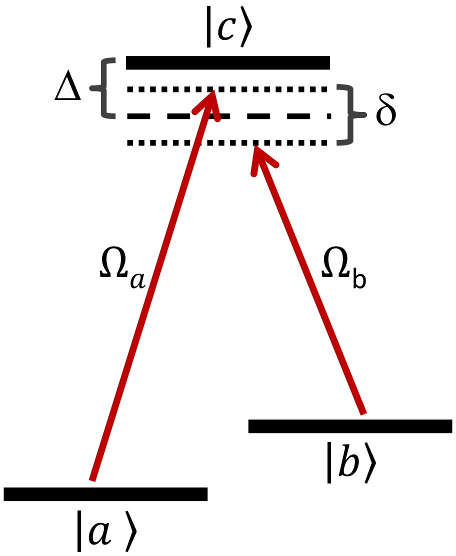

Figure 4.1. Three-level Λ-configuration. The two transitions are driven by two fields with Rabi frequencies of Ω_a *and* Ω_b *and with an overall dipole detuning of* Δ *and a Raman detuning of* δ*.*

4.2. Λ-Type Configuration in the NV Center

To realize CPT it is necessary to have a Λ-type energy level configuration. Electromagnetically induced transparency was first observed in diamond NV centers using ground states and MW driven transitions [79]. The first optical demonstrations of CPT used a Λ-configuration involving both ground and excited states [66], [80], [81]. The ground spin states $m_s = 0$ and $m_s = \pm 1$ formed the two lower levels. Under normal conditions, due to spin conservation, none of the NV excited states will couple to both of these ground states. For this reason, these studies relied on either a very strong external magnetic field or a high level of crystal strain to cause mixing between excited states with different spin. A different Λ-configuration can be formed at low magnetic field and low strain using the ground $m_s = \pm 1$ states as the two lower levels. CPT was recently demonstrated using this configuration [68], and our own CPT measurements used a similar procedure [70].

There exists an excited state, referred to as A_2, that can couple to both the $m_s = +1$ and $m_s = -1$ ground states and so can serve as the top level in the Λ-configuration (see Fig. 4.2a). At zero strain, A_2 has the form $|A_2\rangle = \frac{1}{\sqrt{2}}(|E_-\rangle|+1\rangle + |E_+\rangle|-1\rangle)$ where $|\pm1\rangle$ are the spin states with $m_s = \pm1$, and $|E_\pm\rangle$ are orbital states with orbital angular momentum projections of ±1 along the NV axis [62]. It will decay radiatively, with equal probability, into the $m_s = +1$ and $m_s = -1$ ground states, which have zero orbital angular momentum projection, i.e. $|E_0\rangle|+1\rangle$ and $|E_0\rangle|-1\rangle$ where $|E_0\rangle$ is the orbital state with an orbital angular momentum projection of 0. Optical transitions do not change the spin

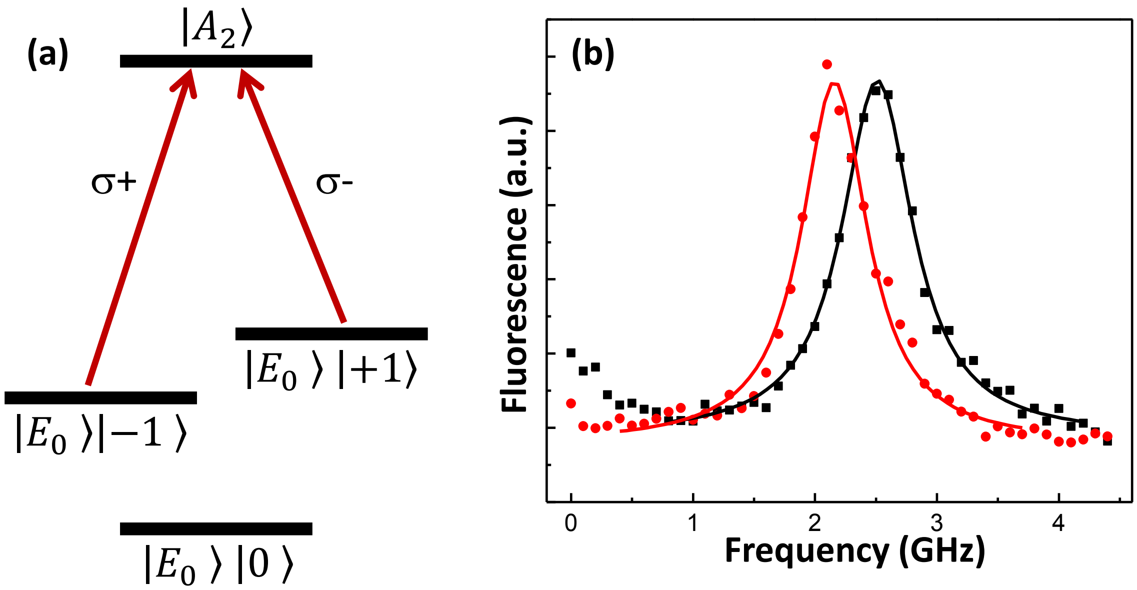

Figure 4.2. (a) Λ-configuration in the NV center. The A_2 excited state couples to the m_s=-1 and m_s=+1 ground states via σ+ and σ- polarized optical fields respectively. From here on we omit the orbital angular momentum component ($|E_0\rangle$) from the labeling of the ground state levels. (b)PLE spectra of the two A_2 transitions indicating a Zeeman splitting of about 500 MHz. Each transition was selected by using a CW MW field tuned to the appropriate ground state transition. The solid lines are Lorentzian fits to the data.

state. In order to conserve the total angular momentum (angular momentum of the photons plus the orbital angular momentum of the electrons), ground state $m_s = +1$ couples to A_2 via σ- polarized light, and ground state $m_s = -1$ couples to A_2 via σ+ polarized light. For large degrees of crystal strain, these selection rules no longer hold, but for low levels they are still approximately correct [82] and have been used for demonstrations of spin-photon entanglement [62]. The excited state level A_1 also couples to both ground states, but it has a significant probability of decaying non-radiatively into the $m_s = 0$ ground state. A_2 does this as well but at a much slower rate [68] making this Λ-configuration a nearly closed system. The lifetimes of the ground spin states are long enough that we can ignore the possibility of decaying out of them.

The polarization selection rules, together with a Zeeman splitting produced by an external magnetic field, allow the two optical transitions in the Λ-configuration to be excited separately. The PLE scans in Fig. 4.2b show these two transitions with a Zeeman splitting of about 500 MHz. A smaller splitting was used for the CPT experiments. To counteract optical pumping into the $m_s = 0$ state due to the off-resonant green excitation used in the PLE measurement, a weak CW MW field was applied, populating the ground state whose transition with A_2 we wished to measure.

As discussed in the previous chapter, the peak in the PLE measurement appears broad due to averaging over spectral diffusion, while the intrinsic linewidth is much sharper. The peaks in Fig. 4.2b overlap significantly, but for each run of the experiment the two transitions can in fact be well distinguished spectrally.

4.3. Coherent Population Trapping: Experiment

For the CPT measurement we use two optical fields of roughly equal power. One is held resonant with the transition between $m_s = +1$ and A_2 while the other is scanned in frequency over the transition between $m_s = -1$ and A_2 (Fig. 4.3a). As in the PLE measurement, a green pulse reverses optically induced ionization, and a weak MW excitation counteracts optical pumping. The results are shown in Fig. 4.3b. Away from Raman resonance no dark state is formed and A_2 can be populated, resulting in a high level of fluorescence. When the detuning between the two optical fields is equal to the Zeeman splitting, Raman resonance is achieved and continued excitation pumps the system into the dark state leading to a drop in fluorescence.

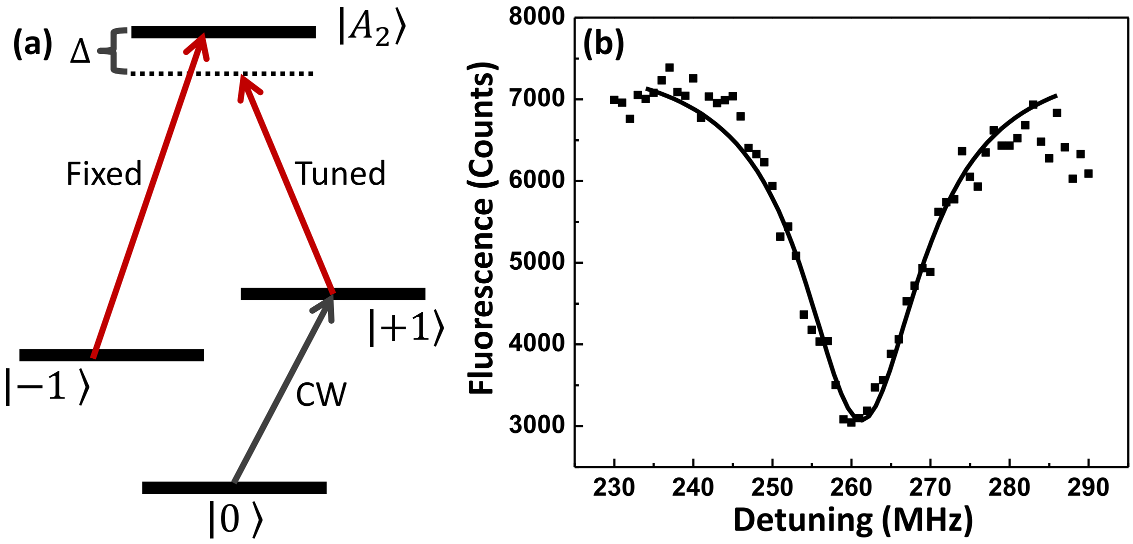

Figure 4.3. (a) Energy-level diagram. Both optical fields have the same power (combined power = 1μW). One is tuned in frequency while the other is held fixed. A weak CW MW field counteracts pumping out of the Λ-configuration due to the off-resonant excitation step. (b) CPT measurement. Away from Raman resonance A_2 is excited and the fluorescence is high. On Raman resonance the system is pumped into the dark state and fluorescence is low. As the location of the dip indicates, a Zeeman splitting of about 260 MHz was used.

Power broadening of the optical transitions leads to a broadening of the CPT resonance. A relatively high optical power (about 1 μW measured before the objective) was used for Fig. 4.3b, resulting in a dip linewidth of about16 MHz. This is much larger than the 2.2 MHz hyperfine splitting, so in order to resolve this splitting we must use a lower optical power.

4.4. Nuclear Spin Dependent Coherent Population Trapping

Since the Zeeman splitting of the $m_s = \pm 1$ states depends on the ^{14}N nuclear spin value, the Raman resonance condition and the CPT measurement do as well (see Fig. 4.4a). To resolve this hyperfine effect, we use a lower optical power (≈ 60 nW). To improve the measurement we also replace the CW MW with a MW π-pulse (on the $m_s = 0 \rightarrow m_s = +1$ transition) which populates the Λ-configuration before the CPT measurement begins (see Fig. 4.4b). A strong π-pulse (Rabi frequency ≈ 5 MHz) ensures that the population is driven into the Λ-configuration regardless of the nuclear spin state. The resulting CPT trace is shown in Fig. 4.4c. Three dips are now visible, each corresponding to the Raman resonance condition being met for a different pair of hyperfine states with equal nuclear spin value. They are separated by 4.4 MHz, twice the hyperfine splitting, since, for instance, the $m_n = +1$ hyperfine state of the $m_s = -1$ spin state is shifted down by 2.2 MHz while the $m_n = +1$ hyperfine state of the $m_s = +1$ spin state is shifted up by 2.2 MHz.

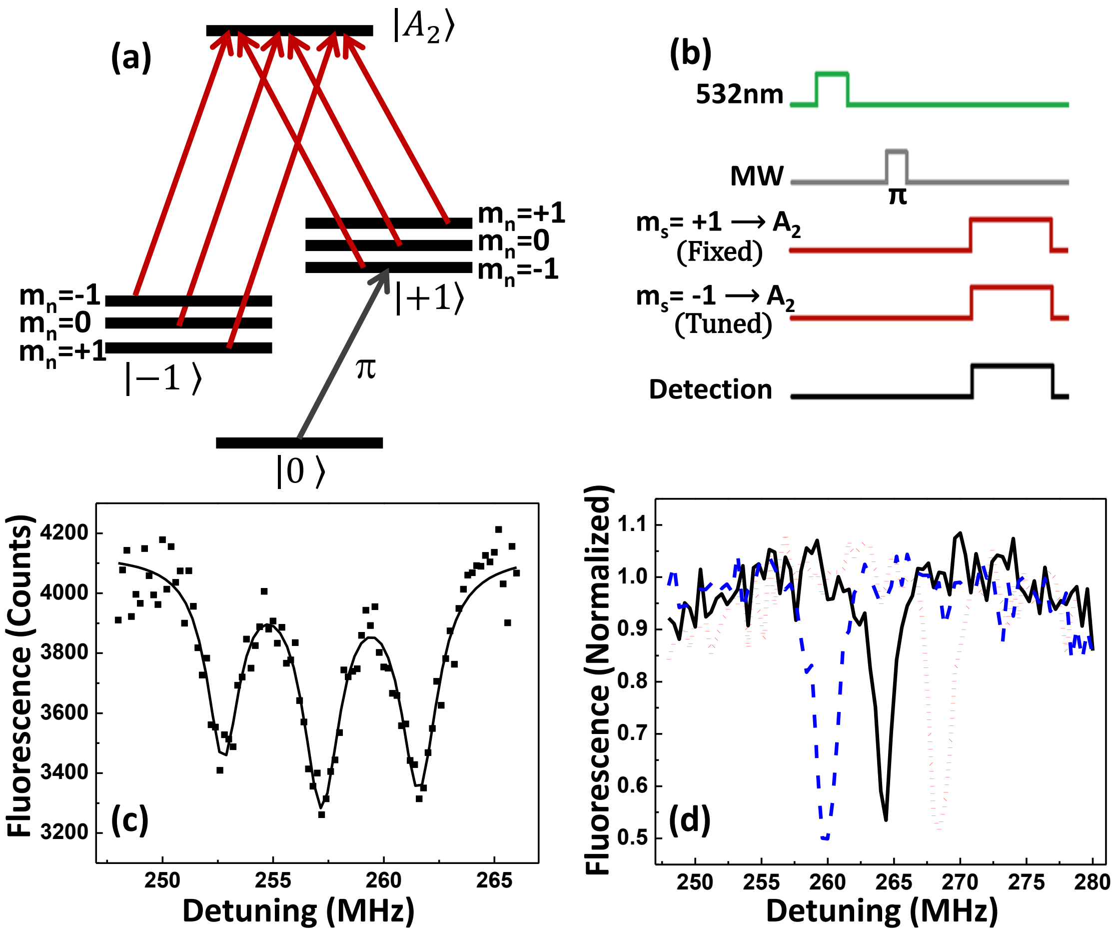

Figure 4.4 Nuclear spin dependent CPT. (a) Energy-level diagram indicating the three hyperfine Raman resonance conditions.(The quadrapole splitting shown in Fig. 2.2 is left out since it is the same for all spin states and therefore irrelevant to CPT.) (b) Pulse sequence. (c) CPT measurement using low optical power (combined power = 60 nW) and a strong MW π-pulse. All three hyperfine states are visible. The solid line is a fit to three Lorentzians. (d) Three different CPT traces obtained using low optical power and a weak MW π-pulse populating the $m_n = -1$ *(blue, dashed line),* $m_n = 0$ *(black, solid line), or* $m_n = +1$ *(red, dotted line) hyperfine state. (A different Zeeman splitting was used in each of the CPT measurements shown so far.)*

The CPT plot represents the sum of many individual CPT measurements and includes equal contributions from each of the hyperfine states. This produces a background for each of the dips. When the Raman resonance condition is met for one pair of hyperfine states, it is not met for the other two; and these cases will contribute fluorescence.

To improve the contrast, as well as confirm the hyperfine nature of these resonances, we use a weak MW π-pulse (≈ 0.8 MHz, small compared with the hyperfine splitting) during the initialization step. This can put population into the Λ-configuration for only one hyperfine state at a time. In other words it produces a nuclear-spin-dependent electron spin flip. Now only one CPT dip is observed, and its location depends on which hyperfine state was addressed by the MW π-pulse in the initialization step (Fig. 4.4d). The two states not addressed by the MWs never enter into the Λ-configuration and remain dark for the entire experiment.

The contrast of the CPT dip is likely limited by several factors. As discussed earlier, population in the A_2 state has a small probability of decaying into the ground $m_s = 0$ state where it goes dark regardless of whether or not the Raman resonance condition is met by the optical fields. This, combined with optically induced ionization events, reduces the "high" count level in the CPT trace. Furthermore, on Raman resonance the system takes a finite time to pump into the dark state, during which it still emits fluorescence. This, plus background due to imperfect initialization and selection rules, prevents the CPT dip from reaching zero.

4.5. Dynamic Stark Splitting Measured by Coherent Population Trapping

We have shown that CPT in the NV center can be an effective measurement of individual nuclear spin states due to its sensitivity to the hyperfine interaction. We now demonstrate that CPT is also responsive to the coherent spin dynamics of this coupled electron-nuclear spin system.

4.5.1. Dynamic Stark Splitting Introduction

When a field couples to the transition between the levels of a two-level system it will drive population oscillations. Looking at it a different way we can treat this as an effective splitting of each level (see Fig. 4.5 for the case where the driving field is on resonance). This is referred to as dynamic Stark splitting (also Autler-Townes splitting) [78], [83]. We can think about this in terms of dressed states. A “dressed” state is an eigenstate of a combined atom-field system. The dynamic Stark splitting is just the splitting between dressed states, while the effective energy levels are just different dressed state components of the bare (non-dressed) spin states. We will discuss dressed states in more detail in Chapter VI.

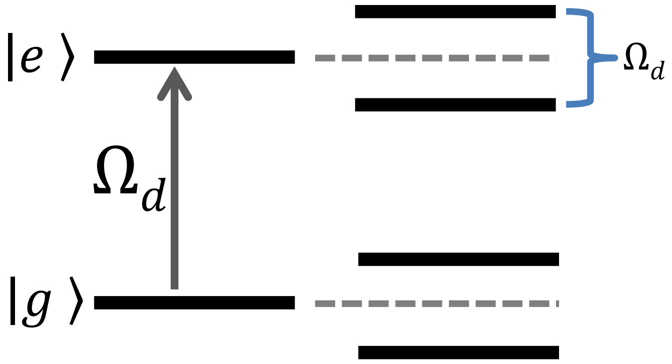

Figure 4.5. Dynamic Stark splitting of a two-level system coupled resonantly to a field with Rabi frequency Ω_d.

For a dressing field with a resonant Rabi frequency of Ω_d and a detuning of δ_d, the split states are shifted by an amount given by

$$\frac{1}{2}(\delta_d \pm \sqrt{{\delta_d}^2 + {\Omega_d}^2}). \tag{4.1}$$

This effect can be observed with an electromagnetically induced transparency measurement [84], [85] and, as we shall see, with a CPT measurement.

4.5.2. Measurement of Dynamic Stark Splitting

We repeat the measurement performed in Fig. 4.4c with all three hyperfine states visible, but now with the addition of a new, continuous MW field (on the ground state transition that is not addressed by the MW π-pulse). This field is present during the optical excitation and produces a dynamic Stark splitting of the ground states.

Fig. 4.6 shows the resulting CPT trace when the continuous MW field is resonant with the ground state transition for the $m_n = 0$ hyperfine state. The dynamic Stark splitting of this state is visible as a splitting of the central CPT dip. The other two hyperfine states exhibit a slight shifting and splitting that is difficult to observe in this CPT trace. The magnitude of the dynamic Stark splitting, and therefore the distance between the two central CPT dips, is dependent on the power of the continuous MW field. CPT traces for three different MW powers are shown in Fig. 4.6 where the Rabi frequencies were determined with Rabi oscillation measurements.

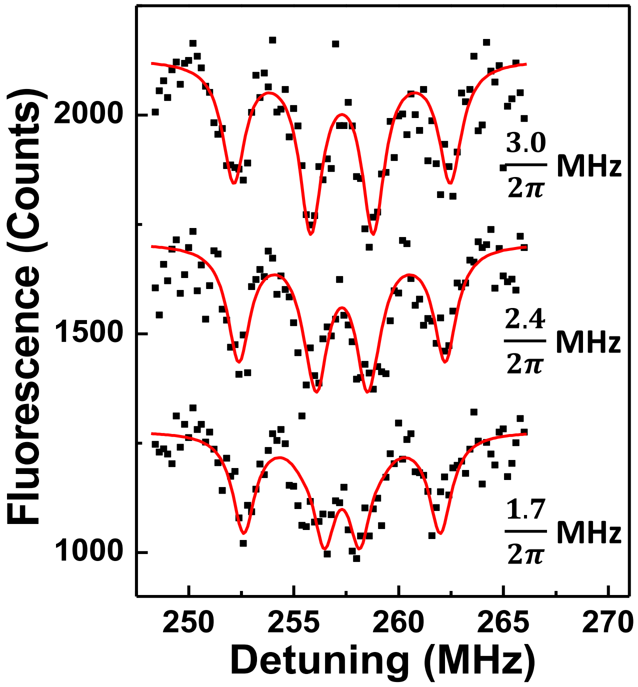

Figure 4.6. CPT measurement of dynamic Stark splitting for different MW powers (vertically offset). A CW MW field is applied to the ground state transition for the $m_n = 0$ hyperfine state during the CPT measurement. The center CPT dip is split by an amount dependent on the strength of this field. Traces are labeled by the experimentally determined MW Rabi frequency. Solid lines are a theoretical fit as described in the main text.

Fig. 4.7 represents the same measurement, but now the MW power is held constant (Rabi frequency ≈ 4/2π MHz) and each CPT trace corresponds to a different MW detuning. The splitting and shifting of the hyperfine states depends on this detuning. As many as six different CPT dips can now be observed, two for each hyperfine state.

Plotted on top of the data in Figs. 4.6 and 4.7 is the sum of multiple Lorentzians with spectral positions that were calculated using (4.1) along with the experimentally determined MW Rabi frequency and the detuning for each hyperfine state. These spectral positions show good agreement with the measurements. The depths and linewidths of the fitting curves were chosen to fit the data.

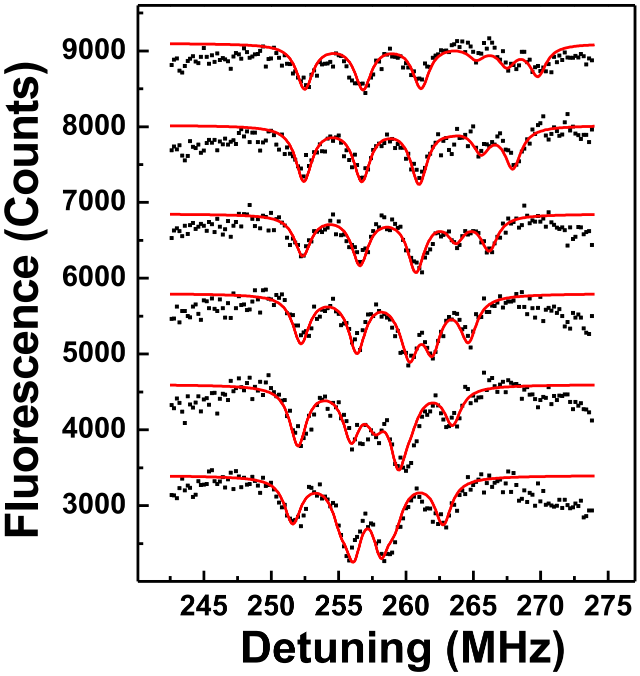

Figure 4.7. CPT measurement of dynamic Stark splitting for different MW detunings (vertically offset). For the top trace, the MW frequency is 9.9 MHz above the ground state transition for the $m_n = 0$ *hyperfine state. For each succeeding trace, the frequency is shifted down by 2 MHz. Solid lines are a theoretical fit as described in the main text.*

4.6. Conclusion

We have seen that CPT measurements in the NV center not only measure the electronic spin states of this system, but are also sensitive to the interaction of these states with both nuclear spins and with a coherently coupling radiation field.

CPT can be a robust form of optical measurement. The Raman resonance condition is not affected by spectral fluctuations in either the optical transition or the laser that produces the optical fields (assuming of course that the two fields are derived from the same laser). This makes processes that rely on this condition attractive for the optical control purposes that we pursue in the next chapter.

Also the width of the CPT dip is not limited by the intrinsic linewidth of the optical transitions but, rather, reflects the coherence between the two ground states, which in the NV center can be quite sharp. Consequently we can use CPT as a measure of this coherence; and we do exactly this in Chapter VI. (However the CPT dip width is, as we shall see, limited by optical power broadening.)

The mechanisms behind CPT could also be used to achieve spin control and detection with a high degree of spatial resolution which may be useful, for instance, in implementing scalable quantum logic gates in chains or clusters of closely spaced NV centers [86].

CHAPTER V

ALL-OPTICAL CONTROL OF THE NV CENTER

This chapter contains some material that was co-authored with Hailin Wang in reference [71]. The experiments described here were performed by the author.

Most demonstrations of spin control in the NV center have relied on MW fields to directly drive transitions between the long-lived spin ground states. However this manipulation method comes with some disadvantages. To realize full all-optical control we need to combine new techniques for optical manipulation with the well-established optical state initialization and readout. In this chapter we develop such techniques.

After a short comparison between MW and optical control, we explore two methods of optical control. First we demonstrate decoherence protected, optically driven Rabi oscillations (ODROs) by driving a two-photon transition. We show that this control can be nuclear spin dependent and then use it to perform a Ramsey fringe measurement. Second we implement stimulated Raman adiabatic passage (STIRAP) which represents spin control via the coherent evolution of a dark state. We experimentally compare the two methods and theoretically analyze the effects of different decoherence processes to determine the relative strengths and weaknesses of each method.

These optical control techniques make possible some applications that are important for scalable quantum information processing. At the end of this chapter we briefly present preliminary investigations into one such application: subwavelength spatial resolution.

5.1. MW Control versus Optical Control

Experimenters have realized some impressive accomplishments using MW control of the spin state of the NV center. Reliance on MW control, however, is subject to several limitations. The first is resolution. Both spectral and spatial resolutions are poor under MW control. The ground state zero-field and Zeeman splittings are similar for all NV centers (assuming they experience the same B-field) making separate NV centers difficult to resolve spectrally. The high degree of sensitivity to strain exhibited by the excited states means that even closely spaced NV centers can have optical resonances that are separated by a few GHz. Furthermore, unlike with MW excitation, it is easy to achieve spatially wavelength-limited optical excitation using far-field optics. There are schemes for achieving subwavelength resolution which use both optical and MW fields. The optical control methods which we present can be extended to accomplish subwavelength resolution that is all-optical.

A second difficulty of using MW control is that it requires specific on-chip infrastructure (e.g. antennas, striplines), which makes sample preparation more complex and could prove a hindrance to scalability. If one is already using optical fields for state preparation and measurement, as most NV center applications do, it makes sense to put state manipulation into this category as well.

Finally, many interesting applications and scalability schemes require either spin-photon or spin-phonon coupling using optical cavities or nanomechanical oscillators respectively. All-optical control would obviously fit nicely into cavity QED scenarios [87]. As for spin-phonon coupling [88], it has already been mentioned that the sensitivity to lattice deformations is much stronger for the excited states than for the ground states.

Unlike the MW transitions, the optical transitions couple to these excited states; and so the opportunity is there for phonon-assisted optical transitions which would mean phonon-assisted spin transitions.

A primary challenge to the use of optical control is the rapid decoherence of these transitions due to radiative decay. The first demonstrations of optical control in NV centers relied on resonant optical excitation to drive Rabi oscillations between a ground and an excited state [67]. The results were limited by a short pure dephasing time (about 10 ns). The lifetime of the excited state is also short (about 11 ns). The optical control methods we use depend on a Raman two-photon resonance which allows for spin control without ever populating the unstable excited state, potentially yielding much longer coherence times. A similar all-optical control scheme has recently been demonstrated that relied on an excited-state spin anticrossing [89].

5.2. Optically Driven Rabi Oscillations with a Two-Photon Transition

The first optical control method we examine is the driving of ODROs between ground spin states via a two-photon transition in a Λ-configuration [90]. First we look at the theory and then the experiments. After that we show that the control is nuclear spin dependent. Lastly we demonstrate the viability of this control method for other applications by using it to perform a Ramsey fringe measurement.

5.2.1. Two-Photon ODROs: Theory

The Hamiltonian for the three-level Λ-configuration described in Chapter IV (Fig. 4.1 with the states $|a\rangle, |b\rangle$, and $|c\rangle$ replaced with $m_s = -1$, $m_s = +1$, and A_2 respectively) is given by

$$H = \begin{pmatrix} \Delta - \frac{\delta}{2} & 0 & \frac{\Omega_-}{2} \\ 0 & \Delta + \frac{\delta}{2} & \frac{\Omega_+}{2} \\ \frac{\Omega_-}{2} & \frac{\Omega_+}{2} & 0 \end{pmatrix} \tag{5.1}$$

where we have taken the rotating wave approximation and used the rotating frame. Δ is the average dipole detuning, δ is the detuning from Raman resonance, and Ω_+ and Ω_- are the Rabi frequencies associated with each field. For $\delta = 0$, and $|\Delta| \gg \Omega_+, \Omega_-$ we can adiabatically eliminate the excited state and write an effective Hamiltonian for just the two lower states

$$H_{eff} = -\frac{1}{4\Delta}\begin{pmatrix} {\Omega_-}^2 & \Omega_+\Omega_- \\ \Omega_+\Omega_- & {\Omega_+}^2 \end{pmatrix}. \tag{5.2}$$

H_{eff} describes a two-level system undergoing Rabi oscillations with a Rabi frequency given by

$$\Omega_R = \Omega_+\Omega_-/2\,|\Delta|. \tag{5.3}$$

This means that when the two fields are tuned to Raman resonance, and the overall dipole detuning is large enough, the system behaves like a two-level system being driven by a single field on resonance [91].

5.2.2. Two-Photon ODROs: Experiments

To demonstrate these Rabi oscillations in the NV center we employ the same Λ-configuration that was used in the preceding chapter to measure CPT. Fig. 5.1 shows the energy level diagram and the pulse sequence that we use to carry out this measurement.

During the initialization step a green pulse first pumps the system into the $m_s = 0$ ground state. This is followed by a strong MW π-pulse which rotates the population into the $m_s = -1$ level (regardless of the nuclear spin state). In the manipulation step two simultaneous, square-shaped, optical pulses are applied. These have nearly equal peak intensity ($\Omega_+ = \Omega_-$), opposite circular polarization, and an extinction ration near 10:1; and they are tuned to be on Raman resonance ($\delta = 0$) but away from the A_2 transition dipole resonance ($\Delta \neq 0$). A two-step PLE measurement provides the spin detection. First, a MW π-pulse drives the population from the spin state we wish to measure into the $m_s = 0$

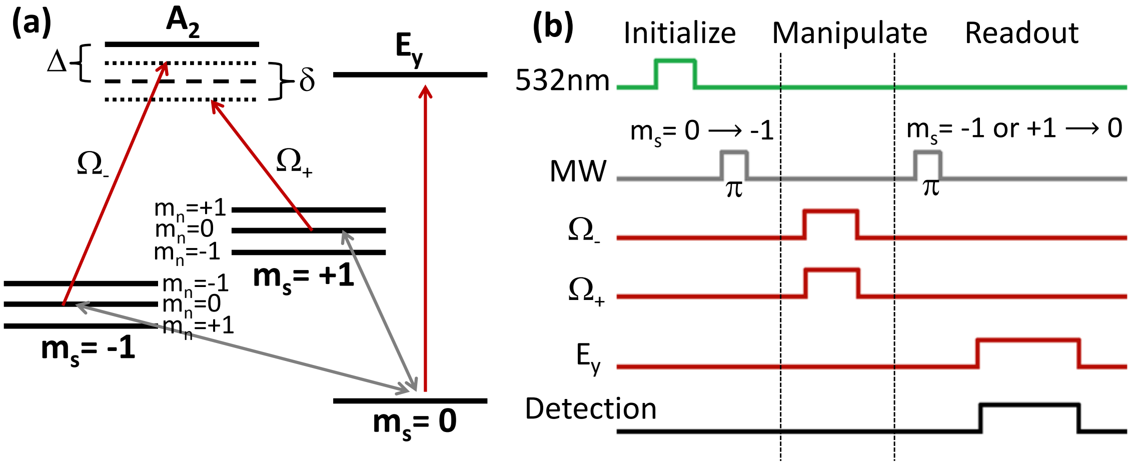

Figure 5.1. (a) Energy level diagram including the hyperfine splitting, optical and MW excitations, and the relevant excited states. (b) Pulse sequence used for two-photon ODROs.

state. Second, an additional optical field resonantly drives the transition between $m_s = 0$ and the E_y excited state while, as usual, the phonon sideband fluorescence is detected.

The results are shown in Fig. 5.2a where the resulting populations in both $m_s = -1$ and $m_s = +1$ are measured. As the widths of the optical pulses in the manipulation step are increased, the electron spin population oscillates between $m_s = -1$ and $m_s = +1$ just as if this transition were being driven directly. These Rabi oscillations feature a decay time of 1.3 μs, much longer than the excited state lifetime of 11.5 ns. We will discuss the various decay mechanisms in detail later.

For this data, an overall dipole detuning (Δ) of -1.5 GHz (blue detuned) was used. We perform the same measurement for various dipole detunings and optical field powers and plot the results in Fig. 5.2b. The oscillation period is seen to be proportional to | Δ |,

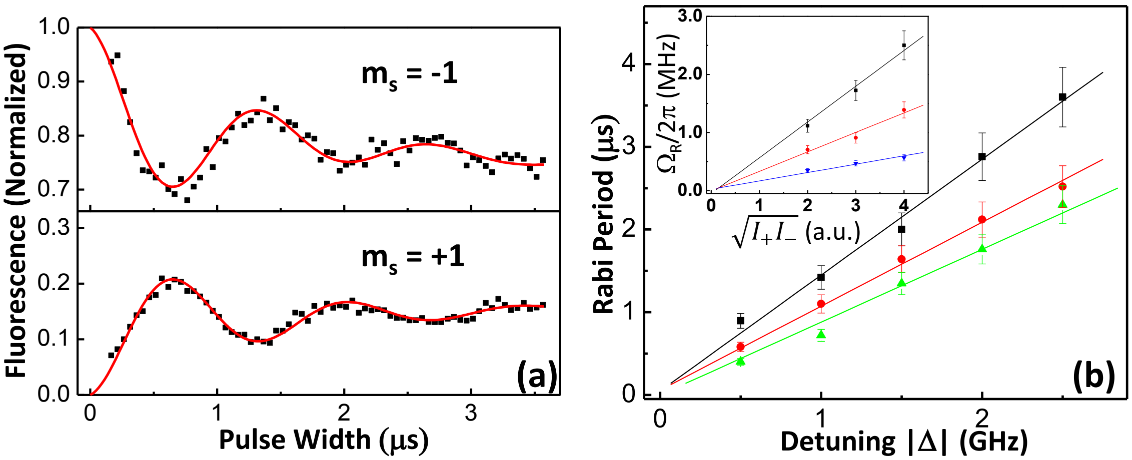

Figure 5.2 (a) ODROs of an electron spin. The fluorescence measures the population in the $m_s = \pm 1$ states. The solid lines are a numerical fit to a damped oscillations with an added slope due to optical pumping. (b) Period of the ODROs as a function of detuning for three different optical intensities. Inset: effective Rabi frequency as a function of the intensity for three different detunings.

while the effective Rabi frequency is proportional to $\sqrt{I_+ I_-}$, where I_+ and I_- are the peak intensities of the two optical pulses. These are just the relations we would expect from (5.3).

5.2.3. Nuclear Spin Dependence of the Two-Photon ODROs

One of the most fruitful features of MW based spin control in the NV center has been the ability to couple the electronic spin state with nearby nuclear spin states [51], [56], [92], [93]. If optical control is to be a genuine alternative to MW control, we need it to be capable of displaying the same nuclear spin dependence.

It turns out that the Rabi oscillations shown in Fig. 5.2 do in fact depend on the ^{14}N spin state. For the data shown there, the detuning between the two optical fields, δ, was set so that they would be on Raman resonance for the $m_n = 0$ hyperfine states. Fig. 5.3 includes plots of the same measurement for two additional detunings, one with the fields on Raman resonance for the $m_n = +1$ hyperfine states and the other with the Raman detuning set in between hyperfine states. Rabi oscillations are observed only when the m_n-dependent Raman resonance condition is satisfied and disappear away from that resonance. This indicates that only one hyperfine state is being driven at a time. As we would expect, as long as the two-photon ODRO Rabi frequency, Ω_R, is small compared with the hyperfine splitting, these ODROs are nuclear spin selective.

The nuclear spin orientation on a given experimental run is random and so these measurements sum over all three orientations. The population will therefore oscillate only 1/3 of the time, meaning that, for ODROs with perfect fidelity, the observed oscillations

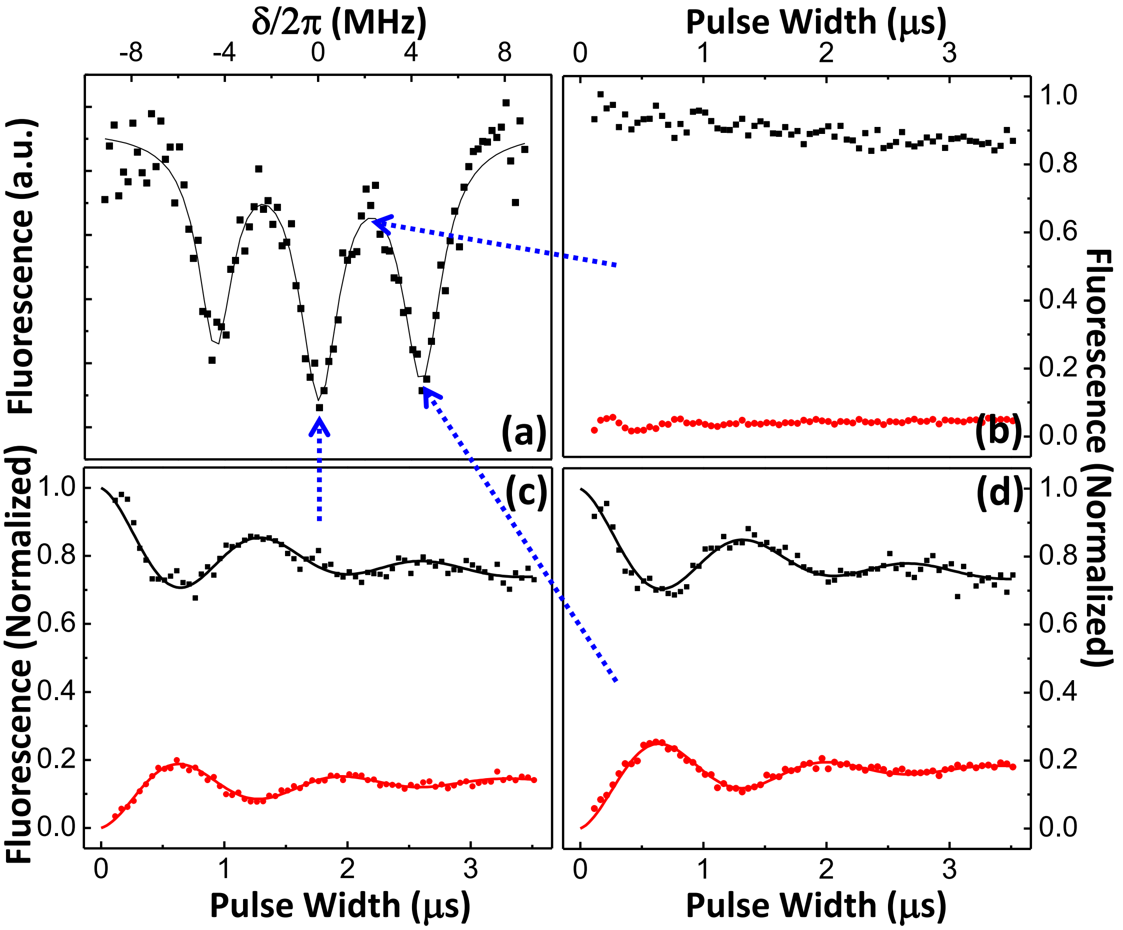

Figure 5.3. Nuclear spin selective ODROs with detunings indicated in the CPT trace shown in (a). (b)-(d) The populations in the m_s = -1 (top traces) and m_s = +1 (bottom traces) states as a function of optical pulse width. Solid lines in (c) and (d) are numerical fits to damped oscillations.

in fluorescence will fluctuate by a maximum of 1/3. The other two hyperfine states provide a steady background.

It is worth noting that the data shown in Fig. 5.3b, where ODROs are not driven, also gives a nice measurement of excitation into the A_2 state. Any such excitation would lead to optical pumping, as A_2 can decay into any of the ground states (recall that decay into $m_s = 0$ is small though). This pumping would increase with increasing optical pulse lengths. The slow decay rate that we observe indicates that this effect plays only a minor role in the decay of the Rabi oscillations.

5.2.4. Ramsey Fringes Measured using Two-Photon ODROs

We now use our optical control to perform a Ramsey fringe measurement. This type of measurement is sensitive to the undriven spin dynamics of the system. The procedure is relatively simple. A superposition of two states is created using a π/2-pulse and then allowed to evolve freely for a time τ during which one state can pick up a phase relative to the other. After this delay, a second π/2-rotation converts this phase difference into a population difference which can then be measured.

To make the signal more apparent the control field is detuned from exact resonance (i.e. in this case the two optical fields are slightly detuned from Raman resonance, $\delta \neq 0$). With respect to this field, then, the relative phase during the free evolution time will oscillate at a frequency given by the detuning. This shows up as a population oscillation after the second π/2-rotation is performed.

The spin environment of the NV center causes dephasing. Nearby atoms with nonzero nuclear spin, typically ^{13}C, together produce a net magnetic field. The NV electron spin can precess around this weak bath field. This results in an additional phase difference being picked up during the free evolution part of the Ramsey measurement. Since the bath field exhibits random fluctuations, this phase will be different for each measurement causing the Ramsey signal, which sums over many measurements, to decay. The rate of this decay thus provides a good measure of the dephasing rate.

For this measurement we use the same sequence we used to measure ODROs; the spin state is initialized into $m_s = -1$ and the final population in $m_s = +1$ is detected. In between we now implement the Ramsey pulse sequence where the π/2-pulses are optically driven and are calibrated from ODRO measurements. The two optical fields are given a detuning from Raman resonance, δ, of 1.4 MHz for the $m_n = 0$ hyperfine states. For this measurement we used a smaller dipole detuning ($\Delta = 1$ GHz) and higher optical powers so that the transition can still be driven given this value of δ. The optical spin control will also no longer be completely nuclear spin selective. (The optical pulse may not produce a true π/2-rotation for all three hyperfine states. However, while the Ramsey measurement is most efficient when π/2-rotations are used, it will still work with non-π/2-rotations so long as at least some rotation takes place. The phase of the resulting oscillations will be affected by this.)

The resulting Ramsey fringes are shown in Fig. 5.4b where a nuclear-spin-selective MW π-pulse was used in the initialization step to populate only the $m_n = 0$ hyperfine state of the $m_s = 0$ level. Thus only this hyperfine state contributes to the Ramsey signal, and we observe oscillations at the frequency of the Raman detuning for this hyperfine state (1.4 MHz). In Figs. 5.4c and 5.4d we initialize into the $m_n = -1$ and $+1$ states respectively. The oscillations in these measurements match the Raman detunings for these hyperfine states (2.2 MHz + 1.4 MHz and 2.2 MHz – 1.4 MHz respectively). For Fig. 5.4e a non-nuclear-spin-selective MW π-pulse initialized all three hyperfine states. The Ramsey fringes now display a more complicated pattern with each hyperfine state contributing to the signal.

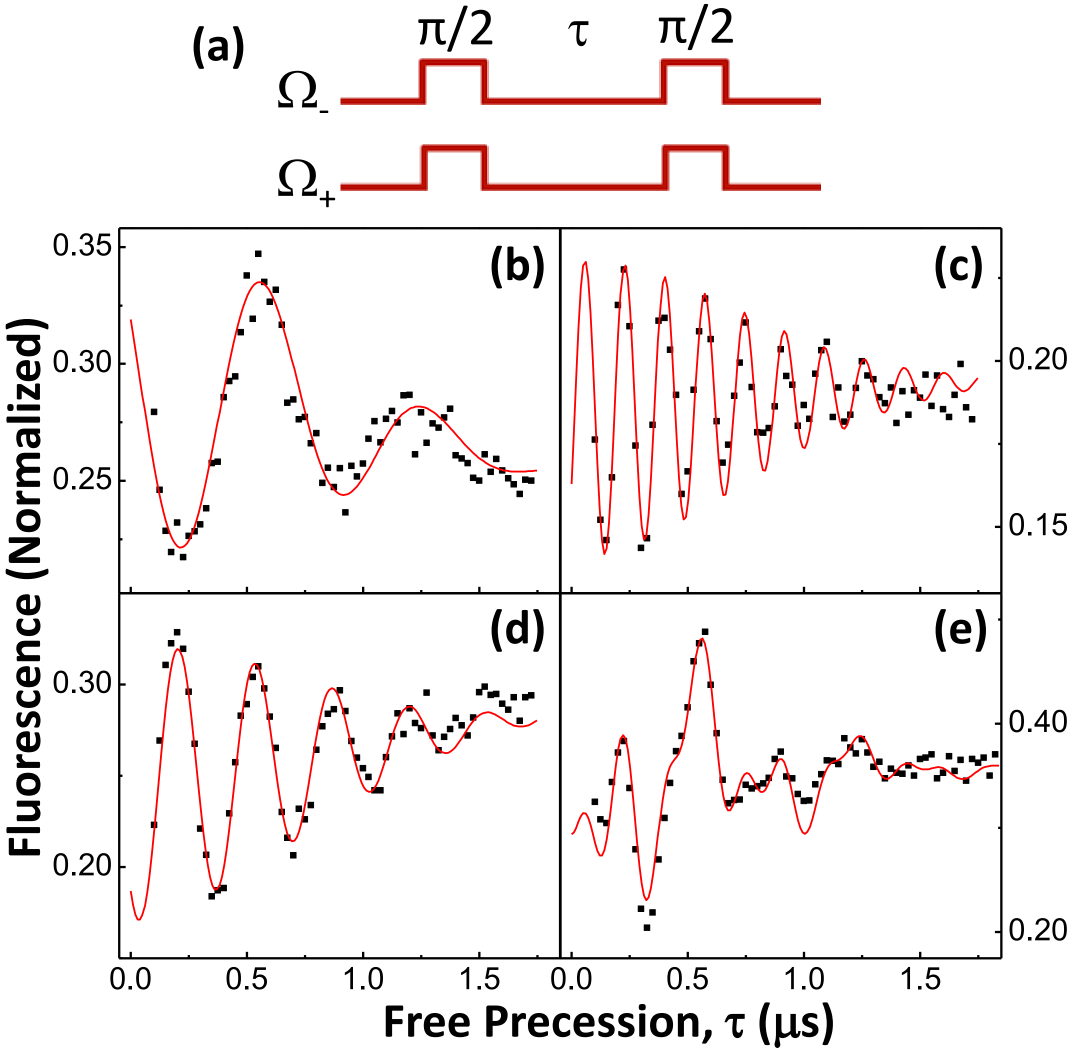

Figure 5.4. Ramsey fringe measurement using ODROs. (a) Pulse sequence for the spin manipulation step. (b)-(e) Free induction decays of an electron spin with $\Omega_R/2\pi = 2.5$ MHz and $\Delta = -1$ GHz. For (b), (c), and (d), nuclear-spin-selective MW π-pulses were used to prepare the electron spin in the $m_s = -1$ and $m_n = 0, -1$, and $+1$ hyperfine states respectively so that only these hyperfine states contribute to the signal. For (e), the electron spin was prepared in the $m_s = -1$ state with random nuclear spin orientation. Solid lines are numerical fits as discussed in the main text.

We numerically fit the data in Fig. 5.4b-d with a curve given by $e^{-(\frac{\tau}{T_2^*})^2}\cos(2\pi\delta_n)$, where δ_n is the Raman detuning for the relevant hyperfine state. The phase of the oscillation was also adjusted to match the data. The fits for each hyperfine case are added together and plotted, with an overall scaling factor, onto the data in Fig. 5.4e. These fits indicate a dephasing time, T_2^*, of approximately 1 μs. This is in agreement with other Ramsey fringe measurements performed on this same NV center using MW driven, rather than optically driven, π/2-rotations. We have illustrated the viability of using this two-photon ODRO spin control as a substitute for MW spin control.

5.3. Stimulated Raman Adiabatic Passage

A second method of optical spin control is STIRAP. Again we begin with a theoretical description of the process followed by the experimental realization. We designed STIRAP experiments that also include the two-photon ODROs that were just described. This will be helpful as we compare these two control techniques.

5.3.1. Stimulated Raman Adiabatic Passage: Theory

Recall the dark state discussed in the previous chapter with respect to CPT.

$$|\mathrm{d}\rangle = \frac{1}{\sqrt{{\Omega_+}^2+{\Omega_-}^2}}\begin{pmatrix}\Omega_+\\ -\Omega_-\\ 0\end{pmatrix} \tag{5.4}$$

This is an eigenstate of H, when Raman resonance is met ((5.1) with $\delta = 0$), with an eigenvalue of 0. This dark state is decoupled from the excited state and has a form that depends on the ratio of the two optical field strengths. By varying this ratio, the dark state can be tuned. If this is done slowly enough the spin state will adiabatically follow the dark state. By initializing the system into the dark state and then adjusting the amplitudes of the two optical fields adiabatically, population can be transferred between the two lower levels of the Λ-configuration with the system remaining in the dark state the entire time. In order to satisfy the adiabatic requirement, the rate of the transfer needs to be slow compared with Ω_R [94]. We therefore expect STIRAP to be slower than the ODROs.

5.3.2. Stimulated Raman Adiabatic Passage: Experiments

To perform and measure STIRAP we use a similar pulse sequence to that used for ODROs. One again the electron spin is initialized into the $m_s = -1$ ground state; and at the end, the population in the $m_s = +1$ state is measured. Two Raman resonant, dipole detuned optical pulses are used in the manipulation step as before, but now their temporal line shapes are more complex and the time delay between the two pulses is varied. The shapes of the two pulses are shown in Fig. 5.5a. The trailing edge of the Ω_+ pulse and the rising edge of the Ω_- pulse are characterized by a time, t_{rise}. The rising edge of the Ω_+ pulse and the trailing edge of the Ω_- pulse are sharp and are separated by a time, T.

For different values of T, different parts of the two pulses overlap and different amounts of population are transferred from $m_s = -1$ to $m_s = +1$. There are two different regimes. When the sloping portions of the two pulses overlap, STIRAP can take place. The system begins in state $m_s = -1$, so when Ω_+turns on it is already in the dark state. As Ω_+slowly ramps down and Ω_- slowly ramps up, the dark state rotates and is ultimately left in $m_s = +1$. When the peak amplitudes overlap (and the sloping edges do not) the experiment is the same as that used to measure ODROs.

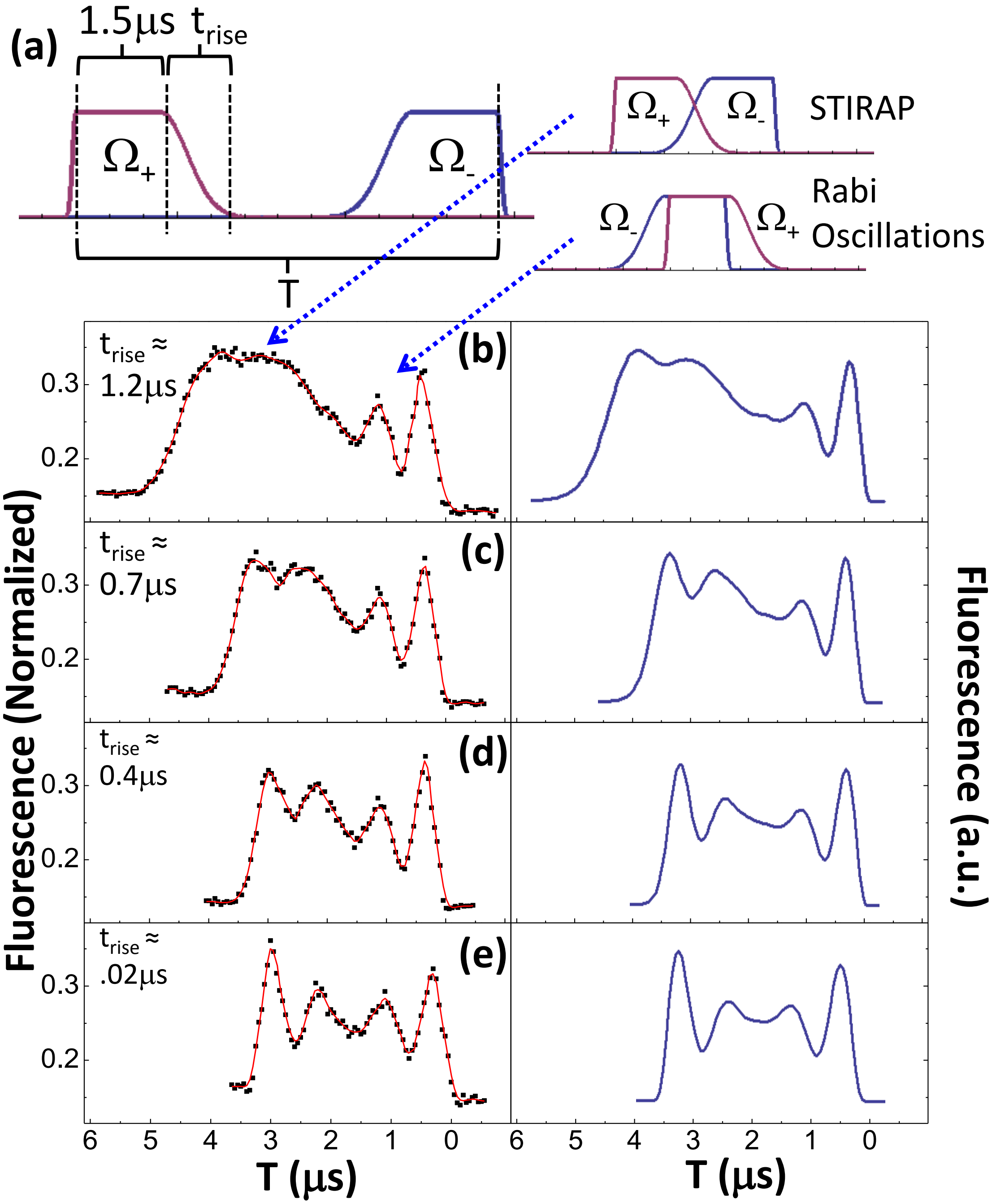

Figure 5.5. STIRAP and ODROs. (a) The temporal line shapes of the two Raman resonant optical pulses used during the spin manipulation step. The final population in state $m_s = +1$ *is measured as a function of delay, T, between the two pulses. The regimes where STIRAP and ODROs take place are indicated. (b)-(e) Left column: experimental results obtained with different* t_{rise}*, as shown in the figure. Solid lines are guides to the eye. Right column: theoretical calculations using the parameters of the experiments in the left column. These calculations are discussed in detail in the main text.*

Fig. 5.5b shows the measurement results. The first half of the plot represents population transfer via STIRAP. The smoothly increasing edge corresponds to an improving efficiency of the overlap. The second half corresponds to the two-photon ODROs. The backwards decay of these oscillations is because moving to the right in this part of the plot represents a decreasing optical pulse width. The dipole detuning of the optical fields means that when the pulses do not overlap (the beginning and end of the plot) there should be no excitation or transfer, although the slight difference in height between these two parts of the plot indicates that a very small degree of pumping does take place. A larger dipole detuning would minimize this even further.

STIRAP only happens when the dark state is evolved adiabatically. To demonstrate this, we carry out the same measurement for different values of t_{rise}. This is shown in Fig. 5.5b-e. As t_{rise} is decreased we can see the adiabatic condition breaking down and the STIRAP being replaced with ODROs. This confirms that STIRAP can only occur on a time scale longer than the Rabi period.

Plotted next to the experimental data in Fig. 5.5b-e are the results of a theoretical simulation of this experiment. There is good agreement between the data and the model. We now describe this model in detail and then use it to look at the effects of different decoherence mechanisms.

5.4. Theoretical Model

To analyze the results of our ODRO and STIRAP experiments, especially the effects of various broadening mechanisms, we perform a simulation using the model three-level system that we have been describing so far [27]. We include only one excited state level. Other excited states exist which couple to the ground state, but the state we are concerned with, A_2, is the highest in energy. Since we use optical fields that are blue-detuned, and the nearest excited state, A_1, is about 3 GHz lower in energy, contributions from this and other states will be negligible.

We numerically solve the Lindblad form master equation

$$\frac{\partial \rho}{\partial t} = -i[H,\rho] + \mathrm{D}(\rho) \tag{5.5}$$

with H defined in (5.1) and with

$$\mathrm{D}(\rho) = \begin{pmatrix} \Gamma\rho_{ee} & -\gamma_s\rho_{-+} & -\gamma\rho_{-e} \\ -\gamma_s\rho_{+-} & \Gamma\rho_{ee} & -\gamma\rho_{+e} \\ -\gamma\rho_{e-} & -\gamma\rho_{e+} & -2\Gamma\rho_{ee} \end{pmatrix}. \tag{5.6}$$

where Γ is the excited state population decay rate, γ is the optical dipole coherence decay rate, and γ_s is the spin coherence decay rate. We set $\Gamma/2\pi = \gamma/2\pi = 7$ MHz, and $\gamma_s/2\pi = 1/(2\pi * T_2) = 0.8$ kHz. This model ignores decay out of the Λ-system which is a reasonable approximation [68].

5.4.1. Model of Two-Photon ODROs

To model the Rabi oscillations shown in Fig. 5.2 we set $\Delta/2\pi = -1.5$ GHz, $\delta/2\pi = 0$, and $\Omega_+/2\pi = \Omega_-/2\pi = 46$ MHz (as inferred from Ω_R). In Fig. 5.6a the final population in level $m_s = +1$, (ρ_{++}), is plotted as a function of pulse width. The small amount of decay is mostly due to optical pumping from direct excitation into A_2. In the experiment, the two hyperfine states for which the optical fields are not on Raman resonance will contribute to the background through pumping but not to the Rabi oscillation signal itself.

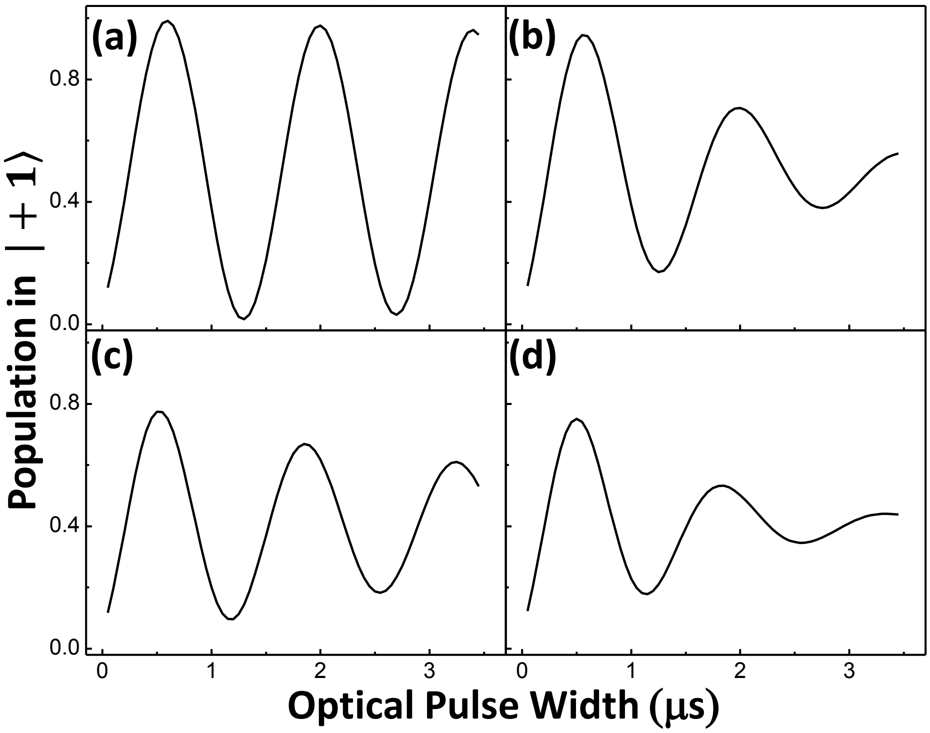

Figure 5.6. Simulation of the two-photon ODROs. (a) Δ held constant and δ = 0. (b) Spectral diffusion is included. Sum over Δ's with δ = 0. (c) Dephasing is included. Sum over δ's with Δ held constant. (d) Both spectral diffusion and dephasing are included. Sum over Δ's and δ's.

Each repetition of the experiment begins with off-resonant excitation which can cause spectral diffusion. This acts as an inhomogeneous broadening of the A_2 transition. We model this by summing the results of our simulation over a range of Δ's, weighting them by a Gaussian with a FWHM$/2\pi$ = 500 MHz as estimated from PLE measurements. This produces the plot shown in Fig. 5.6b. Since the effective Rabi frequency depends on Δ, the sum is over a range of Rabi frequencies resulting in an increase of the measured decay. If the spectral fluctuations of the NV optical transition were instead included as a part of the intrinsic decoherence rate, the calculation would predict effects of optical pumping that are much greater than those we see in the experiment.

To describe the decay rate observed in our experiments, we also need to add the effects of dephasing between the $m_s = +1$ and $m_s = -1$ ground state levels. From our measurement of Ramsey fringes we determined a dephasing time of $T_2^* = 1$ μs. To model this, we sum over a range of δ's weighted by a Gaussian with a $\mathrm{FWHM}/2\pi = 1$ MHz. Fig. 5.6c shows the results where Δ is held constant and these dephasing effects are included. Cases with a non-zero δ (both positive and negative) exhibit smaller oscillation amplitudes and increased Rabi frequencies. This means that the net effect of including dephasing is to produce oscillations with a smaller amplitude, a slightly shifted Rabi frequency, and an increased decay rate. Fig. 5.6d shows the results with both spectral diffusion and dephasing effects included. We now have a decay rate that is similar to that observed in the experiment.

5.4.2. Model of the STIRAP Experiment

The STIRAP/Rabi oscillation experiments were modeled in the same way. Now we use $\Delta/2\pi = -0.9$ GHz and $\Omega_{\pm}/2\pi = 48$ MHz to match the experimental parameters. Given these parameters, optical pumping is expected to be a larger effect than in the Rabi oscillation case. Additionally, the process may no longer be completely nuclear spin dependent; however using a smaller Ω_R should recover this dependence. The scale of the simulated plots was adjusted to match that of the experiments so that the shapes could be easily compared.

As with Fig. 5.6, Fig. 5.7 shows the results of the simulation for (a) Δ constant with $\delta = 0$, (b) a sum over Δ's, (c) a sum over δ's, and (d) a sum over both Δ's and δ's. We can see from these simulations that including spectral diffusion has a relatively large effect on the Rabi oscillations, but a relatively small effect on the STIRAP. This is to be expected since the STIRAP process is relatively insensitive to Δ. The dephasing, on the other hand, has a smaller effect on the Rabi oscillations; and it reduces the overall efficiency of the STIRAP without significantly changing the adiabaticity.

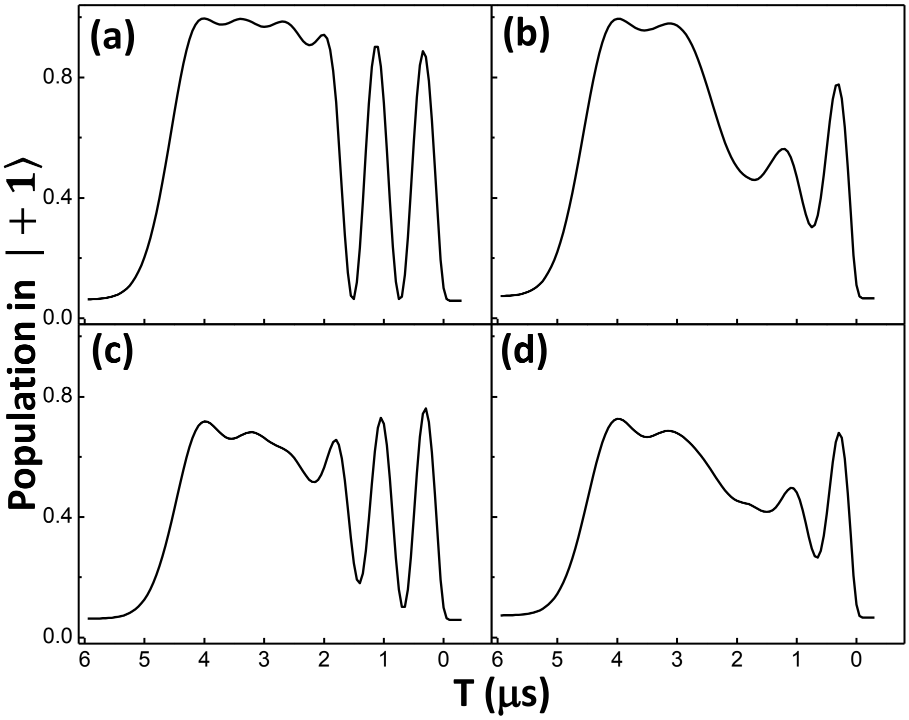

Figure 5.7. Simulation of the STIRAP/ODRO measurement. (a) Δ held constant and δ = 0. (b) Spectral diffusion is included. Sum over Δ's with δ = 0. (c) Dephasing is included. Sum over δ's with Δ held constant. (d) Both spectral diffusion and dephasing are included. Sum over Δ's and δ's.

Overall this shows us that ODROs are faster but are limited by both spectral diffusion and spin dephasing, while STIRAP is slower and still sensitive to dephasing but is much more robust against spectral diffusion. These limits can in principle be pushed back. Dephasing can be significantly reduced by using an isotopically pure diamond [95], a dynamical decoupling procedure [96], or the MW dressed states described in the next chapter. It has recently been shown that spectral diffusion can be decreased by replacing the green, off-resonant initialization pulse with a weaker resonant excitation of the NV^0 charge state [97]. This would need to be combined with NV^- resonant optical initialization [69]. Replacing the green excitation would have the added benefit of allowing one to use smaller dipole detunings without risking direct excitation and the consequent optical pumping. This and/or increasing the overall optical power would make both ODRO and STIRAP controls faster.

5.5. Subwavelength Resolution using Optical Control

Finally, we look at a potential application of all-optical control. Optical manipulation and detection make possible spectral resolution of NV centers. They also offer a vast improvement over the spatial resolution given by MW control. However, the optical spatial resolution is still diffraction limited to approximately the wavelength of the optical field. This may not be enough for applications that require multiple NV centers to be closely spaced. The physics of the dark state, which underlay our STIRAP control method, suggests the prospect of subwavelength control. We present a preliminary experimental investigation into this possibility.

5.5.1. Subwavelength Resolution Techniques

There are various strategies for improving on the diffraction limit, typically by exploiting a nonlinearity in the response of an atomic system to excitation; and several of these have been demonstrated in the NV center [98]. Stimulated emission depletion (STED) microscopy works by saturating the stimulated emission process in a spatially dependent way. An emitter in the region that is not saturated will fluoresce via spontaneous emission whereas a saturated emitter will not. This process works well in the NV center thanks to its relatively long excited state lifetime [99]. A similar mechanism is used in ground state depletion (GSD) microscopy [100]. Both STED and GSD require optical fields with very high power. A third technique has been demonstrated with NV centers, that does not need as much power. Referred to as Spin-RESOLFT (Reversible Saturable Optical Fluorescence Transitions), this method uses a combination of MW spin control and spatially dependent optical initialization [101].

All of these methods for achieving subwavelength resolution work by putting the emitter into a state, in a spatially dependent way, where it will not emit under excitation. This is reminiscent of the dark state which we have been discussing. In fact, a super resolution method has been proposed recently [102], [103] which makes use of the potential non-linear spatial sensitivity of this dark state.

As described above, the form of the dark state depends on the ratio of the two Raman resonant optical field strengths. By carefully choosing the spatial profiles of these fields, the response of the dark state can have a subwavelength spatial dependence. Specifically we want the amplitude of one field to go through a minimum while the amplitude of the other field goes through a maximum. If the system is then prepared adiabatically into the dark state it will share in this high spatial resolution as will any subsequent optical spin measurements.

5.5.2. Subwavelength Resolution Experiment

We test this technique using a measurement similar to that featured in the ODRO and STIRAP experiments; but now we give a different spatial profile to one of the optical fields in the manipulation step. The focal spot for all the optical fields is then scanned spatially. The resulting spin state should consequently exhibit subwavelength spatial dependence.

One of the Raman resonant optical fields is left with the normal Gaussian intensity profile. We put the other field into a doughnut mode by passing the laser beam through a vortex phase plate (RPC Photonics, VPP-1a) before combining it with the other lasers. This produces a focal spot on the diamond with an intensity minimum in the center. To confirm the beam profiles we perform a PLE measurement by tuning the red laser onto resonance and then scanning the position of the focal spot. For simplicity, we limit our measurements to one dimension in the experiments described here. The emitted fluorescence as a function of spot position for both the Gaussian and the doughnut beams is shown in Fig. 5.8. As desired, in the center one is minimized while the other is maximized.

After spin initialization into $m_s = +1$, the two optical pulses are applied in such a way as to adiabatically prepare the system into a dark state defined by the ratio of the powers of these fields. First the field coupling to $m_s = -1$ turns on (doughnut beam) so the

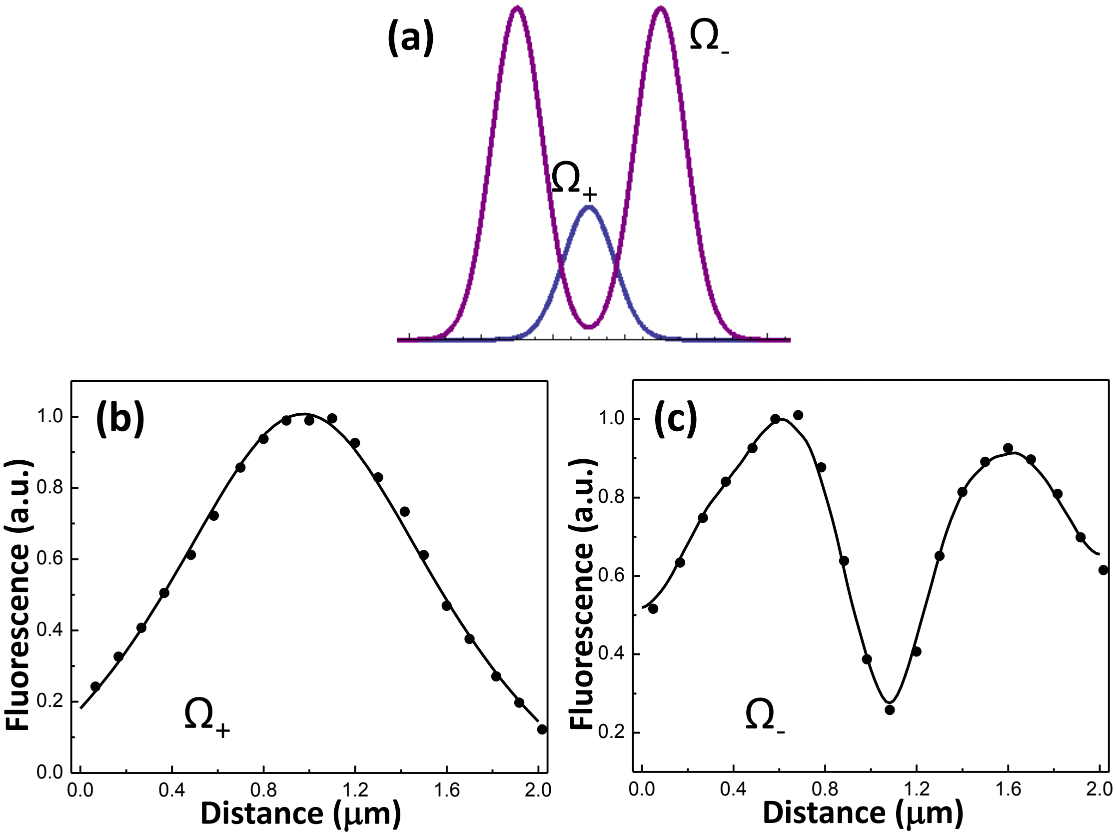

Figure 5.8. PLE measurement of the two beam profiles used for the subwavelength spatial resolution experiment. Only one dimension is shown. (a) Desired pulse shapes. (b) Fluorescence as the Gaussian beam is scanned over the NV center. (c) Fluorescence as the doughnut beam is scanned over the NV center. The doughnut beam is given an overall higher power in the experiment.

system begins in the dark state. Next the field coupling to $m_s = +1$ ramps up, tuning the dark state. Finally the two beams turn off simultaneously leaving the system in the new dark state. Away from the center, the doughnut field has high power giving a dark state that is close to the initialization state. In the center, the Gaussian field has high power resulting in a dark state that represents a spin transfer.

We plot the amount of spin transfer as a function of beam position, where both beams were scanned together across the NV center, in Fig. 5.9a (as well as the population

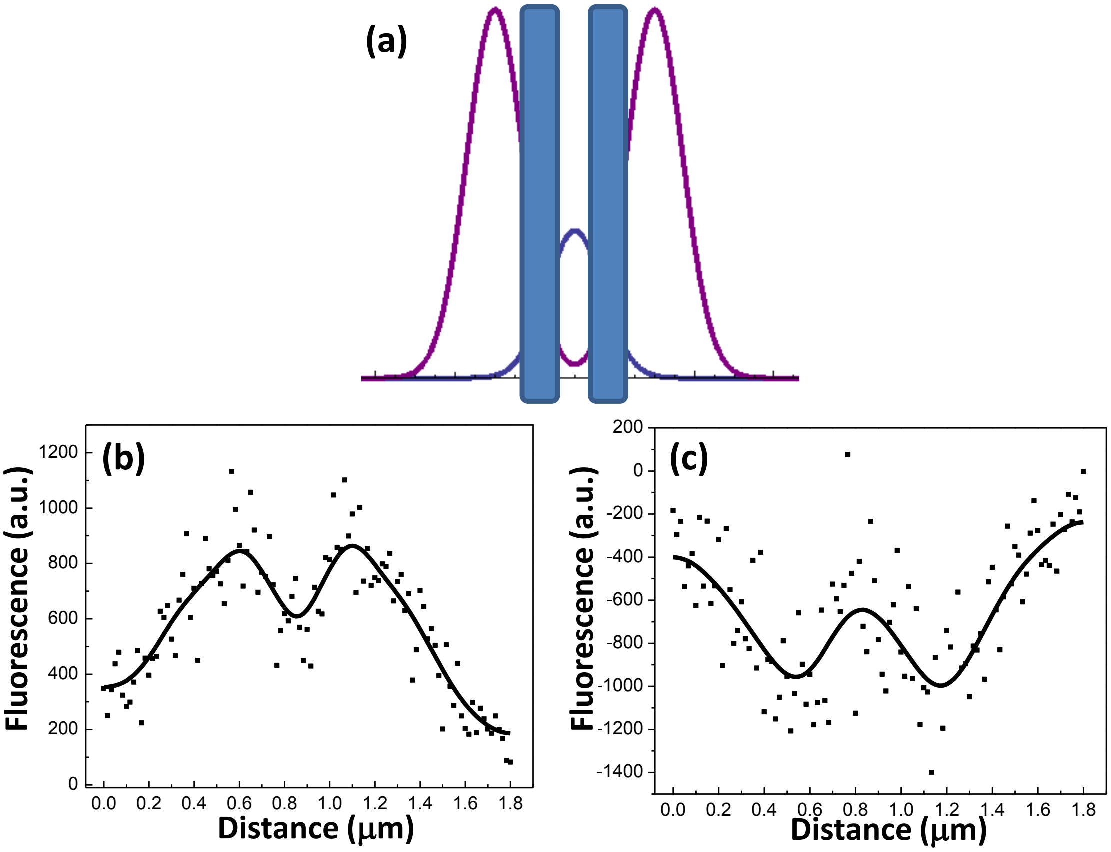

Figure 5.9. Spatially dependent STIRAP. (a) Spatial profile of the two optical fields. The shaded regions indicate where the greatest spin transfer occurs. (b) Final population in $m_s = -1$ indicating a spin transfer. (c) Final population in $m_s = +1$. For both (b) and (c) the same measurement was performed away from Raman resonance and the results were subtracted from the on resonance data in order to remove the effects of optical pumping. The solid lines are guides to the eye.

remaining in the initial state in Fig. 5.9b). We subtracted off the effects of optical pumping which were determined by carrying out the same measurement with the fields away from Raman resonance.

We successfully measure a spatially dependent spin transfer. However we observe an unexpected suppression of the spin transfer in the center, just where we expected the transfer to be the greatest. This likely means that, given the experimental parameters that we used, the doughnut beam was too weak in the center to meet the adiabatic condition. However simply increasing the power in the center of the doughnut would decrease the resolution capability of this measurement. Optical pumping was a challenge in this experiment, and increasing the length of the optical pulses so as to regain adiabaticity in the center would make this even worse.

The feature we observe does appear to be close to subwavelength, and so this initial experiment demonstrates the viability of this super resolution technique. Future experiments will require the right balance of power and duration. Techniques that reduce spectral diffusion would make this measurement possible with a smaller dipole detuning and less optical pumping. With higher optical Rabi frequencies, sharper spatial dependence should be easier to achieve.

5.6. Conclusion

We have demonstrated two-photon ODROs and STIRAP of single electron spins in the NV center. This confirms that with a modest dipole detuning, optical spin control can be realized that is not limited by the rapid radiative decay and large spectral diffusion that are associated with the underlying optical transitions. The ODROs were shown to give faster control, while the STIRAP control was less sensitive to spectral diffusion.

We also took the first steps in developing optical spin control as a feasible alternative to MW spin control by producing optically-driven, nuclear-spin-dependent electron spin flips as well as by using the optical control to perform a Ramsey fringe measurement of the spin dephasing rate.

Lastly we began investigations into using the optical control for subwavelength spatial resolution of the NV center via a spatially dependent adiabatic spin transfer.

CHAPTER VI

DECOHERENCE PROTECTED DRESSED SPIN STATES IN THE NV CENTER

This chapter contains some material that was co-authored with Hailin Wang and Thomas K. Baldwin in reference [72]. The experiments described here were performed by the author.

The decoherence of a quantum state due to uncontrolled interactions with its environment puts a fundamental limitation on applications of quantum control and quantum information. While completely isolating a quantum system is not possible, and not even desirable since coupling between multiple quantum systems is also of fundamental importance, decoherence effects must be minimized to manageable levels.

It is a particular weakness inherent in solid-state systems that they are not spatially isolated from their environment. An atom-like solid-state system is embedded within a larger structure of atoms. If the system is sensitive to magnetic fields, uncontrolled spins associated with these atoms will severely limit coherence. It has already been noted that one of the advantages of using diamond based impurity centers is that the atomic environment, a crystal lattice of mostly spin zero ^{12}C atoms, is very magnetically quiet. Furthermore the spin-lattice relaxation time for this system is on the order of seconds [95] meaning that impurity spins are the limiting factor. Combining this natural advantage with various decoherence reducing techniques has allowed experimentalists to demonstrate, in the NV center, some truly remarkable coherence times for a solid-state system.

In this chapter we develop one such technique which relies on the insensitivity of certain MW dressed electronic spin states to small fluctuations of an external magnetic field. The method we describe will be effective for certain applications where other decoherence reducing methods are difficult to implement. We begin by describing some different methods including the one we use. Next we look at dressed states and their response to magnetic fluctuations. CPT measurements allow us to probe these states. After that we give a more detailed theoretical account of CPT with special emphasis on broadening mechanisms. This allows us to use CPT measurements to compare the decoherence rates for bare and MW dressed spin states. We will see that using MW fields, with an easily achievable coupling rate, to dress a single electron spin can lead to a better than 50 times reduction in the linewidth of the spin transition, limited by transit-time broadening.

6.1. Strategies for Improving the Coherence Time of the NV Electronic Spin State

The most straightforward way to lengthen the coherence time of the NV center electronic spin state is to increase the purity of the diamond sample. Since it is the interaction with impurity spins that causes decoherence, fewer impurities equals less decoherence. ^{13}C has a natural abundance of 1.1%. Measurements in isotopically pure diamond with ^{13}C reduced to 0.3% indicate an increase in coherence time, T_2, from a couple hundred microseconds to 1.8 ms [95]. To measure this, spin-echo sequences must be used to get past spin dephasing. Presumably higher purity diamond would yield even better coherence properties. There are higher costs and technical challenges associated with producing such samples.

Another approach is to use coherent control of the spin state to average out decoherence processes. Dynamical decoupling procedures [104] involve a series of rapid spin flips which together cancel out the bath-induced spin dynamics. Various approaches such as the optimized Uhrig sequence or the periodic Carr-Purcell-Meibloom-Gill sequence have been successfully implemented in different systems such as trapped ions [105], quantum dots [106], and NV centers [96]. In the NV center these techniques have also been applied to the coupled electron-nuclear spin system [107] and have produced a coherence time for the nuclear spin greater than 1 s [108].

Dynamical decoupling represents a time domain approach, and the electron spin is decoupled from the bath at specific times. The dynamics of the electron spin, however, are still influenced by the fluctuating bath field. In addition, the decoupling pulse sequence can often be in conflict with other desired quantum operations.

It has been suggested recently that the NV electron spin can be decoupled from the bath at all times with a spectral domain approach, in which a coherent coupling between the spin and continuous fields leads to the formation of dressed spin states [109]-[111]. The energy levels of the dressed spin states can become immune to fluctuating magnetic fields when the coherent coupling rate far exceeds the relevant amplitude and rate of these bath-induced fluctuations. In essence, the energy gap between the dressed spin states protects the electron spin from decoherence induced by the spin bath. This dressed state approach for protecting a spin from decoherence is often referred to as continuous dynamical decoupling and has been applied, using MW fields, to trapped ions

[112]. Work has begun towards applying it in NV centers using MW based measurements [113]-[115].

Since this approach works in the spectral domain rather than the time domain, spin echo and spin echo like procedures are no longer necessary for cancelling out dephasing. Dressing a spin state fundamentally changes how it responds to magnetic fluctuations and is likely more compatible, than for instance dynamical decoupling, with applications such as building a coupled spin-nanomechanical system or spin-based cavity QED.

We follow this method, using continuous MW fields to dress the NV center ground spin states. We then couple the dressed spin states to optical transitions and employ CPT via these optical transitions to probe the energy level structure, optically-induced spin transitions, and spin decoherence rates of the dressed spin states.

6.2. Dressed Spin States

We will start by describing the dressed states that feature in this decoherence reducing method, and we will see how it is that they are insensitive to small magnetic field fluctuations. We then perform a CPT measurement that allows us to observe these dressed states.

6.2.1. MW Dressed Spin States in the NV Center

The NV center spin ground-state triplet forms a V-configuration. To create the dressed spin states, we coupled two MW fields to the two ground state transitions with equal Rabi frequency, Ω_m. The Hamiltonian of this combined spin and MW-field system in the rotating frame is given by

$$H = \hbar \begin{pmatrix} 0 & \frac{\Omega_m}{2} & \frac{\Omega_m}{2} \\ \frac{\Omega_m}{2} & \delta_+ & 0 \\ \frac{\Omega_m}{2} & 0 & \delta_- \end{pmatrix}, \tag{6.1}$$

where δ_+ and δ_- are the detunings for each MW field (in the absence of the spin bath B-field). With $\delta_+ = \delta_-$ (Raman resonance), one of the eigenstates of the time-independent Hamiltonian is a dark state,

$$|d\rangle = \frac{1}{\sqrt{2}}(|+\rangle - |-\rangle), \tag{6.2a}$$

which is decoupled from the MW fields. The orthogonal bright state

$$|b\rangle = \frac{1}{\sqrt{2}}(|+\rangle + |-\rangle) \tag{6.2b}$$

couples to the *m_s = 0* state ($|0\rangle$) through the MW fields. When $\delta_+ = \delta_- = 0$ (Raman resonance and zero dipole detuning), the other two eigenstates are given by

$$|l\rangle = \frac{1}{\sqrt{2}}(|b\rangle - |0\rangle) \tag{6.2c}$$

$$|u\rangle = \frac{1}{\sqrt{2}}(|b\rangle + |0\rangle). \tag{6.2d}$$

States $|l\rangle$, $|u\rangle$, and $|d\rangle$ are the semiclassical dressed states. The corresponding eigen energies are $E_l = -\hbar\Omega_m/\sqrt{2}$, $E_u = \hbar\Omega_m/\sqrt{2}$, and $E_d = 0$ (see Fig. 6.1).

6.2.2. Insensitivity of the Dressed States to Magnetic Fluctuations

So far we have included the effects of the external, static magnetic field which sets the Zeeman splitting, ω_B, between the levels *m_s = ±1* ($|\pm\rangle$). The energies of these

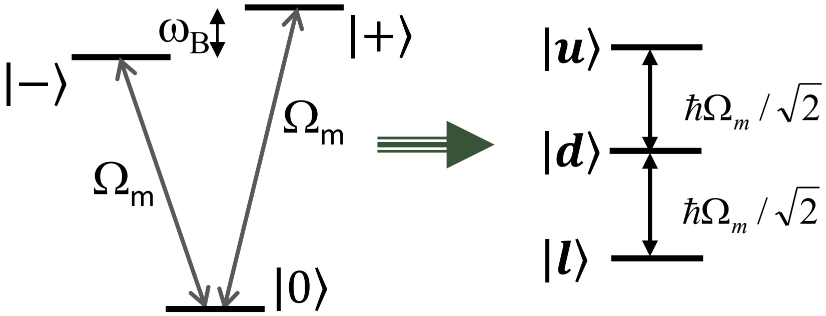

Figure 6.1. Two resonant MW fields with equal Rabi frequency, Ω_m, leads to the formation of three dressed states.

states are also dependent on the bath-induced magnetic field

$$H_B = g_s\mu_B B_N S_z \tag{6.3}$$

where B_N is the fluctuating magnetic field of the bath, g_s, is the effective g-factor for the electron spin, and μ_B is the Bohr magneton. This shifts these states by an additional amount $\pm\delta_N$, where $\delta_N = g_s\mu_B B_N$. The total Hamiltonian including these effects (where from here on we assume $\delta_+ = \delta_- = 0$) is given by

$$H = \hbar\begin{pmatrix} 0 & \frac{\Omega_m}{2} & \frac{\Omega_m}{2} \\ \frac{\Omega_m}{2} & \delta_N & 0 \\ \frac{\Omega_m}{2} & 0 & -\delta_N \end{pmatrix}. \tag{6.4}$$

The energies of the dressed states (now the eigenstates of this Hamiltonian) are now $E_l = -\hbar\sqrt{\frac{\Omega_m^2}{2} + \delta_N^2}$ and $E_u = \hbar\sqrt{\frac{\Omega_m^2}{2} + \delta_N^2}$ with $E_d = 0$ unchanged (see Fig. 6.2a). We can see that for $\Omega_m \gg |\delta_N|$, the dressed state energy levels become nearly independent of δ_N. This is illustrated in Fig. 6.2b.

This insensitivity to magnetic fluctuations is also apparent if we rewrite the Hamiltonian in (6.4) in the basis of the original dressed states, which were defined for

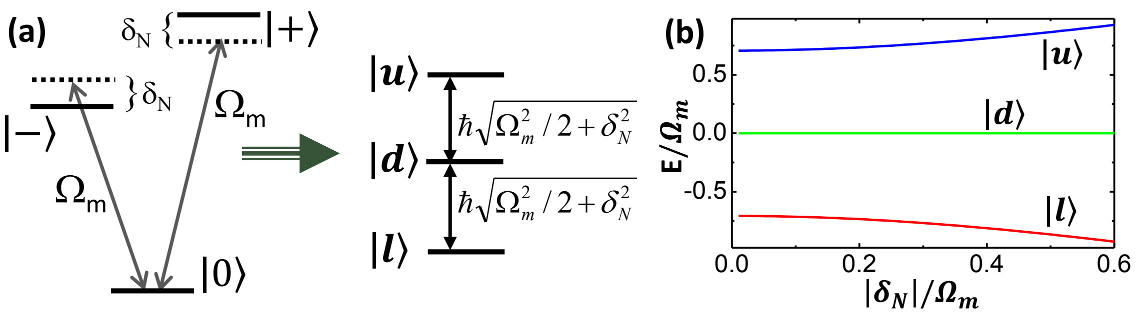

Figure 6.2. (a) The energies of the dressed spin states with the effects of a bath-induced Zeeman shift, $\pm\delta_N$, included. (b) The energies of the dressed spin states as a function of δ_N. For $\Omega_m \gg |\delta_N|$, the curves are relatively flat, indicating an insensitivity to changes in δ_N.

$\delta_N = 0$. In this basis we have

$$H = \hbar\begin{pmatrix} 0 & \frac{\delta_N}{\sqrt{2}} & \frac{\delta_N}{\sqrt{2}} \\ \frac{\delta_N}{\sqrt{2}} & -\frac{\Omega_m}{\sqrt{2}} & 0 \\ \frac{\delta_N}{\sqrt{2}} & 0 & \frac{\Omega_m}{\sqrt{2}} \end{pmatrix}. \tag{6.4}$$

Now the fluctuating Zeeman shifts appear only as off-diagonal matrix elements. From this perspective, the magnetic fluctuations of the bath cannot change the energy of the dressed states directly, but rather can mix or induce transitions between dressed states. However, as long as the amplitude and rate of the bath-induced fluctuations are small compared with the energy gap between the dressed states, the bath-induced mixings or transitions are negligible.

6.2.3. CPT Measurement of the Dressed Spin States

The MW dressed spin states can be probed through optical transitions. In the presence of the resonant MW fields, the electron wave function can be described, with probability amplitudes C_d, C_l, C_u for the dressed states and C_A for the A_2 state, as

$$|\psi\rangle = \left(\frac{C_u}{2}e^{-\frac{i\Omega_m t}{\sqrt{2}}} + \frac{C_l}{2}e^{\frac{i\Omega_m t}{\sqrt{2}}} + \frac{C_d}{\sqrt{2}}\right)e^{-\mathrm{i}\omega_B t}|+\rangle + \left(\frac{C_u}{2}e^{-\frac{i\Omega_m t}{\sqrt{2}}} + \frac{C_l}{2}e^{\frac{i\Omega_m t}{\sqrt{2}}} - \frac{C_d}{\sqrt{2}}\right)|-\rangle$$

$$+\left(\frac{C_u}{\sqrt{2}}e^{-\frac{i\Omega_m t}{\sqrt{2}}} - \frac{C_l}{\sqrt{2}}e^{\frac{i\Omega_m t}{\sqrt{2}}}\right)e^{i\nu t}\,|0\rangle + C_A|A_2\rangle\,, \tag{6.5}$$

where ν is the frequency of the MW field coupling to $|-\rangle$. Similar expressions can be derived for $\delta_N \neq 0$, with corresponding changes in the energy and wave function of the dressed states. Equation 6.5 shows that the states $|\pm\rangle$ each effectively split into three different levels due to coupling with the MW fields. In this case, σ_+ and σ_- polarized optical field will couple $|A_2\rangle$ to the m_s = *-1* part ($|u_-\rangle$, $|l_-\rangle$, and $|d_-\rangle$) and m_s = *+1* part ($|u_+\rangle$, $|l_+\rangle$, and $|d_+\rangle$) of the dressed spin states respectively as shown in Fig. 6.3. It is important to remember that these six states are not all independent. The dressed spin states are still described by only three independent probability amplitudes.

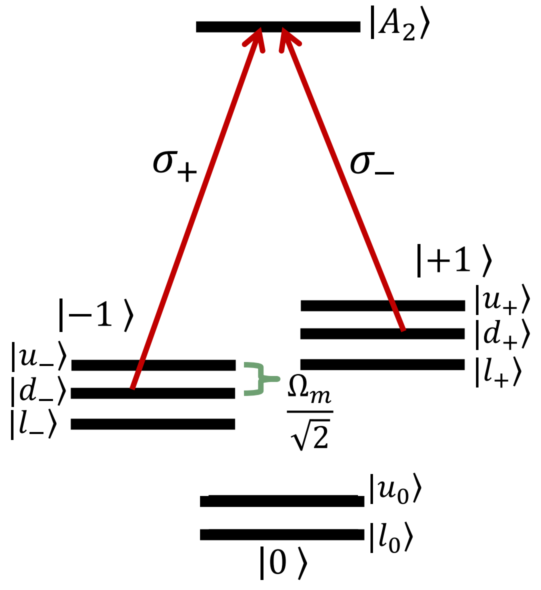

Figure 6.3. Energy level diagram with both the dressed state and bare spin state nature of the ground state levels made explicit. Each of these ground state levels corresponds to a term in (6.5). The two optical fields continue to couple to the transitions between the bare spin states and the $|A_2\rangle$ *excited state.*

As we saw in Chapter IV, CPT can reveal this splitting. We perform a CPT measurement similar to those described in that chapter. Two optical fields with equal intensity and opposite circular polarization drive the two optical transitions of the Λ-configuration. One is held constant on resonance while the other is tuned in frequency. For this measurement we used optical fields with a combined incident power of 6 nW. We measure the emission from $|A_2\rangle$ (fluorescence) as a function of the optical Raman detuning, δ. Throughout the measurement we apply two dressing MW fields on resonance with the two ground-state MW transitions. These have a Rabi frequency of $\Omega_m/2\pi$ = 1 MHz as determined using Rabi oscillation measurements, comparable to the linewidth of the bare spin state transitions. The CPT measurement continues for a duration of 40 μs before it is alternated, as usual, with off-resonant green excitation which reverses any ionization or optical pumping effects. The resulting CPT spectral response is shown in Fig. 6.4.

This CPT trace features five resonances (sharp dips) instead of the single resonance that is observed for the bare spin states. We are limiting this measurement to a single hyperfine state. The CPT resonances shown in Fig. 6.4 correspond to the $m_n = 0$ hyperfine state. CPT resonances for $m_n = -1$ and $m_n = +1$ are 4.4 MHz away (Fig. 4.4) and so do not appear in this measurement. These two hyperfine states just contribute a background.

The resonances in the CPT trace correspond to spin coherences. As shown in Fig. 6.4, these can occur between two different dressed states (for example, between $|l_+\rangle$ and $|u_-\rangle$), and can also arise from the same dressed state (for example, between $|d_+\rangle$ and $|d_-\rangle$). Spin coherences arising from the same dressed state lead to the central CPT

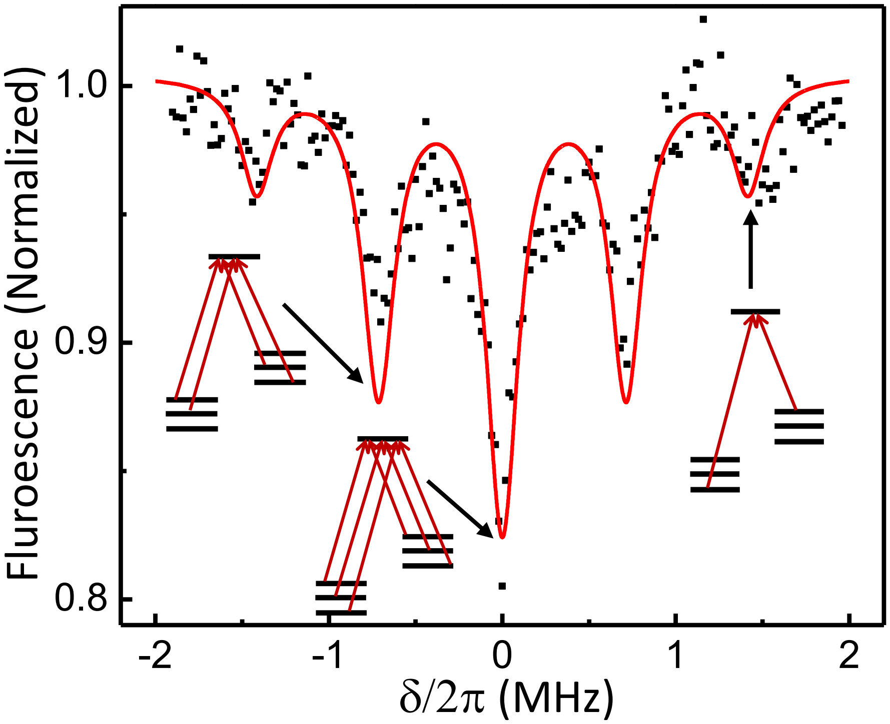

Figure 6.4. Coherent population trapping of dressed spin states. Fluorescence is collected while one optical field is held fixed and the other is tuned. Dips indicate frequencies where the Raman detuning between the two fields is equal to the splitting between dressed state levels associated with different bare spin states. The resonances are labeled with energy level diagrams indicating which coherences are involved in that feature. The solid line is the sum of five Lorentzians with spectral positions calculated from the MW Rabi frequency, relative amplitudes estimated from steady state population considerations (see Section 6.6.3), and linewidths (0.22 MHz) fit to the data.

resonance at $\delta = 0$ (i.e. the frequency different between the two optical fields equals the Zeeman splitting, ω_B, between the bare $|\pm\rangle$ spin states). Spin coherences between $|d\rangle$ and either $|l\rangle$ or $|u\rangle$ lead to CPT resonances at $\delta = \pm\Omega_m/\sqrt{2}$ (recall that $\pm\Omega_m/\sqrt{2}$ are the dressed state splittings), which are the first sidebands in the trace. Spin coherences between $|l\rangle$ and $|u\rangle$ lead to CPT resonances at $\delta = \pm\sqrt{2}\Omega_m$, the second sidebands in the trace. CPT provides a convenient way of observing the dressed state behavior.

The spectral positions of these CPT resonances only depend on the strengths of the MW fields. Fig. 6.5 plots the Ω_m-dependence of the spectral separation between the first sidebands and the central resonance derived from experiments similar to that in Fig. 6.4, confirming the above assignments. The widths and relative depths of the dips are more complicated and will require a more detailed look at the CPT process. This is where we turn next. Afterwards we will be able to return to the CPT measurement and come to some conclusions about the coherence properties of the dressed versus bare spin states.

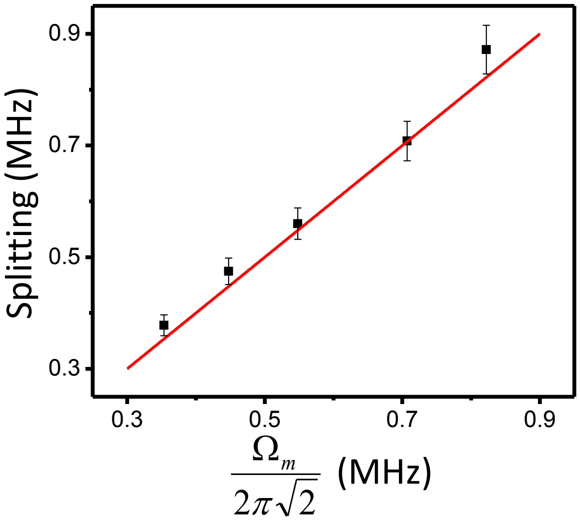

Figure 6.5. The frequency splitting between the central resonance and the first sidebands, as a function of MW Rabi frequency, in CPT measurements similar to that shown in Fig. 6.4. The solid line intercepts with the origin and has a slope of 1.

6.3. Coherent Population Trapping Analysis

We will now look more closely at the theory behind CPT, first in the case of bare spin states and then for dressed spin states. In both cases we will focus on contributions to the CPT linewidth such as power broadening. We also consider the impact of spectral diffusion.

6.3.1. Coherent Population Trapping of Bare Spin States

Consider the Λ-type three-level system we are using with the upper state $|A_2\rangle$ coupling to two lower states $|+\rangle$ and $|-\rangle$ via two nearly resonant optical fields with optical frequencies of ω_+ and ω_- and Rabi frequencies of Ω_+ and Ω_- (both assumed to be real). The wave function of this system in a rotating frame is written as

$$|\Psi\rangle = \tilde{C}_A|A_2\rangle + \tilde{C}_+ e^{i\omega_+ t}|+\rangle + \tilde{C}_- e^{i\omega_- t}|-\rangle. \tag{6.6}$$

The density matrix elements in this rotating frame are defined as $\rho_{ij} = \langle \tilde{C}_i \tilde{C}_j^* \rangle$. The corresponding density matrix equations are then given by [27]

$$\dot{\rho}_{A+} = -(i\Delta_+ + \gamma)\rho_{A+} + \frac{i\Omega_+}{2}(\rho_{AA} - \rho_{++}) - \frac{i\Omega_-}{2}\rho_{-+} \tag{6.7a}$$

$$\dot{\rho}_{A-} = -(i\Delta_- + \gamma)\rho_{A-} + \frac{i\Omega_-}{2}(\rho_{AA} - \rho_{--}) - \frac{i\Omega_+}{2}\rho_{+-} \tag{6.7b}$$

$$\dot{\rho}_{-+} = -(i\delta + \gamma_s)\rho_{-+} + \frac{i\Omega_+}{2}\rho_{-A} - \frac{i\Omega_-}{2}\rho_{A+} \tag{6.7c}$$

$$\dot{\rho}_{AA} = -\Gamma\rho_{AA} + \left(\frac{i\Omega_+}{2}\rho_{A+} + c.c.\right) + \left(\frac{i\Omega_-}{2}\rho_{A-} + c.c.\right) \tag{6.7d}$$

where γ_s and γ are the decay rates for the spin coherence and optical dipole coherence respectively, Γ is the decay rate for the excited state population, Δ_+ and Δ_- are the dipole detunings for the two optical fields, δ is the optical Raman detuning. For our system, $\gamma_s \ll (\gamma, \Gamma)$, and for our experiments we set $\Omega_+ \approx \Omega_-$. (This is a little different from the typical textbook treatment of CPT which usually assumes $\Omega_+ \ll \Omega_-$, with the electron initially in the state $|+\rangle$.)

With $\gamma_s \ll (\gamma, \Gamma)$, ρ_{AA} and the optical dipole coherences characterized by ρ_{A+} and ρ_{A-} can reach steady state on a timescale much faster than that for the spin coherence characterized by ρ_{-+}. In this limit, ρ_{A+} and ρ_{A-} as well as the diagonal matrix elements adiabatically follow the dynamics of ρ_{-+}, with

$$\rho_{A+} = -\frac{i}{2\gamma}(\Omega_+ N_+ + \Omega_- \rho_{-+}) \tag{6.8a}$$

$$\rho_{A-} = -\frac{i}{2\gamma}(\Omega_- N_- + \Omega_+ \rho_{+-}) \tag{6.8a}$$

Where $N_\pm = \rho_\pm - \rho_{AA}$ is the population difference between lower and upper states and we have assumed $|\Delta_\pm| \ll \gamma$ and have thus set $\Delta_\pm = 0$. The steady-state excited-state population is then given by

$$\rho_{AA} = \frac{1}{2\Gamma\gamma}[(\Omega_+^2 N_+ + \Omega_-^2 N_-) + 2\Omega_+\Omega_- Re(\rho_{-+})]. \tag{6.9}$$

The CPT-induced dip in the excited state population is therefore determined by the real part of ρ_{-+}.

Using (6.7c) and (6.8) we arrive at the equation of motion for the spin coherence

$$\dot{\rho}_{-+} = -\left[i\delta + \gamma_s + \frac{\Omega_+^2 + \Omega_-^2}{4\gamma}\right]\rho_{-+} - \frac{\Omega_+\Omega_-}{4\gamma}(N_+ + N_-). \tag{6.10}$$

The $\Omega_\pm^2/4\gamma$ terms in (6.10) correspond to the power broadening of the optically-driven spin transition and thus the power broadening of the CPT resonance. The steady-state solution of ρ_{-+} is given by

$$\rho_{-+} = -\frac{\Omega_+\Omega_-}{4\gamma}\frac{N}{i\delta + \gamma_s + (\Omega_+^2 + \Omega_-^2)/4\gamma} \tag{6.11}$$

Where $N = N_+ + N_-$. For $\rho_{AA} \ll 1$, N can be approximated as the total population in the two lower states, n. Using (6.9) and (6.11), with equal Rabi frequencies for the two optical fields, $\Omega_+ = \Omega_- = \Omega_O$, the excited state population is given by

$$\rho_{AA} = \frac{\Omega_O^2 n}{2\Gamma\gamma}\left[1 - \frac{\Omega_O^2}{2\gamma}\frac{\gamma_s + \Omega_O^2/2\gamma}{\delta^2 + (\gamma_s + \Omega_O^2/2\gamma)^2}\right] \tag{6.12}$$

This population is strongly suppressed when $\Omega_O^2 \gg 2\gamma\gamma_s$ and the two incident optical fields are Raman resonant, ($\delta = 0$). Recall that even when the system is initially prepared in a given lower state, with $\Omega_+ = \Omega_-$ optical excitation can quickly equalize the population in the two lower states.

The power broadening at relatively low intensity for the optical fields scales linearly with this power and is given by $\Omega_O^2/2\gamma$. For larger Ω_O, approaching or exceeding γ, we need to solve (6.11) without the $\rho_{AA} \ll 1$ approximation. In this case we have

$$\rho_{AA} = \frac{\Omega_O^2 \alpha(\delta)}{2\Gamma\gamma + 3\Omega_O^2\alpha(\delta)}, \tag{6.13}$$

where $\alpha(\delta)$ is a lineshape function given by

$$\alpha(\delta) = 1 - \frac{\Omega_O^2}{2\gamma}\frac{\gamma_s + \Omega_O^2/2\gamma}{\delta^2 + (\gamma_s + \Omega_O^2/2\gamma)^2}. \tag{6.14}$$

This shows us that a deviation from the linear intensity dependence of the power broadening is expected when Ω_O approaches or exceeds γ.

Finally, we add the effects of spectral diffusion. As mentioned before, the reinitialization of the NV center with the green laser can lead to a spectral shift of the NV optical transition frequency. This means that, for each experimental run, this frequency will fluctuate. The spectral range of this fluctuation is about 500 MHz for our experiments, far exceeding the intrinsic linewidth (~13 MHz) of the NV center. To account for the effects of this spectral diffusion on the CPT process, we can no longer assume that $|\Delta_\pm| \ll \gamma$ is always true. Equation 6.12 is now modified to

$$\rho_{AA}(\Delta_+) = \frac{\bar{\Omega}_O^2 n}{2\Gamma\gamma}\left[1 - \frac{\bar{\Omega}_O^2}{2\gamma}\frac{\gamma_s + \bar{\Omega}_O^2/2\gamma}{\delta^2 + (\gamma_s + \bar{\Omega}_O^2/2\gamma)^2}\right] \tag{6.15}$$

where $\rho_{ee}(\Delta_+)$ is the excited state population with dipole detuning Δ_+ for the m$_s$ = +1 transition, $\overline{\Omega}_O^2 = \Omega_O^2\gamma^2/(\gamma^2 + \Delta_+^2)$, and we have assumed that $|\delta| \ll \gamma$ and $\rho_{AA}(\Delta_+) \ll 1$. The excited state population must now be averaged over the spectral distribution, $f(\Delta_+)$, of the NV transition frequency giving

$$\rho_{AA} = \int d\,\Delta_+ f(\Delta_+)\rho_{AA}(\Delta_+). \tag{6.16}$$

We can similarly modify (6.13) and (6.14) by replacing $\Omega_O$with $\overline{\Omega}_O$.

6.3.2. Coherent Population Trapping of Dressed Spin States

We now consider CPT for the dressed state system described by the wavefunction in (6.5). The relevant spin coherence can now be written in terms of the dressed-state probability amplitudes as

$$\begin{aligned}\rho_{-+} = {} & \tfrac{1}{4}[\langle C_l C_l^*\rangle + \langle C_u C_u^*\rangle - 2\langle C_d C_d^*\rangle] \\ & + \tfrac{1}{4}\left[(\langle C_l C_d^*\rangle - \langle C_d C_u^*\rangle)e^{\frac{i\Omega_m t}{\sqrt{2}}} + (\langle C_u C_d^*\rangle - \langle C_d C_l^*\rangle)e^{\frac{i\Omega_m t}{\sqrt{2}}}\right] \\ & + \tfrac{1}{4}\left[\langle C_l C_u^*\rangle e^{i\sqrt{2}\Omega_m t} + \langle C_u C_l^*\rangle e^{-i\sqrt{2}\Omega_m t}\right]. \end{aligned} \tag{6.17}$$

The first group of terms in (6.17) describes spin coherences arising from the same dressed state (center dip in Fig. 6.4). The second group of terms describes spin coherences between $|d\rangle$ and either $|l\rangle$ or $|u\rangle$ (first sidebands). The third group describes spin coherences between $|l\rangle$ and $|u\rangle$ (second sidebands).

State $|A_2\rangle$ and the two spin states involved in a given spin coherence term in (6.17) form an effective Λ-type three-level system. Assuming the optical Rabi frequencies are small compared with Ω_m, and that the incident optical fields are Raman resonant with the relevant dressed spin states, non-resonant terms in the density matrix equations can be ignored. Under these conditions, CPT processes for the dressed states can be described by equations similar to those used for the bare spin states (which were shown in (6.7)).

We assume that the relative phase between the two optical fields is the same as that between the two MW fields. (Experimentally this is not necessarily the case, but a difference in relative phases should not affect the power dependence of the CPT linewidth.) The equation of motion for the spin coherence between $|d_+\rangle$ and $|d_-\rangle$ is given by

$$\dot{\rho}_{d-,d+} = -\left[i\delta + \gamma_s + \frac{\Omega_+^2+\Omega_-^2}{4\gamma}\right]\rho_{d-,d+} - \frac{\Omega_+\Omega_-}{4\gamma}(N_{d+} + N_{d-}) \\ -\frac{\Omega_+^2}{4\gamma}(\rho_{d-,l+} + \rho_{d-,u+}) - \frac{\Omega_-^2}{4\gamma}(\rho_{l-,d+} + \rho_{u-,d+}), \tag{6.18}$$

where the spin states are now labeled with an index for the dressed state. Compared with (6.10), the two extra terms represent spin coherences between $|d\rangle$ and either $|l\rangle$ or $|u\rangle$. This reflects coupling between different Λ-type three-level systems. If $\delta \approx 0$, these spin coherences are off-resonant and their contributions are negligible in the low intensity limit. However, when Ω_O/γ^2 approaches Ω_m, these inter-three-level system couplings become important. The steady-state solution for $\rho_{d-,d+}$, with $\Omega_+ = \Omega_- = \Omega_O$, is given by

$$\rho_{d-,d+} = -\frac{\Omega_O^2}{4\gamma}\frac{N_{d+}+N_{d-}+\rho_{d-,l+}^{(0)}+\rho_{d-,u+}^{(0)}+\rho_{l-,d+}^{(0)}+\rho_{u-,d+}^{(0)}}{i\delta+\gamma_s+\Omega_O^2/2\gamma}, \tag{6.19}$$

where for the lowest order corrections we can calculate the off-resonant spin-coherences in (6.18) using (6.11).

Similarly to the bare states, the CPT linewidth for the dressed states scales linearly with the optical power at relatively low intensities. However, we have seen that the linewidth can deviate from this linear dependence when Ω_O/γ^2 approaches or exceeds Ω_m, even though Ω_O remains small compared with γ. Under these conditions, the Λ-type three-level system responsible for the CPT process can no longer be viewed as an isolated system. This makes the CPT process less effective and leads to a smaller power broadening effect than would otherwise be expected.

The effects of spectral diffusion can be included by following the same procedure represented in (6.15) and (6.16).

6.3.3. Amplitudes of the Dressed State CPT Resonances

Before returning to our experimental data and applying the theoretical results regarding the CPT linewidth, we will first consider briefly the relative amplitudes of the dressed state CPT resonances. These relative amplitudes depend on the steady state populations of the dressed states. Away from Raman resonance, the optical fields excite population in $|d\rangle$ and $|b\rangle$ to $|A_2\rangle$ with equal rates. Electron population in $|A_2\rangle$ also decays to $|d\rangle$ and $|b\rangle$ with equal rates, equalizing the population between them. This means that $|C_l| = |C_d| = |C_u|$. As a result, 2/3 of the population is in the $m_s = \pm 1$ states and can contribute to the optical excitation and subsequent emission. The rest is in the $m_s = 0$ state.

For the central CPT resonance in Fig. 6.4, all the dressed spin states associated with $m_s = \pm 1$ are involved. The CPT process then leads to a complete quenching of the excited state population and subsequent fluorescence. (Again, other hyperfine states still contribute a background.)

For the first sideband CPT resonance, only states $|d_+\rangle$, $|d_-\rangle$, and (for instance) $|l_+\rangle$ and $|u_-\rangle$ contribute to the CPT. The CPT process drives the system toward

$|C_l| = \sqrt{2}|C_d| = |C_u|$. Now 1/5 of the total population is both in the $m_s = \pm 1$ states and not in an optically dark state, allowing it to contribute to fluorescence. This is compared to the 2/3 of the population that contributes to fluorescence away from Raman resonance.

For the second sideband CPT resonance, only states (for instance) $|l_+\rangle$ and $|u_-\rangle$ contribute to the CPT. The CPT process now drives the system toward $|C_l| = |C_u|$ while the optical and MW excitations also ensure that the population in $|d\rangle$ and $|b\rangle$ are the same. Now 1/2 of the population is both in the $m_s = \pm 1$ states and not in an optically dark state, allowing it to contribute to fluorescence.

Based on these considerations, assuming steady state conditions apply, we expect a ratio of 100/70/25 for the amplitudes of the central resonance, first sidebands, and second sidebands of the CPT trace.

6.4. CPT Linewidths for Bare and Dressed Spin States: Experimental Results

As we saw in Section 6.3, the linewidth of the CPT resonances is determined by the decay of the underlying spin coherences as well as by power-dependent broadening mechanisms. For an ideal Λ-type system at relatively low intensity, the effective linewidth is given by $2\gamma_s^{eff} = 2\gamma_s + \Omega_O^2/\gamma$ (see (6.11)), scaling linearly with the optical power. To get a handle on the spin coherence decay rate, γ_s, we must account for this optical power broadening.

We first discuss the behavior of the CPT resonance between different spin states associated with the same dressed state (the central dip in the CPT trace shown in Fig. 6.4). Fig. 6.6 shows the linewidth of this resonance as a function of the input laser power, obtained with $\Omega_m/2\pi = 0.83$ MHz and under otherwise similar conditions to the previous

CPT measurement. Also shown in Fig. 6.6 is the power dependent linewidth of the bare state CPT obtained under similar conditions using the method described in Chapter IV. As expected, in both the dressed state and the bare state cases, the CPT linewidth increases with increasing optical power.

The CPT linewidth of the bare spin states deviates from the linear power dependence as Ω_O approaches γ. The deviation from linear power dependence for the dressed spin states, however, occurs at a much lower power due to the inter-Λ-system coupling described above. On top of the data we plot the theoretically calculated power dependent CPT linewidth for both the bare and the dressed spin state cases. For these

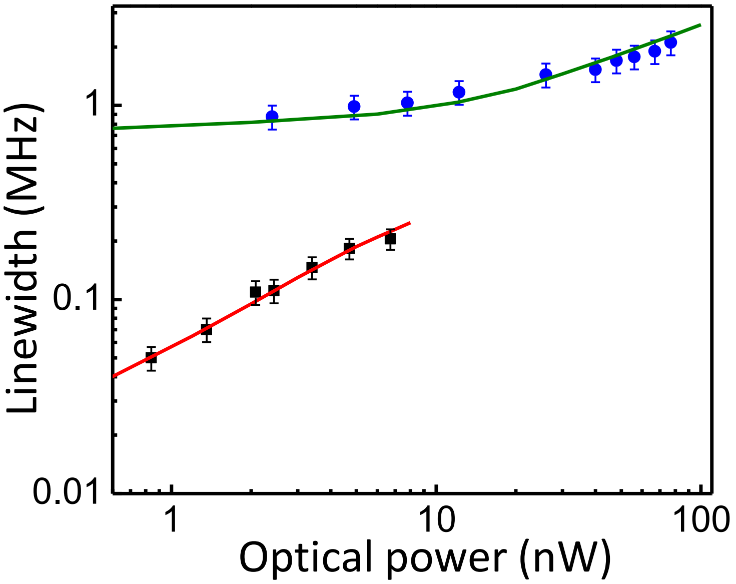

Figure 6.6. The optical power dependent linewidth of the CPT resonance. 1nW corresponds to an estimated $\Omega_0/2\pi$ = 0.74 MHz. Circles (blue) are for the bare spin states. Squares (black) are for the center resonance in the CPT measurement of the dressed spin states. Solid lines (green and red) are the theoretically calculated power dependent broadening. The deviations from linearity described in the text are included as are the effects of spectral diffusion.

calculations we used (6.13), with the effects of spectral diffusion included as described in (6.15) and (6.16), as well as dressed state counterparts. Additionally we used $\gamma/\pi =$ 13 MHz, and Ω_O determined from optically driven Rabi oscillations measurements like those describe in Chapter V.

Fig. 6.7a shows just the dressed state data from Fig. 6.6. Here we can see that the data is consistent with the theoretically expected power broadening suppression. The CPT resonance obtained at the lowest laser power that we used (the lowest power data point in Fig. 6.7a), is shown in Fig. 6.7b.

The linewidth for the dressed states is significantly smaller than for the bare states. From Figs. 6.6 and 6.7 we derive spin transition linewidths in the absence of power broadening (i.e. if the optical power was taken to zero) of approximately 0.75 MHz and 13 kHz for the bare and dressed spin states respectively, about a 50 times

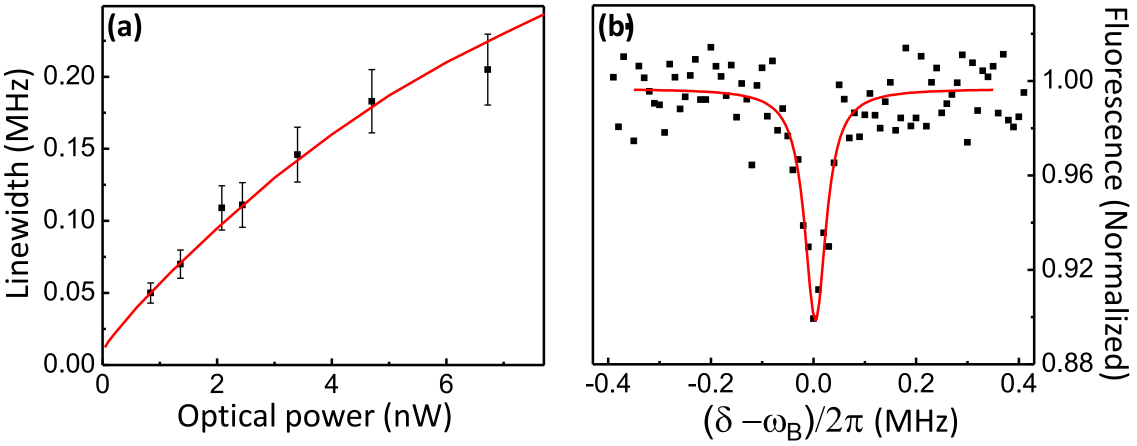

Figure 6.7. (a) The linewidth of the central CPT resonance for the dressed spin states as a function of the incident optical power. The solid line is the theoretically calculated power dependent linewidth. The data is consistent with the theoretically expected deviations from linear power broadening. (b) The central CPT resonance obtained at the lowest optical power used (0.85 nW). The solid line is a fit to a Lorentzian.

reduction. The linewidth for the bare spin states is primarily limited by the bath induced spin dephasing rate. The large reduction of the spin transition linewidth in the dressed state case indicates a spin coherence that is protected from this dephasing by the formation of these dressed states.

In fact the spin coherence of the dressed states is so robust against magnetic fluctuations, it becomes difficult to measure the decoherence rate using our spectral domain CPT measurement. As mentioned above, the intrinsic spin transition linewidth obtained with spin echoes in an isotopically purified diamond is 0.18 kHz [95]. The narrowest intrinsic linewidth obtained in non-isotopically purified diamond is 0.5 kHz [116]. Reducing power broadening down to this scale would require incredibly weak laser powers, making the CPT measurement very difficult.

Additionally, a lower limit is set on our measurement due to transit-time broadening. The CPT measurement had a duration of 40 μs before a green pulse (necessary to counteract ionization and pumping) reset the spin state. This places a limit of about 12 kHz on the smallest linewidth we can measure. This is in good agreement with our results and is consistent with the true linewidth being significantly sharper than our measurements indicate.

Finally we look at the dependence of the CPT linewidth on the power of the MW dressing fields. Fig. 6.8 compares the linewidth of the central resonance with that of the first sideband for different values of Ω_m. This shows that they have similar power-broadened linewidths at relatively large Ω_m. However, when $\Omega_m$decreases below the linewidth of the bare spin transition (i.e. $\Omega_m$is no longer large compared with $|\delta_N|$) the linewidth of the first sideband becomes significantly greater than that of the central resonance as broadening of the sideband due to decoherence becomes comparable to the power broadening.

This demonstrates an important difference between spin coherences between different dressed states (probed by the first sideband CPT resonance) and spin coherences arising from the same dressed state (probed by the central CPT resonance). The protection of the spin coherence between different dressed states requires that Ω_m be large compared with $|\delta_N|$. This is not necessary for spin coherences associated with the same dressed state. In this case, the formation of the dressed state enforces an energy and phase correlation between the $m_s = +1$ and $m_s = -1$ parts of this same dressed state. While

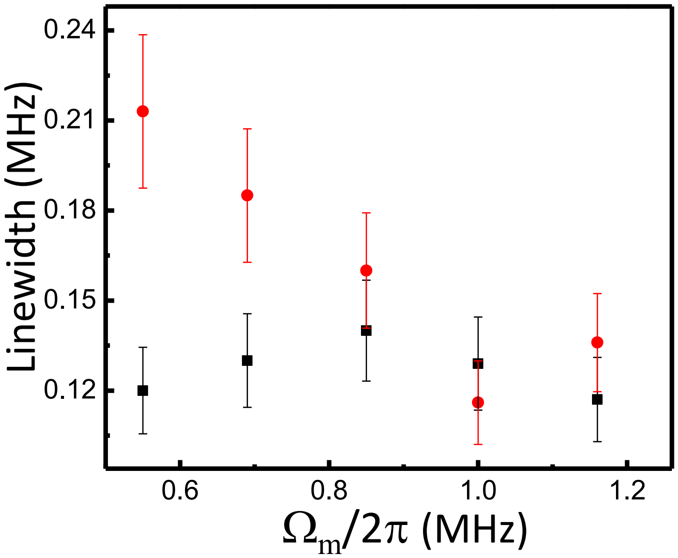

Figure 6.8. The linewidth of the first CPT sideband (red, circles) and the central CPT resonance (black, squares) as a function of Ω_m *with an incident optical power of 2.5 nW. At higher MW power the resonances exhibit similar power broadening. At lower MW power the dressed state decoherence protection breaks down for the sideband, but not for the center resonance.*

the resulting spin coherences are set by the MW dressing fields and cannot be independently controlled, they do illustrate the robustness of the dressed states against magnetic fluctuations. Most applications will need to use the spin coherences between different dressed states.

6.5. Conclusion

We have demonstrated a continuous dynamical decoupling technique for protecting the NV center electron spin from bath induced decoherence. Continuous MW fields dressed the ground state spins, producing states that are insensitive to small fluctuations in the magnetic field. We used CPT measurements via the optical transitions to investigate these dressed states. When power broadening effects were taken into account, we estimated an improvement of at least 50 times in the spin transition linewidth.

For quantum information applications, dressed spin states could be used directly as qubits. With Ω_m over 100 MHz, which has been achieved in earlier studies [117], a nearly complete suppression of spin dephasing could be attained. Our CPT measurements also indicate the feasibility of performing quantum control of dressed spin qubits through off-resonant optical Raman transitions, similar to those described in Chapter V with bare spin states. The dressed spin states would be especially useful when dynamical decoupling is in conflict with the desired quantum operations or when applications need continuous, rather than intermittent, decoupling, such as in the cooling of a mechanical oscillator via coupling to an electron spin or in spin-based cavity QED.

CHAPTER VII

CONCLUSION

7.1. Summary

Atom-field interactions are the basis for some of the most promising advances in quantum technologies. Experimenters are using these interactions, not just for state measurement, but increasingly for the manipulation of an atom's internal quantum states. The precise, comprehensive, and coherent control that has been developed regarding radiation fields, translates into precise, comprehensive, and coherent control over these atomic states.

In this dissertation we have extended this control, particularly optical control, as it is applied to one of the most fruitful atom-like solid-state systems currently being investigated, the diamond NV center. We developed methods for controlling the NV spin state using two-photon ODROs and using STIRAP. The fact that these processes do not populate the excited state lets them avoid the dechoerences associated with the optical dipole transitions. The two methods were compared, and various other decoherence effects were investigated. We concluded from this analysis that ODROs provide faster control but are limited by both spectral diffusion and the ground state spin dephasing, while STIRAP is slower and still sensitive to dephasing but is much more robust against spectral diffusion. We then confirmed the viability of these spin control techniques by applying them in two measurement processes. ODROs successfully produced the spin rotations central to a Ramsey fringe measurement of spin dephasing. STIRAP allowed us to execute a spatially dependent spin transfer, and to take the first steps toward using this for a subwavelength spatial resolution of these solid-state spins.

We also used optical fields to demonstrate CPT effects. Our CPT used a natural Λ-type energy level configuration within the NV center, and did not require the strong strain or magnetic fields necessary in some of the first realizations of CPT in this system. We showed that the CPT can be nuclear spin dependent, revealing the hyperfine splitting of the electronic spin states. Experiments using a continuous MW field to create a dynamic Stark splitting of the ground spin states suggested that CPT measurements would be useful for probing dressed state spins.

We took advantage of this finding and used CPT to investigate the coherence properties of a certain set of MW dressed states. These were expected to be particularly insensitive to the primary decoherence mechanism for NV center ground state spins, fluctuations of a spin-bath-induced magnetic field. We studied the power dependence of the CPT resonance linewidth for coherences associated with these dressed states. When optical power broadening effects were taken into account, we were able to conclude that the linewidth of the transitions underlying the CPT process was reduced by at least a factor of 50 when the dressed spin states were used instead of the bare spin states. The improvement in coherence time was likely even greater since our measurements were limited by transit-time broadening. This decoherence reduction method, unlike some other methods, gives continuous protection and is relatively easy to implement.

When combined with the advantages already inherent in a solid-state spin system, the experimental advancements we have described make such a system even more attractive as a tool for implementing applications of quantum control.

7.2. Future Work

Many of the experiments we have described would benefit from a decrease in the spectral diffusion. It has been shown elsewhere that replacing the ubiquitous green repump pulse with one at 575 nm, resonant with the neutrally charged NV state, can reverse ionization without the unwanted spectral diffusion [97]. Incorporating this would allow us to use much smaller dipole detunings for our optical fields without worrying about driving the optical transition directly. The result would be significantly faster ODRO's and STIRAP, making it easier to expand the use of these control methods to applications, such as state transfer between electron and nuclear spins, which are usually done with MW control.

It should also be possible to combine the optical spin control with the dressed state approach for protecting the spin from decoherence. This would generate a coherently controllable, solid-state spin with exceptional coherence properties, perhaps improved even more by the use of higher purity diamond samples.

The optical control methods we described are especially suited for building a quantum network by using closely spaced NV centers, or by incorporating the NV center into cavity QED or optomechanical systems. In the last case, spin-phonon coupling has been demonstrated using NV center ground spin states [118]. However the excited states, which are much more sensitive to strain, exhibit a coupling to phonons that is several orders of magnitude stronger. The optical control method we developed would allow us to take advantage of these states for mediating the spin-phonon coupling while avoiding the decoherence associated with them.

Finally, it may be possible to extend some or all of the techniques presented here to other atom-like solid-state systems such as SiC. Experimenters continue to sift through the many candidate systems to find ones with useful spin properties. The success of the NV center has produced a wide range of techniques which can be immediately adapted for use in a novel system. Meanwhile research using the diamond NV center continues to be productive, and we hope that the work we have described will lead to even more success based on this remarkable solid-state spin.

REFERENCES CITED

[1] G. Leuchs and T. Beth, Eds., *Quantum Information Processing.* Weinheim: WILEY-VCH, 2003.

[2] J. Keeler, *Understanding NMR Spectroscopy.* Chichester: John Wiley and Sons Ltd., 2005.

[3] M. Le Bellac, *A Short Introduction to Quantum Information and Quantum Computation.* Cambridge: Cambridge University Press, 2006.

[4] S. L. Braunstein and H.-K. Lo, Eds., *Scalable Quantum Computers*. Berlin: WILEY-VCH, 2001.

[5] V. Giovannetti, S. Lloyd, and L. Maccone, “Quantum Metrology,” *Phys. Rev. Lett.*, vol. 96, pp. 010401-010404, 2006.

[6] G. Kucsko, P. C. Maurer, N. Y. Yao, M. Kubo, H. J. Noh, P. K. Lo, H. Park, and M. D. Lukin, “Nanometre-scale thermometry in a living cell,” *Nature*, vol. 500, pp. 54-58, 2013.

[7] C. Monroe, “Quantum information processing with atoms and photons,” *Nature*, vol. 416, pp. 238-246, 2002.

[8] H. Walther, B. T. H. Varcoe, B.-G. Englert, and T. Becker, “Cavity quantum electrodynamics,” *Rep. Prog. Phys.*, vol. 69, pp. 1325-1382, 2006.

[9] T. D. Ladd, F. Jelezko, R. Laflamme, Y. Nakamura, C. Monroe, and J. L. O’Brien, “Quantum computers,” *Nature*, vol. 464, pp. 45-53, 2010.

[10] S. Chu, “Cold atoms and quantum control,” *Nature*, vol. 416, pp. 206-210, 2002.

[11] J. Stolze and D. Suter, *Quantum Computing: A Short Course from Theory to Experiment*. Weinheim: WILEY-VCH, 2004.

[12] P. Kok and B. W. Lovett, *Introduction to Optical Quantum Information Processing*. Cambridge: Cambridge University Press, 2010.

[13] H. Haffner, C. F. Roos, and R. Blatt, “Quantum computing with trapped ions,” *Phys. Rep.*, vol 469, pp. 155-203, 2008.

[14] I. Bloch, “Quantum coherence and entanglement with ultracold atoms in optical lattices,” *Nature*, vol. 453, pp. 1016-1022, 2008.

[15] C. Kloeffel and D. Loss, “Prospects for spin-based quantum computing in quantum dots,” *Annu. Rev. Condens. Matter. Phys*., vol. 4, 51-81, 2013.

[16] L. Gordon, J. R. Weber, J. B. Varley, A. Janotti, D. D. Awschalom, and C. G. Van de Walle, “Quantum computing with defects,” *MRS Bull.*, vol. 38, 802-807, 2013.

[17] A. D. Greentree, B. A. Fairchild, F. M. Hossain, and S. Prawer, “Diamond integrated quantum photonics,” *Mater. Today*, vol. 11, pp. 22-31, 2008.

[18] R. Hanson and D. D. Awschalom, “Coherent manipulation of single spins in semiconductors,” *Nature*, vol. 453, pp. 1043-1049, 2008.

[19] D. D. Awschalom, L. C. Bassett, A. S. Dzurak, E. L. Hu, and J. R. Petta, “Quantum Spintronics: Engineering and manipulating atom-like spins in semiconductors,” *Science*, vol. 339, pp. 1174-1179, 2013.

[20] J. Wrachtrup and F. Jelezko, “Processing quantum information in diamond,” *J. Phys.- Condens. Mat.,* vol. 18, pp. S807-S824, 2006.

[21] S. Prawer and A. D. Greentree, “Diamond for quantum computing,” *Science*, vol. 320, 1601-1602, 2008.

[22] C. Santori, D. Fattal, and Y. Yamamoto, *Single-photon devices and applications*. Weinheim:WILEY-VCH, 2010.

[23] J. R. Weber, W. F. Koehl, J. B. Varley, A. Janotti, B. B. Buckley, C. G. Van de Walle, and D. D. Awschalom, “Defects in SiC for quantum computing,” *J. Appl. Phys.*, vol. 109, pp. 102417-102421, 2011.

[24] W. F. Koehl, B. B. Buckley, F. J. Heremans, G. Calusine, and D. D. Awschalom, “Room temperature coherent control of defect spin qubits in silicon carbide,” *Nature*, vol. 479, pp. 84-87, 2011.

[25] M. S. Shahriar, P. R. Hemmer, S. Lloyd, P. S. Bhatia, and A. E. Craig, “Solid-state quantum computing using spectral holes,” *Phys. Rev. A*, vol. 66, pp. 032301-032306, 2002.

[26] M. Fleischhauer, A. Imamoglu, and J. P. Marangos, “Electromagnetically induced transparency: Optics in coherent media,” *Rev. of Mod. Phys.*, vol. 77, pp. 633-673, 2005.

[27] M. O. Scully and M. S. Zubairy, *Quantum Optics*. Cambridge: Cambridge University Press, 1997.

[28] G. Compagno, R. Passante, and F. Persico, *Atom-Field Interactions and Dressed Atoms*. Cambridge: Cambridge University Press, 1995.

[29] F. Jelezko and J. Wrachtrup, "Single defect centres in diamond: A review," *Phys. State. Sol.*, vol. 203, pp. 3207-3225, 2006.

[30] T. A. Kennedy, J. S. Colton, J. E. Butler, R. C. Linares, and P. J. Doering, "Long coherence times at 300 K for nitrogen-vacancy center spins in diamond grown by chemical vapor deposition," *App. Phys. Lett.*, vol. 83, pp. 4190-4192, 2003.

[31] A. M. Zaitsev, *Optical Properties of Diamond: A Data Handbook*. Berlin: Springer, 2001.

[32] M. W. Doherty, N. B. Manson, P. Delaney, and L. C. L. Hollenberg, "The negatively charged nitrogen-vacancy centre in diamond: the electronic solution," *New J. Phys.,* vol. 13, p. 025019, 2011.

[33] M. W. Doherty, F. Dolde, H. Fedder, F. Jelezko, J. Wrachtrup, N. B. Manson, and L. C. L. Hollenberg, "Theory of the ground-state spin of the NV- center in diamond," *Phys. Rev. B*, vol. 85, pp. 205203-205223, 2012.

[34] N. B. Manson, J. P. Harrison, and M. J. Sellars, "Nitrogen-vacancy center in diamond: Model of the electronic structure and associated dynamics," *Phys. Rev. B*, vol. 74, pp. 104303-104313, 2006.

[35] J. R. Maze, A. Gali, E. Togan, Y. Chu, A. Trifonov, E. Kaxiras, and M. D. Lukin, "Properties of nitrogen-vacancy centers in diamond: the group theoretic approach," *New J. Phys*., vol. 13, pp. 025025-025048, 2011.

[36] A. Lenef and S. C. Rand, "Electronic structure of the N-V center in diamond: Theory," *Phys. Rev. B*, vol. 53, pp. 13441-13455, 1996.

[37] M. W. Doherty, N. B. Manson, P. Delaney, F. Jelezko, J. Wrachtrup, and L. C. L. Hollenberg, "The nitrogen-vacancy colour centre in diamond," *Phys. Rep.*, vol. 528, pp. 1-45, 2013.

[38] L. du Preez, Ph.D. Thesis, University of Witwatersrand, Johannesburg, South Africa, 1965.

[39] C. D. Clark and C. A. Norris, "Photoluminescence associated with the 1.673, 1.944, and 2.498 eV centres in diamond," *J. Phys. C: Solid St. Phys.*, vol. 4, pp. 2223-2229, 1971.

[40] G. Davies and M. F. Hamer, "Optical studies of the 1.945 eV vibronic band in diamond," *Proc. R. Soc. Lond. A*, vol. 348, pp. 285-298, 1976.

[41] J. H. N. Loubser and J. A. van Wyk, "Electron spin resonance in annealed type1b diamond," *Diamond Res.*, vol. 11, pp. 4-7, 1977.

[42] N. R. S. Reddy, N. B. Manson, and E. R. Krausz, "Two-laser spectral hole burning in a colour centre in diamond," *J. Lumin.*, vol. 38, pp. 46-47, 1987.

[43] E. van Oort, N. B. Manson, and M. Glasbeek, "Optically detected spin coherence of the diamond N-V centre in its triplet ground state," *J. Phys. C: Solid State Phys.*, vol. 21, pp. 4385-4391, 1988.

[44] A. Gruber, A. Drabenstedt, C. Tietz, L. Fleury, J. Wrachtrup, and C. von Borczyskowski, "Scanning confocal optical microscopy and magnetic resonance on single defect centers," *Science*, vol. 276, pp. 2012-2014, 1997.

[45] R. Brouri, A. Beveratos, J. Poizat, and P. Grangier, "Photon antibunching in the fluorescence of individual color centers in diamond," *Opt. Lett.,* vol. 25, pp. 1294-1296, 2000.

[46] F. Jelezko, T. Gaebel, I. Popa, A. Gruber, and J. Wrachtrup, "Observation of coherent oscillations in a single electron spin," *Phys. Rev. Lett.,* vol. 92, pp. 076401-076405, 2004.

[47] R. Hanson, O. Gywat, and D. D. Awschalom, "Room-temperature manipulation and decoherence of a single spin in diamond," *Phys. Rev. B,* vol. 74, pp. 161203-161206, 2006.

[48] R. Hanson, V. V. Dobrovitski, A. E. Feiguin, O. Gywat, and D. D. Awschalom, "Coherent dynamics of a single spin interacting with an adjustable spin bath," *Science,* vol. 320, pp. 352-355, 2008.

[49] F. Jelezko, T. Gaebel, I. Popa, M. Domhan, A. Gruber, and J. Wrachtrup, "Observation of coherent oscillation of a single nuclear spin and realization of a two-qubit conditional quantum gate," *Phys. Rev. Lett.,* vol. 93, pp. 130501-130504, 2004.

[50] L. Childress, M. V. G. Dutt, J. M. Taylor, A. S. Zibrov, F. Jelezko, J. Wrachtrup, P. R. Hemmer, and M. D. Lukin, "Coherent dynamics of coupled electron and nuclear spin qubits in diamond," *Science,* vol. 314, pp. 281-285, 2006.

[51] M. V. G. Dutt, L. Childress, L. Jiang, E. Togan, J. Maze, F. Jelezko, E. Togan, J. Maze, F. Jelezko, A. S. Zibrov, P. R. Hemmer, and M. D. Lukin, "Quantum register based on individual electronic and nuclear spin qubits in diamond," *Science,* vol. 316, pp. 312-316, 2007.

[52] T. Gaebel, M. Domhan, I. Popa, C. Wittmann, P. Neumann, F. Jelezko, J. R. Rabeau, N. Stavrias, A. D. Greentree, S. Prawer, J. Meijer, J. Twamley, P. H. Hemmer, and J. Wrachtrup, "Room-temperature coherent coupling of single spins in diamond," *Nat. Phys.*, vol. 2, pp. 408-413, 2006.

[53] R. Hanson, F. M. Mendoza, R. J. Epstein, and D. D. Awschalom, "Polarization and readout of coupled single spins in diamond," *Phys. Rev. Lett.*, vol. 97, pp. 087601-087604, 2006.

[54] B. Smeltzer, J. McIntyre, and L. Childress, "Robust control of individual nuclear spins in diamond," *Phys. Rev. A*, vol 80, pp. 050302-050305, 2009.

[55] G. D. Fuchs, G. Burkard, P. V. Klimov, and D. D. Awschalom, "A quantum memory intrinsic to single nitrogen-vacancy centers in diamond," *Nat. Phys.,* vol. 7, pp. 789-793, 2011.

[56] P. Neumann, J. Beck, M. Steiner, F. Rempp, H. Fedder, P. R. Hemmer, J. Wrachtrup, F. Jelezko, "Single-shot readout of a single nuclear spin," *Science,* vol. 329, pp. 542-544, 2010.

[57] J. M. Taylor, P. Cappellaro, L. Childress, L. Jiang, D. Budker, P. R. Hemmer, A. Yacoby, R. Walsworth, and M. D. Lukin, "High-sensitivity diamond magnetometer with nanoscale resolution," *Nat. Phys.,* vol. 4, pp. 810-816, 2008.

[58] S. Hong, M. S. Grinolds, L. M. Pham, D. L. Sage, L. Luan, R. L. Walsworth, and A. Yacoby, "Nanoscale magnetometry with NV centers in diamond," *MRS Bull.*, vol 38, pp. 155-161, 2013.

[59] A. Drabenstedt, L. Fleury, C. Tietz, F. Jelezko, S. Kilin, A. Nizovtzev, and J. Wrachtrup, "Low-temperature microscopy and spectroscopy on single defect centers in diamond," *Phys. Rev. B*, vol. 60, pp. 11503-11508, 1999.

[60] A. Batalov, V. Jacques, F. Kaiser, P. Siyushev, P. Neumann, L. J. Rogers, R. L. McMurtrie, N. B. Manson, F. Jelezko, and J. Wrachtrup, "Low temperature studies of the excited-state structure of negatively charged nitrogen-vacancy color centers in diamond," *Phys. Rev. Lett.*, vol. 102, pp. 195506-195509, 2009.

[61] F. Jelezcko, I. Popa, A. Gruber, C. Tietz, J. Wrachtrup, A. Nizovtsev, and S. Kilin, "Single spin states in a defect center resolved by optical spectroscopy," *App. Phys. Lett.*, vol. 81, pp. 2160-2162, 2002.

[62] E. Togan, Y. Chu, A. S. Trifonov, L. Jiang, J. Maze, L. Childress, M. V. G. Dutt, A. S. Sorensen, P. R. Hemmer, A. S. Zibrov, and M. D. Lukin, “Quantum entanglement between an optical photon and a solid-state spin qubit,” *Nature,* vol. 466, pp. 730-734, 2010.

[63] H. Bernien, L. Childress, L. Robledo, M. Markham, D. Twitchen, and R. Hanson, “Two-photon quantum interference from separate nitrogen vacancy centers in diamond,” *Phys. Rev. Lett.,* vol. 108, pp. 043604-043608, 2012.

[64] A. Sipahigil, M. L. Goldman, E. Togan, Y. Chu, M. Markham, D. J. Twitchen, A. S. Zibrov, A. Kubanek, and M. D. Lukin, “Quantum interference of single photons from remote nitrogen-vacancy centers in diamond,” *Phys. Rev. Lett.*, vol 108, pp. 143601-143605, 2012.

[65] H. Bernien, B. Hensen, W. Pfaff, G. Koolstra, M. S. Blok, L. Robledo, T. H. Taminiau, M. Markham, D. J. Twitchen, L. Childress, and R. Hanson, “Heralded entanglement between solid-state qubits separated by three metres,” *Nature,* vol. 497, pp. 86-90, 2013.

[66] C. Santori, P. Tamarat, P. Neumann, J. Wrachrup, D. Fattal, R. G. Beausoleil, J. Rabeau, P. Olivero, A. D. Greentree, S. Prawer, F. Jelezko, and P. Hemmer, “Coherent population trapping of single spins in diamond under optical excitation,” *Phys. Rev. Lett.*, vol. 97, pp. 247401-247404, 2006.

[67] L. Robledo, H. Bernien, I. van Weperen, and R. Hanson, “Control and coherence of the optical transition of single nitrogen vacancy centers in diamond,” *Phys. Rev. Lett.,* vol. 105, pp. 177403-177406, 2010.

[68] E. Togan, Y. Chu, A. Imamoglu, and M. D. Lukin, “Laser cooling and real-time measurement of the nuclear spin environment of a solid-state qubit,” *Nature,* vol. 478, pp. 497-501, 2011.

[69] L. Robledo, L. Childress, H. Bernien, B. Hensen, F. A. Alkemade, and R. Hanson, “High-fidelity projective read-out of a solid-state spin quantum register,” *Nature,*vol. 477, pp. 574-578, 2011.

[70] D. A. Golter, K. N. Dinyari, and H. Wang, “Nuclear-spin-dependent coherent population trapping of single nitrogen-vacancy centers in diamond,” *Phys. Rev. A*, vol. 87, pp. 035801-035805, 2013.

[71] D. A. Golter and H. Wang, “Optically driven Rabi oscillations and adiabatic passage of single electron spins in diamond,” *Phys. Rev. Lett.*, vol. 112, pp. 116403-116407, 2014.

[72] D. A. Golter, T. K. Baldwin, and H. Wang, “Protecting a solid-state spin from decoherence using dressed spin states,” *Phys. Rev. Lett.*, vol. 113, pp. 237601-237605, 2014.

[73] L. Marseglia, J. P. Hadden, A. C. Stanley-Clarke, J. P. Harrison, B. Patton, Y.-L. D. Ho, B. Naydenov, F. Jelezko, J. Meijer, P. R. Dolan, J. M. Smith, J. G. Rarity, and J. L. O’Brien, “Nanofabricated solid immersion lenses registered to single emitters in diamond,” *App. Phys. Lett.*, vol. 98, pp. 133107-133109, 2011.

[74] M. Jamali, I. Gerhards, M. Rezai, K. Frenner, H. Fedder, and J. Wrachtrup, “Microscopic diamond Solid-Immersion-Lenses fabricated around single defect centers by focused ion beam milling,” Unpublished.

[75] R. J. Epstein, F. M. Mendoza, Y. K. Kato, and D. D. Awschalom, “Anisotropic interactions of a single spin and dark-spin spectroscopy in diamond,” *Nature*, vol. 1, pp. 94-98, 2005.

[76] P. Tamarat, T. Gaebel, J. R. Rabeau, M. Khan, A. D. Greentree, H. Wilson, L. C. L. Hollenberg, S. Prawer, P. Hemmer, F. Jelezko, and J. Wrachtrup, “Stark shift control of single optical centers in diamond,” *Phys. Rev. Lett.*, vol 97, pp. 083002-083005, 2006.

[77] T. P. Mayer Alegre, C. Santori, G. Medeiros-Ribeiro, and R. G. Beausoleil, “Polarization-selectrive excitation of nitrogen vacancy centers in diamond,” *Phys. Rev. B*, vol 76, pp. 165205-165209, 2007

[78] P. R. Berman and V. S. Malinovsky, *Principles of Laser Spectroscopy and Quantum Optics*. Princeton and Oxford: Princeton University Press, 2001.

[79] C. Wei and N. B. Manson, “Observation of electromagnetically induced transparency within an electron spin resonance transition,” *J. Opt. B-Quantum S. O.*, vol 1, pp. 464-468, 1999.

[80] P. R. Hemmer, A. V. Turukhin, M. S. Shahriar, and J. A. Musser, “Raman-excited spin coherences in nitrogen-vacancy color centers in diamond,” *Opt. Lett.*, Vol 26, pp. 361-363, 2001.

[81] C. Santori, D. Fattal, S. M. Spillane, M. Fiorentino, R. G. Beausoleil, A. D. Grentree, P. Olivero, M. Draganski, J. R. Rabeau, P. Reichart, B. C. Gibson, S. Rubanov, D. N. Jamieson, and S. Prawer, “Coherent population trapping in diamond N-V centers at zero magnetic field,” *Opt. Express*, vol. 14, pp, 7986-7994, 2006.

[82] P. Tamarat, N. B. Manson, J. P. Harrison, R. L. McMurtrie, A. Nizovtsev, C. Santori, R. G. Beausoleil, P. Neumann, T. Gaebel, F. Jelezko, P. Hemmer, and J. Wrachtrup, “Spin-flip and spin-conserving optical transitions of the nitrogen-vacancy centre in diamond,” *New J. Phys.*, vol. 10, pp. 045004-045012, 2008.

[83] C. Cohen-Tannoudji, J. Dupont-Roc, and G. Grynberg, *Atom-Photon Interaction*, New York: Wiley, 1998.

[84] C. Wei and N. B. Manson, “Observation of the dynamic Stark effect on electromagnetically induced transparency,” *Phys. Rev. A*, vol. 60, pp. 2540-2546, 1999.

[85] L. Yang, L. Zhang, X. Li, L. Han, G. Fu, N. B. Manson, D. Suter, and C. Wei, “Autler-Townes effect in a strongly driven electromagnetically induced transparency resonance,” *Phys. Rev. A*, vol. 72, pp. 053801-053808, 2005.

[86] N. Y. Yao, L. Jiang, A. V. Gorshkov, P. C. Maurer, G. Giedke, J. I. Cirac, and M. D. Lukin, “Scalable architecture for a room temperature solid-state quantum information processor,” *Nat. Commun.*, vol. 3, p. 800, 2012.

[87] A. Imamoglu, D. D. Awschalom, G. Burkard, D. P. DiVincenzo, D. Loss, M. Sherwin, and A. Small, “Quantum information processing using quantum dot spins and cavity QED,” *Phys. Rev. Lett.*, vol. 83, pp. 4204-4207 ,1999.

[88] A. Albrecht, A. Retzker, F. Jelezko, and M. B. Plenio, “Coupling of nitrogen vacancy centres in nanodiamonds by means of phonons,” *New J. Phys.*, vol. 15, pp. 083014-083029, 2013.

[89] C. G. Yale, B. B. Buckley, D. J. Christle, G. Burkard, F. J. Heremans, L. C. Bassett, and D. D. Awschalom, “All-optical control of a solid-state spin using coherent dark states,” *PNAS*, vol. 110, pp. 7595-7600, 2013.

[90] D. D. Yavuz, P. B. Kalatunga, E. Urban, T. A. Johnson, N. Proite, T. Henage, T. G. Walker, and M. Saffman, “Fast ground state manipulation of neutral atoms in microscopic optical traps,” Phys. Rev. Lett., vol. 96, pp. 063001-063004, 2006.

[91] T. M. Sweeney, C. Phelps, and H. L. Wang, “Quantum control of electron spins in the two-dimensional electron gas of a CdTe quantum well with a pair of Raman-resonant phase-locked laser pulses,” *Phys. Rev. B*, vol. 84, pp. 075321-075326, 2011.

[92] B. Smeltzer, L. Childress, and A. Gali, “13C hyperfine inderactions in the nitrogen-vacancy centre in diamond,” *New J. Phys.*, vol. 13, pp.025021-025029, 2011.

[93] S. Kolkowitz, Q. P. Unterreithmeier, S. D. Bennett, and M. D. Lukin, "Sensing distant nuclear spins with a single electron spin," *Phys. Rev. Lett.*, vol. 109, pp. 137601-137605, 2012.

[94] J. Oreg, F. T. Hioe, and J. H. Eberly, "Adiabatic following in multilevel systems," *Phys. Rev. A*, vol. 29, pp. 690-697, 1984.

[95] G. Balasubramanian, P. Neumann, D. Twitchen, M. Markham, R. Kolesov, N. Mizuochi, J. Isoya, J. Achard, J. Beck, J. Tissler, V. Jacques, P. R. Hemmer, F. Jelezko, and J. Wrachtrup, "Ultralong spin coherence time in isotopically engineered diamond," *Nat. Mater.*, vol. 8, pp. 383-387, 2009.

[96] G. deLange, Z. H. Wang, D. Riste, V. V. Dobrovitski, and R. Hanson, "Universal dynamical decoupling of a single solid-state spin from a spin bath," *Science*, vol. 330, pp. 60-63, 2010.

[97] P. Siyushev, H. Pinto, M. Voros, A. Gali, F. Jelezko, and J. Wrachtrup, "Optically controlled switching of the charge state of a single nitrogen-vacancy center in diamond at cryogenic temperatures," *Phys. Rev. Lett.*, vol. 110, pp. 167402-167406, 2013.

[98] S. Castelletto, X. Li, and M. Gu, "Frontiers in diffraction unlimited optical methods for spin manipulation, magnetic field sensing and imaging using diamond nitrogen vacancy defects," *Nanophoton.*, vol. 1, pp. 139-153, 2012.

[99] K. Y. Han, K. I. Willig, E. Rittweger, F. Jelezko, C. Eggeling, and S. W. Hell, "Three-dimensional stimulated emission depletion microscopy of nitrogen-vacancy centers in diamond using continuous-wave light," *Nano Lett.*, vol. 9, pp. 3323-3329, 2009.

[100] K. Y. Han, S. K. Kim, C. Eggeling, and S. W. Hell, "Metastable dark states enable ground state depletion microscopy of nitrogen vacancy centers in diamond with diffraction-unlimited resolution," *Nano Lett.*, vol. 10, pp. 3199-3203, 2010.

[101] P. C. Maurer, J. R. Maze, P. L. Stanwix, L. Jiang, A. V. Gorshkov, A. A. Zibrov, B. Harke, J. S. Hodges, A. S. Zibrov, A. Yacoby, D. Twitchen, S. W. Hell, R. L. Walsworth, and M. D. Lukin, "Far-field optical imaging and manipulation of individual spins with nanoscale resolution," *Nat. Phys.*, vol. 6, pp. 912-918, 2010.

[102] D. D. Yavuz and N. A. Proite, "Nanoscale resolution fluorescence microscopy using electromagnetically induced transparency," *Phys. Rev. A*, vol. 76, pp. 041802-041805, 2007.

[103] A. V. Gorshkov, L. Jiang, M. Greiner, P. Zoller, and M. D. Lukin, "Coherent quantum optical control with subwavelength resolution," *Phys. Rev. Lett.*, vol. 100, pp. 093005-093008, 2008.

[104] L. Viola, E. Knill, and S. Lloyd, “Dynamical Decoupling of Open Quantum Systems,” Phys. Rev. Lett., vol. 82, pp. 2417-2421, 1999.

[105] M. J. Biercuk, H. Uys, A. P. VanDevender, N. Shiga, W. M. Itano, and J. J. Bollinger, “Optimized dynamical decoupling in a model quantum memory,” *Nature*, vol. 458, pp. 996-1000, 2009.

[106] H. Bluhm, S. Foletti, I. Neder, M. Rudner, D. Mahalu, V. Umansky, and A. Yacoby, “Dephasing time of GaAs electron-spin qubits coupled to a nuclear bath exceeding 200 μs,” *Nat. Phys.*, vol. 7, pp. 109-113, 2011.

[107] T. van der Sar, Z. H. Wang, M. S. Blok, H. Bernein, T. H. Taminiau, D. M. Toyli, D. A. Lidar, D. D. Awschalom, R. Hanson, and V. V. Dobrovitski, “Decoherence-protected quantum gates for a hybrid solid-state spin register,” *Nature*, vol. 484, pp. 82-86, 2012.

[108] P. C. Maurer, G. Kucsko, C. Latta, L. Jiang, N. Y. Yao, S. D. Bennett, F. Pastawski, D. Hunger, N. Chisholm, M. Markham, D. J. Twitchen, J. I. Cirac, and M. D. Lukin, “Room-temperature quantum bit memory exceeding one second,” *Science*, vol. 336, 2012.

[109] P. Rabl, P. Cappellaro, M. V. G. Dutt, L. Jiang, J. R. Maze, and M. D. Lukin, “Strong magnetic coupling between an electronic spin qubit and a mechanical resonator,” *Phys. Rev. B*, vol. 79, pp. 041302-041305, 2009.

[110] N. Aharon, M. Drewsen, and A Retzker, “General scheme for the construction of a protected qubit subspace,” *Phys. Rev. Lett.*, vol 111, pp. 230507-230511, 2013.

[111] Z. Y. Wang, J. M. Cai, A. Retzker, and M. B. Plenio, “All-optical magnetic resonance of high spectral resolution using nitrogen-vacancy spin in diamond,” *New J. Phys.*, vol. 16, pp. 083033-083048, 2014.

[112] N. Timoney, I. Baumgart, M Johanning, A. F. Varon, M. B. Plenio, A. Retzker, and C. Wunderlich, “Quantum gates and memory using microwave-dressed states,” *Nature*, vol. 476, 2011.

[113] P. London, J. Scheuer, J. M. Cai, I. Schwarz, A. Retzker, M. B. Plenio, M. Katagiri, T. Teraji, S. Koizumi, J. Isoya, R. Fischer, L. P. McGuinness, B. Naydenov, and F. Jelezko, “Detecting and polarizing nuclear spins with double resonance on a single electron spin,” *Phys, Rev. Lett.*, vol. 111, pp. 067601-067605, 2013.

[114] X. Xu, Z. Wang, C. Duan, P. Huang, P. Wang, Y. Wang, N. Xu, X. Kong, F. Shi, X. Rong, and J. Du., “Coherence-protected quantum gate by continuous dynamical decoupling in diamond,” *Phys. Rev. Lett.*, vol. 109, pp. 070502-070506, 2012.

[115] J. M. Cai, B. Naydenov, R. Pfeiffer, L. P. McGuinness, K. D. Jahnke, F. Jelezko, M. B. Plenio, and A. Retzker, “Robust dynamical decoupling with concatenated continuous driving,” *New J. Phys.*, vol. 14, pp. 113023-113038, 2012.

[116] N. Mizuochi, P. Neumann, F. Rempp, J. Beck, V. Jacques, P. Siyushev, K. Nakamura, D. J. Twitchen, H. Watanabe, S. Yamasaki, F. Jelezko, and J. Wrachtrup, “Coherence of single spins coupled to a nuclear spin bath of varying density,” *Phys. Rev. B*, vol. 80, pp. 041201-041204, 2009.

[117] G. D. Fuchs, V. V. Dobrovitski, D. M. Toyli, F. J. Heremans, and D. D. Awschalom, “Gigahertz dynamics of a strongly driven single quantum spin,” *Science*, vol. 326, pp. 1520-1522, 2009.

[118] E. R. MacQuarrie, T. A. Gosavi, N. R. Jungwirth, S. A. Bhave, and G. D. Fuchs, “Mechanical spin control of nitrogen-vacancy centers in diamond,” *Phys. Rev. Lett.*, vol. 111, pp. 227602-227606, 2013.